Pontifícia Universidade Católica
do Rio de Janeiro

Lucas Araujo Lima Almeida

Charge transfer complexes with high surface area based on TiO_2 nanoparticles modified with bidentate ligands: synthesis, characterization and photocatalytic activity under low-power visible light

Tese de Doutorado

Thesis presented to the Programa de Pó-Graduação em Engenharia de Materiais e de Processos Químicos e Metalúrgicos of PUC-Rio in partial fulfillment of the requirements for the degree of Doutor em Engenharia de Materiais e de Processos Químicos e Metalúrgicos.

Advisor: Prof. Bojan Marinkovic

Rio de Janeiro

September 2023

PONTIFÍCIA UNIVERSIDADE CATÓLICA
DO RIO DE JANEIRO

Lucas Araujo Lima Almeida

Charge transfer complexes with high surface area based on TiO_2 nanoparticles modified with bidentate ligands: synthesis, characterization and photocatalytic activity under low-power visible light

Thesis presented to the Programa de Pó-Graduação em Engenharia de Materiais e de Processos Químicos e Metalúrgicos of PUC-Rio in partial fulfillment of the requirements for the degree of Doutor em Engenharia de Materiais e de Processos Químicos e Metalúrgicos. Approved by the Examination Committee.

Prof. Bojan Marinkovic
Advisor
Departamento de Engenharia Química e de Materiais – PUC-Rio

Prof. Roberto Ribeiro de Avillez
Departamento de Engenharia Química e de Materiais – PUC-Rio

Profª. Anupama Ghosh
Departamento de Engenharia Química e de Materiais – PUC-Rio

Dr. Marco André Fraga
Institudo Nacional de Tecnologia – INT

Profª. Paula Mendes Jardim
Universidade Federal do Rio de Janeiro – UFRJ

Rio de Janeiro, September 21st, 2023.

Lucas Almeida Araujo Lima Almeida

Graduated in Petroleum Engineering with additional domain in Materials for Engineering at Pontificia Universidade Católica do Rio de Janeiro (Puc - Rio) in 2017 and obtained his M.Sc. Degree in Materials Engineering and Chemical and Metallurgical Processes from (Puc - Rio). He had experience in the synthesis and characterization of nanostructures, visible-sensitive TiO_2-based nanomaterials and photocatalysis area. Currently, he works as researcher specializing in X-ray diffraction, thermogravimetric analysis, scanning electron microscopy and X-Ray fluorescence.

Ficha Catalográfica

Almeida, Lucas Araujo Lima

Charge transfer complexes with high surface area based on TiO_2 nanoparticles modified with bidentate ligands: synthesis, characterization and photocatalytic activity under low-power visible light / Lucas Araujo Lima Almeida; advisor: Bojan Marinkovic. – Rio de Janeiro: PUC, Departamento de Engenharia Química e de Materiais, 2023.

104 f.: il. color.; 30 cm

Tese (doutorado) - Pontifícia Universidade Católica do Rio de Janeiro, Departamento de Engenharia Química e de Materiais.

Inclui referências bibliográficas.

1. Engenharia Química e de Materiais – Teses. 2. Nanopartículas. 3. Quelante bidentado. 4. Transferência de carga do ligante para o metal. 5. Vacâncias de oxigênio. 6. Radical superóxido. I. Marinkovic, Bojan. II. Pontifícia Universidade Católica do Rio de Janeiro. Departamento de Engenharia Química e de Materiais. III. Título.

CDD: 620.11

Education, favela and culture.
The opportunities and commitment are the basis of social transformations.
My family.

Acknowledgments

My deepest thanks to my Advisor, Prof. Bojan Marinkovic, for the construction of collective scientific and critical thinking. For your dedication, investment and teachings over the years. In addition to, of course, believing in people and giving genuine opportunities. For this, my immense gratitude.

I would like to thank my friends at our Centro de Pesquisa e Caracterização Avançada de Materiais (CePeCAM) of departamento de Engenharia de Química e de Materiais (DEQM, PUC-Rio) for their complete welcome. MSc. Juliana Viol and Dra. Anja Dosen for teaching different characterization and partnership techniques. In particular Fábian Orozco, Freddy Rojas, Emanuel Pessanha, Esteban Camilo e Ananias Emmerick for sharing the work environment and their knowledge with me.

I thank professor Marco Cremona (Department of Physics, PUC-Rio) and postdoctoral student Rafael dos Santos (Department of Physics, PUC-Rio) for the photoluminescence analysis.

I thank professor (Physical Sciences Laboratory, UENF) and doctoral student Francine Menezes (Physical Sciences Laboratory, UENF) for the EPR analyses.

I also thank Professor Jordi Llorca (Department of Chemical Engineering, Polytechnic University of Catalonia) for the XPS analyses.

My eternal thanks to my family for their unconditional love, a life of opportunities and for being my source of inspiration. Mainly, to my grandparents, my parents, my sister and my girlfriend. My total gratitude for my journey and story.

This study was financed in part by the Coordenação de Aperfeiçoamento de Pessoal de Nível Superior - Brasil (CAPES) - Finance Code 001.

Abstract

Almeida, Lucas Araujo Lima; Marinkovic, Bojan (Advisor). **Charge transfer complexes with high surface area based on TiO_2 nanoparticles modified with bidentate ligands: synthesis, characterization and photocatalytic activity under low-power visible light**. Rio de Janeiro, 2023. 104p. Tese de Doutorado - Departamento de Engenharia Química e de Materiais, Pontifícia Universidade Católica do Rio de Janeiro.

Visible light-sensitive TiO_2-based nanomaterials are among the most promising alternatives for photocatalytic applications, such as environmental remediation. The charge transfer complexes (CTCs) between nano-TiO_2 and bidentate ligands, an alternative, have been widely studied. However, the photodegradation efficiency and role of reactive oxidizing species (ROS) are not fully understood. In addition, the development of CTCs based on TiO_2 modified with malonic acid (MoA) have not yet been investigated, as far as the authors know. In this study, TiO_2-Acetylacetone (ACAC) and TiO_2-MoA CTCs with high surface area were synthesized *via* sol-gel route. Both as-prepared TiO_2-based CTCs were subjected to tetracycline and chlorophenol photocatalytic degradation tests with and without ROS scavengers under low-power visible light (26 W). The TiO_2-MoA CTCs were fully characterized by XRPD, MS-TGA, FTIR, N_2 adsorption-desorption, DRS, PL, EPR and XPS analysis. The sol-gel synthesis and the calcination process adopted produced CTCs of nano-TiO_2 anatase strongly bond (covalent bond) with acetylacetone and malonic acid, capable of absorbing along the visible spectrum when calcined at 300 °C (TiO_2-ACAC-300) and 270 °C (TiO_2-MoA-270). Both calcined CTCs present single electron trapped in oxygen vacancy (SETOV / F^+ color center). The TiO_2-MoA-270 CTCs showed very high surface areas (>306 $m^2.g^{-1}$), mesopore volumes (>0.339 $mL.g^{-1}$) and the highest photocatalytic activity, degrading approximately 100% of the TC after 6 h. The TiO_2-MoA-270 and TiO_2-A300 CTCs were an efficient source of $^{\bullet}O_2^-$ radicals and inefficient generation of $OH^{\bullet}$ radicals. The findings of this research can be applied to the synthesis, *via* sol-gel, of other CTCs, such as dicarboxylic acids, and explored in further studies on air purification and hydrogen production.

Keywords

Nanoparticles; bidentate chelating; ligand-to-metal charge transfer; oxygen vacancies; superoxide anion radical; remediation of aqueous pollutants.

Resumo

Almeida, Lucas Araujo Lima; Marinkovic, Bojan (Advisor). **Complexos de transferência de carga com alta área superficial baseados em TiO_2 nanométrico modificado com ligantes bidentados: síntese, caracterização e atividade fotocatalítica sob luz visível de baixa potência**. Rio de Janeiro, 2023. 104p. Tese de Doutorado - Departamento de Engenharia Química e de Materiais, Pontifícia Universidade Católica do Rio de Janeiro.

Os nanomateriais à base de TiO_2 sensíveis à luz visível estão entre as alternativas mais promissoras para aplicações fotocatalíticas, como remediação ambiental. Os complexos de transferência de carga (CTCs) entre nano-TiO_2 e ligantes bidentados, uma alternativa, têm sido amplamente estudados. No entanto, a eficiência da fotodegradação e o papel das espécies oxidantes reativas (ROS) não são totalmente compreendidos. Além disso, o desenvolvimento de CTCs baseados em TiO_2 modificado com ácido malônico (MoA) ainda não foi investigado, até onde é sabido. Neste estudo, CTCs de TiO_2-Acetilacetona (ACAC) e TiO_2-MoA com alta área superficial foram sintetizados *via* sol-gel. Ambos os CTCs à base de TiO_2 preparados foram submetidos a testes de fotodegradação de tetraciclina e clorofenol com e sem sequestrantes de ROS sob luz visível de baixa potência (26 W). Os CTCs TiO_2-MoA foram totalmente caracterizadas por análises de DRX, MS-TGA, FTIR, adsorção-dessorção de N_2, DRS, PL, EPR e XPS. A síntese sol-gel e o processo de calcinação adotado produziram CTCs de anatásio fortemente ligados (ligação covalente) com acetilacetona e ácido malônico, capazes de absorver ao longo do espectro visível quando calcinados a 300 °C (TiO_2-A300) e 270 °C (TiO_2-MoA-270). Ambos os CTCs calcinados apresentam um único elétron preso na vacância de oxigênio (SETOV / centro de cores F^+). Os CTCs TiO_2-MoA-270 apresentaram áreas superficiais (>306 $m^2.g^{-1}$), volumes de mesoporos (>0,339 $mL.g^{-1}$) e atividade fotocatalítica extremamente elevados, degradando aproximadamente 100% de TC após 6 h. Os CTCs TiO_2-MoA-270 e TiO_2-A300 são uma fonte eficiente de geração de radicais $^{\bullet}O_2^-$ e ineficientes geradores de radicais $OH^{\bullet}$. Os resultados desta pesquisa podem ser aplicados à síntese, via sol-gel, de outros CTCs, como os ácidos dicarboxílicos, e explorados em estudos posteriores sobre purificação do ar e produção de hidrogênio.

Palavras-chave

Nanopartículas, quelante bidentado, transferência de carga do ligante para o metal, vacâncias de oxigênio, radical superóxido, remediação de poluentes aquosos.

Contents

List of Figures

List of Tables

List of Equations

1. Introduction

The remediation of air, river and marine pollution are latent challenges today. The disposal of wastewater from industrial processes and the intensive use of drugs for the treatment of human health are potential sources of contamination of aqueous effluents (Liu *et al.*, 2020; Moraes, de, Torezin, *et al.*, 2020; Zhou *et al.*, 2020). Among the pollutants are the organic compound chlorophenol and the drug tetracycline (an antibiotic). Chlorophenol is a priority pollutant due to its high toxicity, low biodegradability, and carcinogenic and endocrine disruptive properties (Moraes, de, Torezin, *et al.*, 2020; Moraes, de, Valim, *et al.*, 2020). In addition, water treatment plants are not designed for the remediation of pharmaceutical and personal care products (PPCPs), such as tetracycline (He, Kai e Ding, 2021; Liu *et al.*, 2020; Zhou *et al.*, 2020).

Technological advances and commitment to sustainability are currently important guidelines for scientific development. In this context, photocatalysis presents itself as an alternative and sustainable technology for the abatement of pollutants, being promising and widely investigated. The process of absorbing solar radiation to reduce activation energy and promote desired chemical reactions is the basic concept of photocatalysis. Therefore, the development of photocatalyst materials and new nanomaterials are relevant to the scientific community and society.

Thus, this thesis aims at the synthesis, characterization and evaluation of the photocatalytic potential, under low-power visible light (26 W), of nanocrystalline photocatalysts composed of TiO_2 modified with chelating ligands (acetylacetone and malonic acid), using chlorophenol and tetracycline as test molecules. Furthermore, the impact of chelating ligands on the optical and photocatalytic properties of TiO_2 nanoparticles is studied, as well as the generation efficiency of reactive oxidizing species in charge transfer complexes of TiO_2 chelating ligands. The following is a brief description of the subsequent chapters:

- Chapter 2: Theoretical foundation and bibliographic review. The foundations for understanding photocatalysis as a sustainable technology, its challenges, and mechanisms to enhance

photocatalytic activity are presented. In addition, the knowledge gap filled by this research are presented.

- Chapter 3: Objectives of the thesis.

- Chapter 4: TiO_2-Acetylacetone as an efficient source of superoxide radicals under reduced power visible light: photocatalytic degradation of chlorophenol and tetracycline. The results showed in this chapter were published in the Journal Catalysts (Almeida *et al.*, 2022).

- Chapter 5: Enhanced photocatalytic activity of TiO_2 anatase nanoparticles modified with malonic acid under reduced power visible light: synthesis, characterization and degradation of tetracycline and chlorophenol.

- Chapter 7: Conclusion and future works

2. Literature Review

2.1. Photocatalysis as a sustainable technology

Solar radiation is a renewable and abundant source of energy. Several studies sought to optimize the absorption of sunlight to use it as a resource in practical applications. Photocatalysis is one such application that consists of the process of absorbing solar electromagnetic radiation, promoting a reduction in the activation energy of certain chemical reactions. (Luciani, Imparato e Vitiello, 2020)

Currently, studies are being carried out in the area of photocatalysis with the following objectives: degradation of dyes (Hunge *et al.*, 2018; Sabzehei *et al.*, 2020), hydrogen production (Chen *et al.*, 2020; Dessal *et al.*, 2019), treatment of effluents contaminated by heavy metals, organic compounds and drugs (Bai *et al.*, 2020; Liu *et al.*, 2020; Moraes, de, Torezin, *et al.*, 2020; Wang *et al.*, 2020) and air purification (Almeida *et al.*, 2020; Habran, Pontón, *et al.*, 2018; Hernández Rodríguez *et al.*, 2020).

Sunlight is composed of infrared (energy <1.7 eV), visible (1.7 eV to 3.2 eV) and ultraviolet (>3.2 eV) spectra. The ultraviolet (UV) spectrum makes up the smallest portion of sunlight, less than 5% (Zhou *et al.*, 2012). However, most research in photocatalysis was initially carried out in this radiation range due to the properties of materials with photocatalytic potential (photocatalyst). (Christoforidis e Fornasiero, 2017; Fujishima e Honda, 1972; Ren *et al.*, 2017; Tsang *et al.*, 2019)

The main foundations for the occurrence of photocatalytic activity are the capacity of pairs of free electron and electronic holes (e^-/h^+) on the surface of materials, due to the incidence of photons, to interact with molecules present in the environment (O_2 and H_2O) and, consequently, generation of reactive oxidizing species ($^{\bullet}O_2^-$ and $OH^{\bullet}$) (Ren *et al.*, 2017). Figure 1 exemplifies the photocatalytic process for the abatement of the gaseous pollutant NO_x and conversion into NO_3^-.

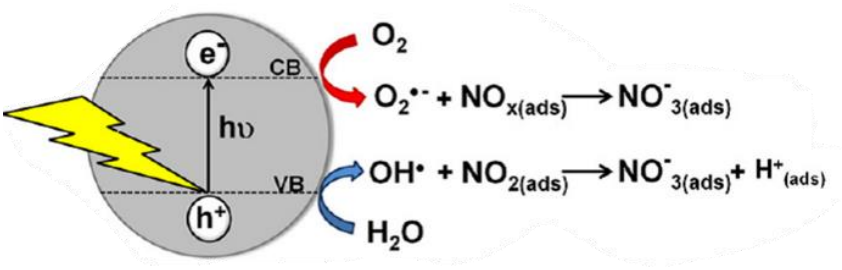

Figure 1: Representative scheme of the photocatalytic process for degradation of NO_x gas (Tsang *et al.*, 2019).

As seen in Figure 1, only materials with forbidden energy band are able to perform photocatalysis. The separation between the valence band (VB) and the conduction band (CB) implies the existence of a bandgap in the material, requiring the application of external energy for the electrons within the VB to be injected into the CB and, consequently, form e^-/h^+ pairs. Therefore, ceramic and semiconductor materials are the basis for the development of photocatalysts. (Almeida, 2019; Esteban, 2017)

On the other hand, the photocatalytic efficiency is related to the VB and CB distribution of the materials in relation to the redox potential of the normal hydrogen electrode (NHE) under standard conditions ($[H^+]$ = 1 mol L^{-1}, temperature = 25 °C e pression = 1 atm). This knowledge is important because the reduction and oxidation reactions of O_2 into $^{\bullet}O_2^-$ and H_2O/OH^- into $OH^{\bullet}$, respectively, have different redox potentials. Furthermore, the values of the ceramic bandgaps limit the range of solar radiation that could be absorbed by the photocatalysts and, consequently, their photocatalytic performance. (Ren *et al.*, 2017)

2.2. Photocatalytic potential of semiconductors

Different semiconductor ceramic materials are researched as photocatalysts due to variations in the bandgap value, BV and BC positions in relation to the redox potential and desired photocatalytic application (Christoforidis e Fornasiero, 2017). Semiconductors with smaller bandgap provide higher absorption of sunlight (UV

and, possibly, visible light). Figure 2 shows the VB and CB positions of different semiconductors in relation to the NHE redox potential for H_2 production.

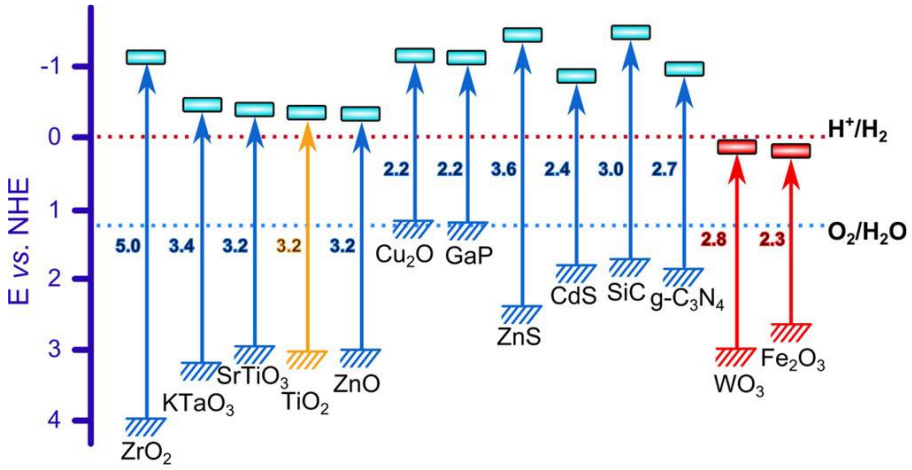

Figure 2: Distribution Scheme of VB and CB, and the bandgap values of different semiconductors in relation to the redox potential. (Christoforidis e Fornasiero, 2017)

The photocatalytic production of hydrogen occurs through two half-reactions. One is the oxidation reaction of the H_2O molecule, in which the H_2O molecule is broken down producing O_2 and H^+. The second is the half reaction of the reduction of H^+ to H_2. These reactions are possible due to the interaction of h^+ in VB with H_2O and of e^- in CB with H^+, as seen in Figure 2. Therefore, semiconductors with VB with redox potential higher than the reduction reaction of O_2/H_2O and with CB with lower redox potential than the H^+/H_2 reduction reaction showed a higher potential for H_2 production.

TiO_2 and CdS semiconductors are examples of suitable photocatalysts for this application. However, the bandgap value and the chemical stability of the material are also crucial factors for choosing the photocatalyst. CdS would be the most appropriate material due to its smaller bandgap, allowing absorption of visible light (between 2.4 eV and 3.2 eV) and the entire UV spectrum. However, CdS is affected by the phenomenon of photocorrosion, which significantly reduces its stability under working conditions. (Banerjee *et al.*, 2021; Liu *et al.*, 2021)

On the other hand, TiO_2 is one of the most chemically stable oxides, it is non-toxic and has high stability against photocorrosion. These characteristics combined with the excellent cost-effectiveness and, mainly, the ability to also react with O_2 molecules and OH^- ions to generate reactive oxidizing species (ROS) make TiO_2

the most versatile and studied semiconductor in the area of photocatalysis. (Christoforidis e Fornasiero, 2017)

Figure 3 shows, for several semiconductors, the alignment of VB and CB boundaries in relation to the NHE redox potential to produce ROS, superoxide ($^{\bullet}O_2^-$) and hydroxyl radicals ($OH^{\bullet}$). ROS are reactive radicals that promote the abatement/degradation of environmental pollutants, in which photocatalysis is used as an alternative remediation technology.

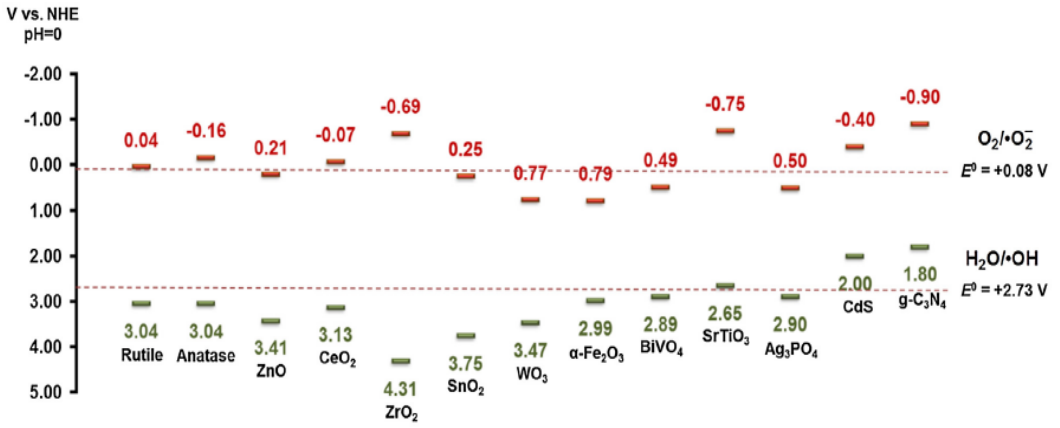

Figure 3: Scheme of the electronic bands of different semiconductors in relation to the redox potential (Ren *et al.*, 2017).

The main crystalline phases of TiO_2, rutile and anatase, reported in Figure 3 corroborate the photocatalytic potential of TiO_2, since both energy bands participate in the formation of $^{\bullet}O_2^-$ and $OH^{\bullet}$ radicals. However, TiO_2, as well as other semiconductors, have intrinsic disadvantages that encourage the development of new optimized photocatalysts based on TiO_2 (Almeida *et al.*, 2020; Gil-Londoño, Cremona, *et al.*, 2023; Imparato *et al.*, 2022; Moraes, de, Torezin, *et al.*, 2020) and based on other semiconductors such as CeO_2, Nb_2O_5, Mg_2TiO_4, etc (Chen *et al.*, 2017; Divins *et al.*, 2021; Medić *et al.*, 2016).

2.3. Development of novel photocatalysts

Currently, studies on photocatalysis focus their efforts on solving the following intrinsic drawbacks of semiconductors: (Habran, Pontón, *et al.*, 2018)

1) Small surface area
2) insufficient absorption of visible radiation
3) rapid e^-/h^+ pairs recombination

The development of new photocatalysts present these research guidelines. Different solutions are investigated individually or jointly. The drawbacks 1) and 2), for example, can be overcome together through the synthesis of nanometric semiconductors with metallic nanoparticles (He, Kai e Ding, 2021; Martínez *et al.*, 2019) or organic molecules (dyes and chelating ligands) (Luciani, Imparato e Vitiello, 2020; Zhang, Kim e Choi, 2014). In addition, point 3) can be solved, for example, by developing heterostructures based on semiconductors with different bandgaps (He, Kai e Ding, 2021; Omrani e Nezamzadeh-Ejhieh, 2020) and/or semiconductors with the presence of extrinsic oxygen vacancies (Almeida *et al.*, 2020; Gil-Londoño, Krambrock, *et al.*, 2023; Kato *et al.*, 2022). Therefore, different mechanisms are presented to enhance the photocatalytic activity with the aim of developing novel TiO_2-based materials.

2.4. TiO_2 with high surface area

The surface area is a fundamental parameter for photocatalytic activity. Photocatalysts with a high surface area have a higher probability of promoting photocatalytic reactions due to the higher availability of reactive sites on the surface. Furthermore, a high surface area is generally a consequence of the nanometric dimensions of the crystallite/grain of ceramic materials. Therefore, the synthesis of nanomaterials promotes two benefits to the enhanced photocatalytic activity. Lower diffusion distance of photogenerated charges (e^-/h^+ pairs) to the TiO_2 surface and high surface area, increasing the probability of ROS

photogeneration and reduction of e^-/h^+ pairs recombination. (Habran, Krambrock, *et al.*, 2018; Kim e Kwak, 2007; Ren *et al.*, 2017)

TiO_2 is a polymorphic ceramic material, some of which are rutile, anatase and brookite. However, anatase is reported as the phase with the best photocatalytic performance under UV light. This attribution occurs partially, because anatase is the most stable phase when the objective is to synthesize nanometric TiO_2. (Bakre e Tilve, 2017; Fujishima, Zhang e Tryk, 2008; Ohno, Sarukawa e Matsumura, 2001)

The synthesis of nanometric anatase is commonly performed through the alkaline hydrothermal and sol-gel routes. The hydrothermal alkaline method enables the synthesis of TiO_2 with different morphologies such as nanowires, nanorods, nanotubes and nanosheets. However, hydrothermal alkaline synthesis is normally not capable of producing anatase as the only phase (Abreu *et al.*, 2012; Martínez *et al.*, 2019). On the other hand, the sol-gel route is capable of exclusively synthesizing anatase. Furthermore, the sol-gel synthesis produces deagglomerated anatase nanoparticles with dimensions smaller than 20 nm using temperatures and synthesis times lower than the hydrothermal alkaline route. (Fujishima, Zhang e Tryk, 2008)

The sol-gel synthesis process consists of three steps between the initial use of titanium alkoxide (precursor) and the final production of nanocrystalline anatase. (Scolan e Sanchez, 1998)

The first step is the formation of the TiO_2 sol. Initially, the titanium alkoxide is mixed with a solution of water and ethanol. Alcohol (ethanol) dissolves the alkoxide, while water participates in the hydrolysis process. Subsequently, an acid solution is added to contribute to the hydrolysis and condensation reactions, the final product of this step is a solution of polymerized species (TiO_2 sol). The hydrolysis and condensation processes are described in Figure 4 where M is a metal, R is an alkyl chain and M(OR)z is the metal alkoxide. (Sanchez e Livage, 1988; Scolan e Sanchez, 1998)

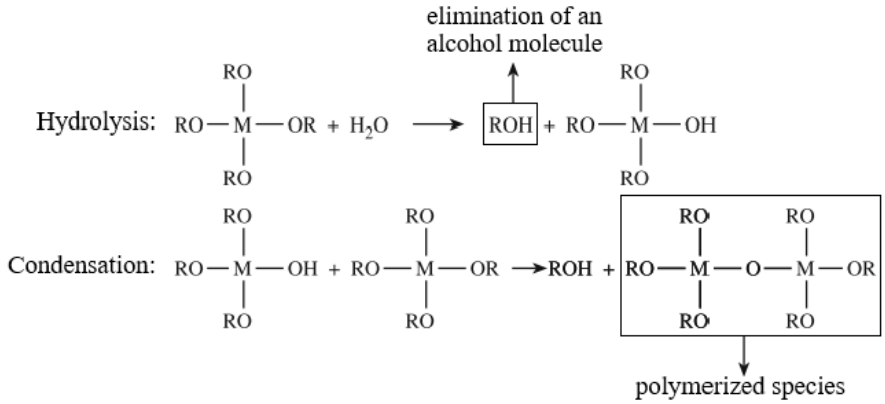

Figure 4: Simplified scheme of the hydrolysis and condensation reactions of a metallic alkoxide solution (Norton e Carter, 2007).

The second stage consists of transforming the sol into gel. The transition occurs by the abrupt increase in viscosity of the sol due to the significant formation of long polymerized species (chains) and the formation of cross-links between them. TiO_2 gel is composed of an amorphous three-dimensional chain of polymerized species and liquids such as alcohol and water. Finally, step three consists of the formation of deagglomerated nanocrystalline TiO_2, after a drying and calcination process of the gel. (Norton e Carter, 2007)

The improvement of sol-gel synthesis with the development of new research was able to produce anatase nanoparticles with dimensions smaller than 10 nm and surface areas greater than 100.0 $m^2 g^{-1}$ (Almeida *et al.*, 2020). The incorporation of strong chelating ligands (complexing agents) such as carboxylic acids, dicarboxylic acids and β-diketones during sol-gel synthesis was the main factor for this achievement. The chelating ligands act to control the rate of hydrolysis and condensation of the titanium alkoxide, contributing to the reduction of polymeric chains and, consequently, to the final size of the TiO_2 particles. The reaction scheme of Figure 5 illustrates the interaction of the acetylacetone molecule (β-diketones) with the Ti^{4+} atom until the final formation of TiO_2 nanoparticles. (Almeida *et al.*, 2020; Bakre e Tilve, 2017; Habran, Pontón, *et al.*, 2018; Scolan e Sanchez, 1998)

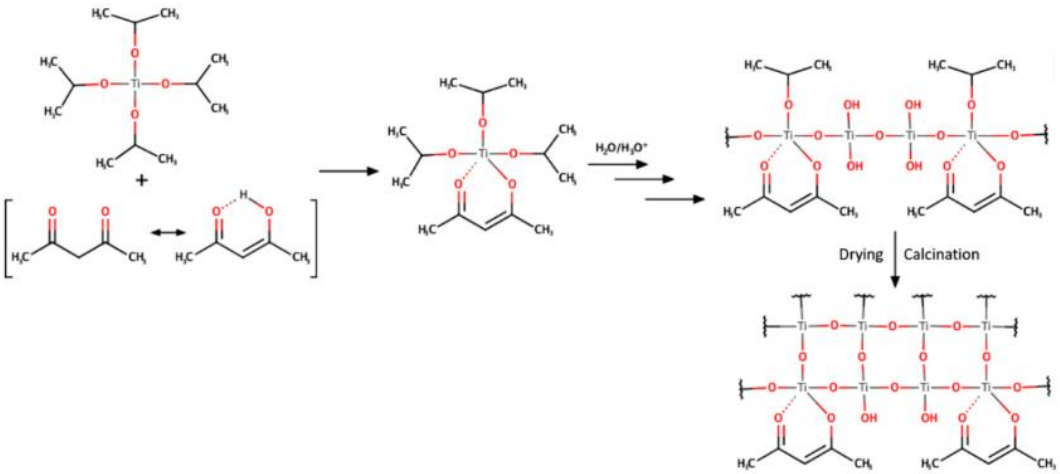

Figure 5: Scheme of reactions for formation of bonds between acetylacetone in keto-enol form and the Ti^{4+} atom (Almeida *et al.*, 2020)

Scolan and Sanchez (Scolan e Sanchez, 1998) pioneered the incorporation of β-diketone acetylacetone during sol-gel synthesis. They investigated the influence of the molar concentration of the complexant in relation to the molar concentration of Ti (A= [ACAC]/[Ti]). Scolan and Sanchez (Scolan e Sanchez, 1998) concluded that increasing the molar ratio from 1 to 4 resulted in nanometer-sized anatase xerogels, on the order of 4 nm and 1.5 nm, respectively. However, the surface areas of the synthesized oxides were not evaluated.

Recently, Habran et al. (Habran, Pontón, *et al.*, 2018) and Almeida et al. (Almeida *et al.*, 2020) reported surface area values for TiO_2 synthesized according to the methodology adopted by Scolan and Sanchez (Scolan e Sanchez, 1998) with ratio A= 2. The TiO_2 xerogel (dried at room temperature) with 2.5 nm crystallites and the xerogel calcined at 300°C in air with 6.6 nm crystallites revealed high surface areas of 132.0 $m^2\ g^{-1}$ and 137.0 $m^2\ g^{-1}$, respectively.

From another perspective, Bakre and Tilve (Bakre e Tilve, 2017) studied the addition of nine different dicarboxylic acids as a complexing agent in sol-gel synthesis. The influence of the chemical structure of the acids on the control of the physical properties of TiO_2 nanoparticles after calcination at 500 °C for 3 h was investigated. It was concluded that linear dicarboxylic acids, without extra functional groups and with *cis* geometry, such as malonic acid, glutaric acid and maleic acid are capable of synthesizing pure anatase with nanometric dimensions. Another relevant characteristic reported were the surface areas of 253.8 $m^2\ g^{-1}$ and 297.0 $m^2\ g^{-1}$ obtained for TiO_2 synthesized with the addition of malonic acid and

glutaric acid, respectively. These two TiO_2 nanoparticles showed the best photocatalytic performances for methylene blue dye degradation under UV irradiation, corroborating the positive impact of the high surface area. (Bakre e Tilve, 2017)

Therefore, sol-gel synthesis with the incorporation of chelating ligands is an efficient alternative to reduce particle size and increase surface area.

2.5. TiO_2 sensitive to visible light

Currently, one of the most significant challenges in the application of photocatalysis on a large scale is the inability of most semiconductors and TiO_2 to efficiently absorb solar radiation. Although the bandgap value of TiO_2 is decisive for the formation of superoxide and hydroxyl radicals, the value of 3.2 eV contributes negatively to solar sensitization, since semiconductors sensitive to visible light must have a bandgap between 1.7 eV and 3.2 eV. The UV spectrum makes up only 3% of the visible spectrum, while visible light comprises 44%. (Kapilashrami *et al.*, 2014; Zhou *et al.*, 2012)

Therefore, one of the main advances is the visible sensitization of intrinsic semiconductors that have high photocatalytic activity in the UV spectrum, such as TiO_2.

The TiO_2 sensitization alternatives studied in the last decades area: a) doping with metals or non-metals, b) coupling with other narrow bandgap semiconductors, c) synthesis of "Black TiO_2" and d) coupling with dyes or small organic molecules (Kapilashrami *et al.*, 2014; Luciani, Imparato e Vitiello, 2020; Ullattil *et al.*, 2018; Zhang, Kim e Choi, 2014). Although there are different visible sensitization mechanisms, the interaction of chelating ligands (small organic molecules) with TiO_2 has gained prominence. (Aronne *et al.*, 2017; Li *et al.*, 2019; Milićević *et al.*, 2017; Sannino *et al.*, 2015)

This recent line of research is able to explore two mechanisms of increased photocatalytic activity simultaneously. As mentioned in section 2.4, bidentate ligands (complexing agents) when incorporated into sol-gel synthesis are able to form nanometric anatase with high surface area. Therefore, sensitization via bidentate ligands becomes even more advantageous.

The absorption of visible light provided by the bidentate bonds with the TiO_2 surface occurs due to the ligand to metal charge transfer (LMCT) mechanism when excited by visible photons. The bond formed enables the transfer of charge from the highest occupied molecular orbital (HOMO) of the ligand directly to the CB of TiO_2, since the HOMO of the complexant has intermediate energy level between VB and CB of TiO_2. Figure 6 illustrates the LMCT mechanism and the photocatalytic reaction of reduction of O_2 to $^{\bullet}O_2^-$ or H^+ to H_2 (electron acceptors). (Zhang, Kim e Choi, 2014)

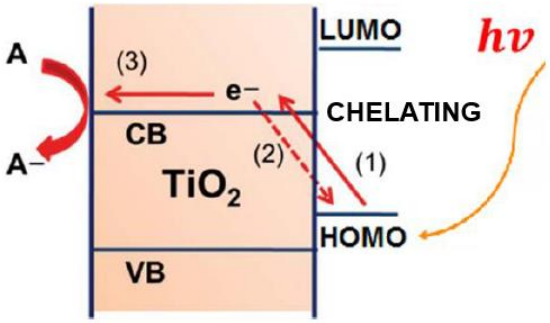

Figure 6: Schematic model of visible sensitization of TiO_2 by coupling with chelating ligand. (A represents an electron acceptor) (Zhang, Kim e Choi, 2014)

The steps (1), (2) and (3) presented in Figure 6 indicate, respectively, the transfer of electrons from the HOMO of the chelator to the CB of TiO_2 (LMCT mechanism), the recombination of the e^-/h^+ pairs and the reaction of excited electrons with acceptor species on the surface of TiO_2 coupled with a chelating ligand. (Zhang, Kim e Choi, 2014)

Scolan and Sanchez (Scolan e Sanchez, 1998) and Habran et al. (Habran, Pontón, *et al.*, 2018) reported that excessive addition of the bidentate acetylacetone (ACAC), [ACAC]/[Ti] molar ratios between 1 and 5, in the sol-gel route sensitizes TiO_2 sol and nanocrystalline TiO_2 xerogels in the visible spectrum. In addition, Sannino et al. (Sannino *et al.*, 2015) and Addonizio et al. (Addonizio, Aronne e Imparato, 2020) reported that low [ACAC]/[Ti] molar ratios (0.4 and 0.5) also promote the formation of the LMCT mechanism, however, they form amorphous TiO_2 xerogels. Figure 7 proves the visible light sensitization of TiO_2 xerogels synthesized by Sannino et al. (Sannino *et al.*, 2015) and Habran et al. (Habran, Pontón, *et al.*, 2018).

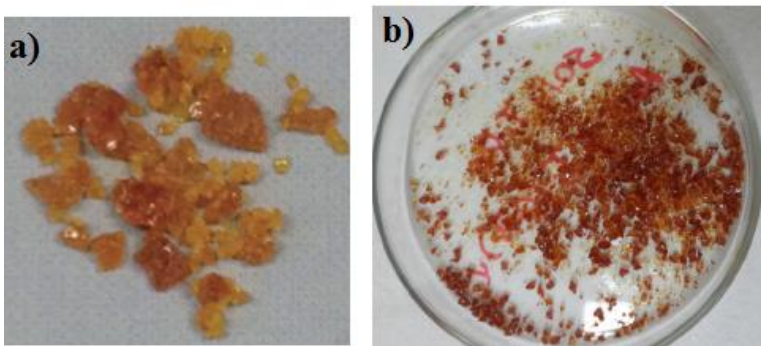

Figure 7: a) Xerogel dried at room temperature (Sannino *et al.*, 2015); b) xerogel dried at 100 °C (Habran, Pontón, *et al.*, 2018).

Recently, Almeida et al. (Almeida *et al.*, 2020) demonstrated the high photocatalytic potential of the charge transfer complex (CTC) formed between ACAC and TiO_2 for the abatement of NOx pollutant gas under visible light. It was revealed that the TiO_2 xerogel calcined at 300 °C for 2 h (TiO_2-ACAC-300) showed an abatement of ~100% during 1 h of visible light exposure. This result was 5 times better than the performance of TiO_2-ACAC xerogel and 13 times better than P-25 (standard photocatalyst, Evonik). The ACAC excess promotes two types of bonds on the TiO_2 surface, a strong bond (covalent) with Ti^{4+} atoms and a weak one due to excess ACAC adsorbed on the surface, in which the covalent bonds are effective for the LMCT mechanism and for NO_x gas abatement. (Almeida *et al.*, 2020)

Figure 8 shows the distribution scheme of the electronic bands of CTC TiO_2-ACAC in relation to the redox potential and the photooxidation reactions of the NO_x gas.

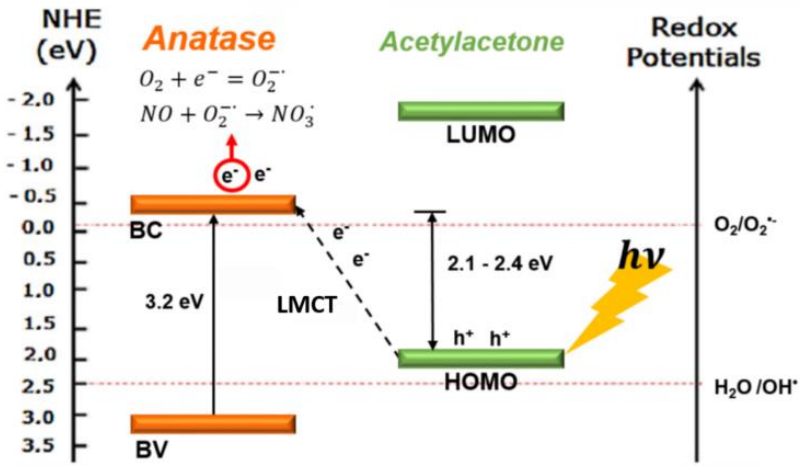

Figure 8: Scheme of the electronic bands of CTC TiO_2-ACAC and, consequently, the photooxidation reactions of NOx gas. (Almeida *et al.*, 2020).

The impact of the coupling between bidentate ligands and TiO_2 on the optical and photocatalytic properties still reveals important knowledge gaps. One of the proposals of this study, detailed later, was to continue the investigation of the photocatalytic potential of CTC TiO_2-ACAC, as proposed by the authors Almeida et al. (Almeida *et al.*, 2020).

Furthermore, the synthesis and characterization of novel LMCT systems with different bidentate ligands are scarce. Bakre and Tilve (Bakre e Tilve, 2017) studied different dicarboxylic acids for TiO_2 synthesis and photocatalytic evaluation in the UV spectrum. However, an investigation of the photocatalytic potential of the probable CTC formed between TiO_2 and dicarboxylic acids before their total evaporation at temperatures above 500 °C was not carried out.

In contrast to ACAC (β-diketone), the carboxylic acids such as malonic, glutaric and maleic acids have two extra hydroxyl functional groups beyond the double carbonyl (Figure 9), allowing higher interaction and formation of bidentate bonds with Ti^{4+}. The bonds in these dicarboxylic acids can occur through the carbonyl functional group in the keto-enol form (Figure 5), through the carboxyl group or through the two oxygens of the hydroxyl groups (Figure 9).

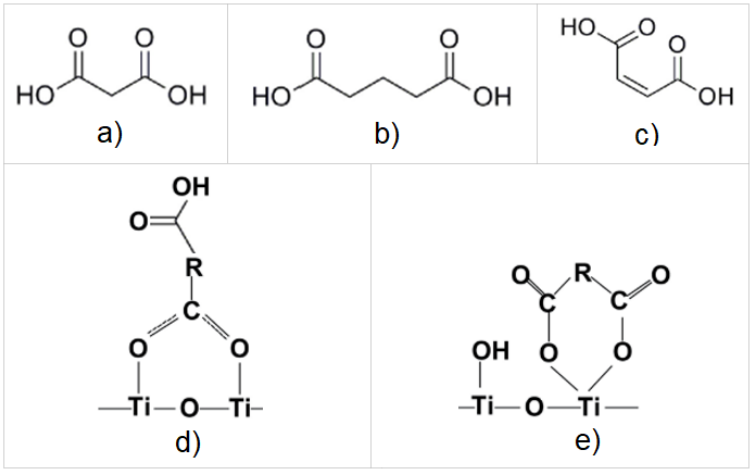

Figure 9: Chemical structure: a) malonic acid, b) glutaric acid, c) maleic acid. Scheme of the bidentate bonds of dicarboxylic acids between the functional groups d) carboxyl and e) hydroxyl with Ti^{4+}.

Therefore, the development of novel TiO_2 CTCs through sol-gel synthesis with the incorporation of dicarboxylic acids have the potential to overcome the photocatalytic performance of TiO_2-ACAC CTCs and further consolidate the LMCT mechanism as an efficient visible sensitizer for photocatalytic applications.

2.6. Efficiency of reactive oxidizing species on photocatalytic activity

The development of novel photocatalysts aim to promote an efficient generation of reactive oxidizing species. Thus, understanding the efficiency of ROS is extremely important. (Nosaka e Nosaka, 2017)

Currently, one of the most used methodologies to evaluate the efficiency of ROS occurs during photocatalytic measurements for the abatement of aqueous pollutants (chlorophenol, drugs and dyes). Organic molecules that act as ROS scavengers are added to the reaction medium, inhibiting the interaction of ROS with the pollutants. Methanol, ethanol and isopropanol molecules act as $OH^{\bullet}$ scavengers, making the photocatalytic participation of $OH^{\bullet}$ irrelevant to the degradation process (Alam *et al.*, 2019; Liu *et al.*, 2018; Moraes, de, Torezin, *et al.*, 2020; Moraes, de, Valim, *et al.*, 2020). On the other hand, the benzoquinone (BQ) molecule is commonly used as scavenger of $^{\bullet}O_2^-$ radicals (Abd Elkodous *et al.*, 2021; Liu *et al.*, 2018; Zhang, Li e Liu, 2020).

Alternatively, the evaluation of ROS occurs through analysis by electronic paramagnetic resonance (EPR) spectroscopy with the aid of molecules of 5,5-dimethyl-1-pyrroline N-oxide (DMPO) or 5-tert-butoxycarbonyl-5-methyl-1-pyrroline N-oxide (BMPO) to identify $^{\bullet}O_2^-$ and DMPO to identify $OH^{\bullet}$. (Nosaka e Nosaka, 2017)

Furthermore, photocatalytic tests in aqueous media to evaluate the potential of the photocatalyst, and the efficiency of each ROS when irradiated by visible light, must ensure that only the photocatalyst absorbs in the visible. Therefore, the aqueous pollutant should not contribute to the absorption of visible light and should show absorption peaks in the UV spectrum. The organic compound chlorophenol (model pollutant) and several drugs are used for this purpose, since dyes such as methylene blue and rhodamine B absorb in the visible spectrum and, consequently, artificially contribute to greater efficiency of the photocatalytic process. (Moraes, de, Torezin, *et al.*, 2020; Myilsamy *et al.*, 2016; Rochkind, Pasternak e Paz, 2015; Zhang, Li e Liu, 2020; Zhou *et al.*, 2020)

Wang et al. (Wang *et al.*, 2020) evaluated the efficiency of WO_3-TiO_2-Pt core-shell heterostructures for photodegradation of the drug tetracycline under solar irradiation using a 300 W xenon lamp as a light source. The best result presented

was 88.3% photocatalytic abatement after 2h for a molar ratio of 1:3 [WO_3] / [TiO_2] with 5% Pt by mass. The use of benzoquinone as a scavenger drastically reduced the photocatalytic activity at 23.5%, while the isopropanol scavenger showed an activity of 85% (efficiency virtually unchanged). Therefore, for this photocatalyst the superoxide radical plays a fundamental role in photocatalytic reactions. In addition, the efficiency of ROS $^{\bullet}O_2^-$ reported by Wang et al. (Wang *et al.*, 2020) suggests that the use of photocatalysts capable of producing only superoxide are extremely efficient for the abatement of tetracycline.

Therefore, the development of novel visible-sensitive photocatalysts based on TiO_2 nanoparticles modified by bidentate ligands must be submitted to photocatalytic tests with the presence of scavengers in liquid medium to evaluate the photogeneration of ROS ($^{\bullet}O_2^-$ and $HO^{\bullet}$), and consequently, its role in the abatement of chlorophenol and tetracycline.

3. Objectives

3.1 General objective

Development of novel charge transfer complexes with high surface area based on TiO_2 nanoparticles modified with bidentate ligands: synthesis, characterization and photocatalytic activity to degrade tetracycline and chlorophenol under low-power visible light.

3.2 Specific objectives

1) Photocatalytic performance of TiO_2-Acetylacetone CTC calcinated at 300 °C in air for the photodegradation of chlorophenol and tetracycline under reduced power visible light (26 W).
   - Understanding of ROS ($^{\bullet}O_2^-$ and $OH^{\bullet}$) roles in photocatalysis performed by TiO_2-ACAC using scavengers, such as benzoquinone and isopropanol.
   - Study of the volatilization profile of CTC TiO_2-ACAC up to 550 °C by thermogravimetric analysis coupled with mass spectroscopy.

2) synthesis, characterization and evaluation of the photocatalytic potential, under low-power visible light (26 W), of a novel nanocrystalline CTC composed of nano-TiO_2 bounded to malonic acid, using chlorophenol and tetracycline as test molecules.
   - Potential of ROS generation of TiO_2-Malonic acid CTC calcinated at 270 °C in air using ROS scavengers for $^{\bullet}O_2^-$ and $OH^{\bullet}$, such as benzoquinone and isopropanol, respectively.
   - Generalize the sol-gel synthesis and calcination conditions for the preparation of TiO_2-bidentate CTC, sensitive to the visible spectrum, and with specific surface areas larger than 250.0 $m^2\ g^{-1}$.

4.
TiO_2-Acetylacetone as an efficient source of superoxide radicals under reduced power visible light: photocatalytic degradation of chlorophenol and tetracycline

Lucas A. Almeida, Anja Dosen, Juliana Viol and Bojan A. Marinkovic.

The results presented in chapter 4 were published in the journal Catalysts (MDPI) 2022, 12, 116. DOI: 10.3390/catal12020116.

4.1
Background

The intensive use of drugs for the treatment of human health and industrial wastewater disposal are potential sources of contamination of aqueous effluents (Liu *et al.*, 2020; Mohammad *et al.*, 2021; Moraes, de, Torezin, *et al.*, 2020; Zhou *et al.*, 2020). Currently, water treatment plants are not designed for the remediation of pharmaceutical and personal care products (PPCPs) (Liu *et al.*, 2020; Zhou *et al.*, 2020). An example of PPCPs is the antibiotic tetracycline, used to prevent bacterial infections, found in sewage from the pharmaceutical industry, hospitals, and livestock (He, Kai e Ding, 2021; Wang *et al.*, 2020). The remediation of organic compounds, such as chlorophenol, is a priority due to its high toxicity, low biodegradability, and carcinogenic and endocrine disruptive properties (Moraes, de, Torezin, *et al.*, 2020; Moraes, de, Valim, *et al.*, 2020).

In this context, photocatalysis (an advanced oxidative process) is an alternative and sustainable technology for the remediation of these pollutants. The development of new photocatalysts mainly seeks to increase the capacity of the absorption of sunlight, i.e., to expand absorption from the ultra-violet (UV) region to the visible spectrum, since the visible region comprises ~45% of the solar spectrum (Christoforidis e Fornasiero, 2017; Habran, Pontón, *et al.*, 2018; Kapilashrami *et al.*, 2014; Ren *et al.*, 2017; Wang *et al.*, 2020; Zhou *et al.*, 2012). In addition, the maximization of the photogeneration of reactive oxygen species (ROS), such as $^{\bullet}O_2^-$ and $^{\bullet}OH$, plays a key role in photocatalytic activity (Cheshme Khavar *et al.*, 2019; Nosaka e Nosaka, 2017). This maximization occurs through

the increase in the formation of e^{-}/h^{+} pairs and, consequently, their interaction with the O_2 and H_2O molecules to generate $^{\bullet}O_2^{-}$ and $^{\bullet}OH$, respectively.

Thus, the visible light sensitization mechanism denominated as ligand-to-metal charge transfer (LMCT) has gained recognition in the development of TiO_2-based nanomaterials (Luciani, Imparato e Vitiello, 2020) , although the effect of point defects should also be considered (Almeida *et al.*, 2020; Piskunov *et al.*, 2015; Serga *et al.*, 2021). The LMCT mechanism promotes, in theory, efficient photogeneration of superoxide radicals under visible light (Almeida *et al.*, 2020) and consists of the direct injection of e^{-} from the highest occupied molecular orbital (HOMO) of a chelating ligand into the conduction band (CB) of a semiconductor, such as TiO_2 (Zhang, Kim e Choi, 2014). The LMCT mechanism occurs via bonds formed between the chelating ligands (small organic molecules) and the TiO_2 surface. (Almeida *et al.*, 2020; Luciani, Imparato e Vitiello, 2020; Zhang, Kim e Choi, 2014)

The LMCT complex based on TiO_2 and acetic acid (monodentate ligand) showed photodegradation of phenol higher than 90% after 1.5 h exposure to a blue light-emitting diode (LED) lamp (20 W) (Liu *et al.*, 2017a). In addition, another LMCT complex, made of TiO_2 and salicylic acid (bidentate ligand), revealed the potential for selective aerobic oxidation of amines to imines under blue LED irradiation (3 W), having a selective yield of 92% of the desired product, N-benzylidenebenzylamine (Li *et al.*, 2019). Other LMCT complexes of TiO_2 and bidentate ligands, such as glucose (Kim, Lee e Choi, 2015) e alizarin (Li *et al.*, 2020), showed ~ 100% photocatalytic reduction of Cr (VI) during 1 h, under visible light irradiation (Xenon lamp 300 W). Furthermore, the nanocrystalline charge transfer complex (CTC) between TiO_2 and acetylacetone (bidentate) calcinated at 300 °C in air revealed ~ 100% NOx gas photodegradation for 2 h, under visible light irradiation (24 W) (Almeida *et al.*, 2020). Another study on the amorphous TiO_2-Acetylacetone complex revealed ~ 90% degradation of 2,4-dichlorophenol after 24 h, in the absence of irradiation in the presence of high catalyst concentration (1 $g.L^{-1}$) (Aronne *et al.*, 2017). However, as the authors are aware, CTC such as TiO_2-bidentate has not been investigated thus far, for photocatalytic applications in drug degradation.

Moreover, the understanding of the role of reactive radicals on the photocatalytic activity of these complexes is not fully understood. Experimental

analyses performed by electron paramagnetic resonance (EPR) (Almeida *et al.*, 2020; Ritacco *et al.*, 2021) and theoretical studies based on density functional theory (DFT) reported for the TiO_2-Acetylacetone (Ritacco *et al.*, 2021) and TiO_2-Thiosalicylic acid (Milićević *et al.*, 2017) complexes demonstrate the capacity of the LMCT mechanism to produce superoxide ($^{\bullet}O_2^-$). On the other hand, Fourier transform infrared (FTIR) analysis reveals the presence of adsorbed hydroxyls on the surface of these LMCT complexes (Almeida *et al.*, 2020; Kim, Lee e Choi, 2015; Li *et al.*, 2019; Liu *et al.*, 2017; Ritacco *et al.*, 2021) that may participate in the formation of $^{\bullet}OH$, if electronic holes exist in the valence band (VB) of TiO_2. However, to the best of our knowledge, the individual potential of ROS in the LMCT systems has not been evaluated for photocatalytic applications. The ROS scavengers have been, however, already employed to other photocatalysts in photocatalytic measurements in the liquid medium to assess the individual potential of each ROS (Abd Elkodous *et al.*, 2021; Lam *et al.*, 2014; Moraes, de, Torezin, *et al.*, 2020; Sousa, de *et al.*, 2020; Wang *et al.*, 2020; Zhang, Li e Liu, 2020).

The measurements of photocatalytic degradation of chlorophenol and tetracycline by CTC, combined with the use of $^{\bullet}O_2^-$ and $^{\bullet}OH$ scavengers, would clarify the actual potential of each ROS in the photocatalytic abatement.

Photocatalytic degradation in a liquid medium under visible light irradiation is mostly carried out with a light power superior to 300 W (Alam *et al.*, 2019; Li, F. *et al.*, 2018; Myilsamy *et al.*, 2016; Sousa, de *et al.*, 2020). The high energy consumption of the lamps follows the opposite path to the sustainable nature of photocatalysis. Therefore, a lamp with reduced power such as residential lamps of 26 W will be applied in this research for degradation of aqueous pollutants.

This study has as the main goals (1) evaluation of the potential of TiO_2-Acetylacetone CTC calcinated at 300 °C in air, for photodegradation of chlorophenol and tetracycline under reduced power visible light (26 W) and (2) understanding of ROS ($^{\bullet}O_2^-$ and $^{\bullet}OH$) roles, in photocatalysis performed by TiO_2-Acetylacetone, using scavengers such as benzoquinone and isopropanol. Furthermore, the volatilization profile of TiO_2-ACAC CTC was studied up to 550 °C by thermogravimetric analysis coupled with mass spectroscopy (TGA-MS) to confirm the presence of acetylacetone at temperatures above 150 °C.

4.2.
Materials and methods

4.2.1. Materials

All reagents were purchased from Sigma Aldrich and used as obtained. Titanium isopropoxide ($Ti(OiPr)_4$, 97%), acetylacetone (ACAC, ≥ 99%), ethanol (≥ 99.8%), and nitric acid (65%) were used for the synthesis of TiO_2-ACAC CTC nanoparticles. The aqueous pollutants were chlorophenol (4-CP, ≥ 99%) and tetracycline (TC, ≥ 98%). Benzoquinone (BQ, ≥ 98%) and isopropanol (IPA, ≥ 99.5%) were used as ROS scavengers.

4.2.2. Synthesis of TiO_2-Acetylacetone charge transfer complex

The synthesis of TiO_2 anatase nanoparticles coupled with acetylacetone (CTC) was carried out by the sol-gel route as reported by Scolan and Sanchez (Scolan e Sanchez, 1998). In addition, as previously reported [12,16] the molar ratios for hydrolysis (H= $[H_2O]/[Ti]$), acidity (H^+= $[H^+]/[Ti]$) and complexing (A=[ACAC]/[Ti]) were kept at 100, 0.027 and 2, respectively, to produce TiO_2-ACAC xerogel with mean crystal size ~ 2.5 nm.

In the adopted procedure, 30 mL of $Ti(OiPr)_4$ were added dropwise into a solution of 20 mL of ACAC with 100 mL of ethanol (1:5 v/v). The obtained yellow solution remained under magnetic stirring for 40 min at room temperature. Afterward, 180 mL of HNO_3 solution (0.015 M) were dropped slowly into the yellowish solution under continuous stirring. The dark orange solution obtained was heated to 60 °C and kept under magnetic stirring for 8 h. Next, the sol of TiO_2 was dried overnight in Petri dishes at room temperature and a gel was formed (TiO2-A-RT). Finally, the gel was dried at 100 °C overnight to obtain a red-yellowish xerogel of TiO_2-Acetylacetone (TiO_2-ACAC). The TiO_2-ACAC xerogel, grounded in an agate mortar, was calcined in air at 300 °C, for 2 h, in a Tubular Maitec-INTI FET 1600/H furnace. The as-prepared powder was denoted TiO_2-A300.

4.2.3. Thermogravimetric analysis coupled with mass spectroscopy (TGA-MS)

Thermogravimetric analysis (TGA) and differential scanning calorimetry (DSC) were performed on a Perkin-Elmer Simultaneous Thermal Analyzer STA-6000, under synthetic air flow (130 mL.min-1), with a heating rate of 10 °C.min^{-1} and within the temperature range between 30 °C and 550 °C. A mass of ~ 25 mg was used.

To identify the volatilized species from TiO_2-ACAC, and confirm the presence of ACAC, in the TiO_2-A300 sample, a mass spectrometer OmniStar / ThermoStar-GSD 320 O3 (Pfeiffer Vacuum) was coupled to the STA-6000. The m/z range until 105 was scanned with the measuring time of 0.5 s.amu^{-1}.

4.2.4. Measurement of the photodegradation of chlorophenol and tetracycline and the efficiency of ROS

The photocatalytic potential of TiO_2-A300 for degradation of 5 mg.L^{-1} of 4-CP and TC under visible light irradiation was evaluated. In accordance to (Almeida *et al.*, 2020) the inorganic part of TiO_2-A300 CTC is composed from nanocrystalline anatase. Other two materials, TiO_2-A-RT and TiO_2-ACAC (where inorganic part also consists of nanocrystalline anatase) were not evaluated since they previously showed inferior photocatalytic efficiency (Almeida *et al.*, 2020). In addition, a measurement of the TC photodegradation until stabilization of TC abatement was performed.

All measurements were performed with 0.2 g.L^{-1} of the photocatalyst. The light source used was a DULUX D/E 26 W residential fluorescent lamp with an irradiance of 0.23 W.cm^{-2} and an emission of light in the wavelength range from 400 nm to 700 nm (Figure 28, Appendix A). The photocatalytic system is shown in Figure 29 (Appendix A). The lamp is housed in a cylindrical quartz bulb (length 11 cm, internal diameter 3.2 cm, and thickness 0.15 cm) unable to absorb visible light. The photoreactor was immersed in a bath with cold water circulation to maintain the system at room temperature. The photocatalytic tests were carried out under vigorous magnetic stirring in two stages. In the first stage, the pollutant and the photocatalyst were kept in the dark for 1 h to attain the absorption–desorption equilibrium. After this period, the lamp was turned on, and 5 mL aliquots of

supernatant were acquired at intervals of 1 h for 6 h. The supernatant was filtered through a Merck Millipore filter (0.45 μm) and analyzed by an Agilent UV-Vis spectrophotometer (model 8453). The absorption at the wavelengths of 224 nm and 358 nm was accompanied for photodegradation of 4-CP and TC during the test time, respectively. The observed reduction in these wavelengths for each pollutant was used as input to determine the percentage of photodegradation performed by TiO_2-A300 CTC, as seen in Figure 30 (Appendix A) and Table 2 (Appendix A). The degradation data obtained were presented through the mean value together with the respective standard deviations (Table 2, Appendix A) since all photocatalytic tests were performed in triplicate to ensure repeatability of results.

The ROS efficiency in TiO2-ACAC CTC was evaluated by adding the scavenger molecule BQ (5.4 $mg.L^{-1}$; 0.05 $mmol.L^{-1}$) to inhibit the participation of the $^{\bullet}O_2^-$ radical in the degradation of 4-CP and TC. On the other hand, the addition of the IPA scavenger (6.0 $mg.L^{-1}$; 0.1 $mmol.L^{-1}$) was performed to inhibit the participation of the $^{\bullet}OH$ radical. The scavengers were added to the 5.0 $mg.L^{-1}$ solutions of 4-CP or TC before starting the photo-catalytic tests to ensure a mass ratio close to 1:1 between the pollutant and the scavenger.

4.3. Results

4.3.1. Evaluation of TiO_2-ACAC CTC Volatilization Profile by TGA-MS

TiO_2-A-RT, TiO_2-ACAC, and TiO_2-A300 were analyzed by TGA-MS to confirm the presence of ACAC above 150 °C through the release of ACAC fragments or the release of the entire ACAC molecule on heating.

The TGA curve of the TiO_2-A-RT sample (Figure 10a) revealed an expressive mass loss of 29.5 wt.% at temperatures below 150 °C due to dehydration of the material. Furthermore, the mass loss between 150 °C and 450 °C is associated with the release of acetylacetone, as documented by TGA-MS results (Figure 10b). The mass loss of organic species between 150 °C and 450 °C was ~15 wt.% and approximately equal to the mass loss of the TiO_2-ACAC xerogel for the same temperature region (Almeida *et al.*, 2020). The TGA curves of TiO_2-ACAC and TiO_2-A300 and their first derivatives (DTG) (Figure 31, Appendix A) were in

accordance with the results previously reported by Almeida et al. (Almeida *et al.*, 2020).

Figure 10b illustrates the evolution profiles of released gases as a function of tempera-ture for the TiO_2-A-RT sample. In the first temperature stage of volatilization between 30 °C and 150 °C, species with m/z of 17, 18, 19, and 20, corresponding to water were detected (Acik *et al.*, 2009). In the second temperature stage between 150 °C and ~ 265 °C, the m/z of 43, 44, and 58 were identified, owing to the release of acetyl ions ($CH_3C{\equiv}O+$), CO_2, and acetone, respectively (Bowie *et al.*, 1966). Bowie et al. (Bowie *et al.*, 1966) showed that m/z of 43 and 58 are associated with the fragmentation of the ACAC molecule, where the most intense peak of the ACAC volatilization in the mass spectrum is m/z 43, belonging to acetyl ions. Acetone and CO_2 release in this temperature range are in accordance with Acik et al. (Oja Açik *et al.*, 2007) who observed the release of both species from the amorphous TiO_2-ACAC xerogel. In the third temperature region of mass loss between 300 °C and 450 °C, an increase of CO_2 release was identified (m/z = 44 and 45) together with water release, which is in accordance with the observation of Acik et al. (Oja Açik *et al.*, 2007) and Madarász et al. (Madarász *et al.*, 2009) for amorphous TiO_2-ACAC xerogel and crystalline titanium oxobis(acetylacetonate), respectively.

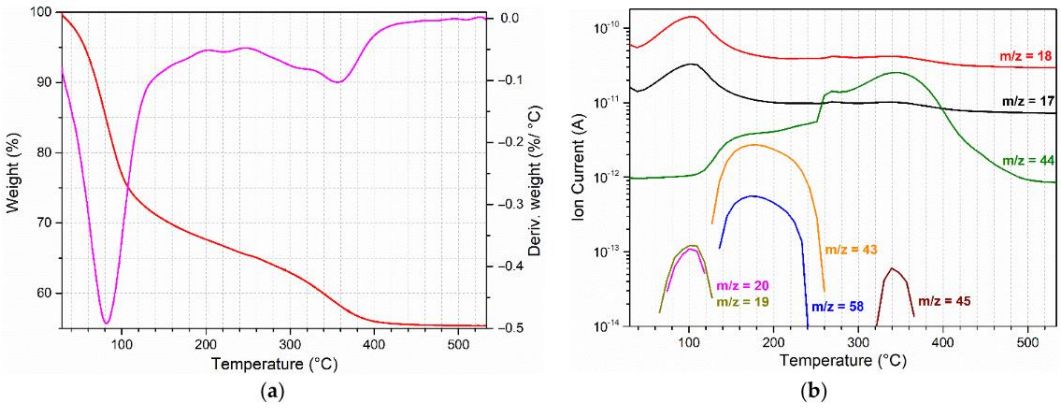

Figure 10: (a) TGA and DTG curves of TiO_2-A-RT sample; (b) Evolution profiles of gaseous species as monitored by TGA-MS for TiO_2-A-RT sample.

The profiles of gaseous species released from nanocrystalline TiO_2-ACAC and TiO_2-A300 samples are shown in Figure 11. The volatilization stages of TiO2-ACAC (Figure 11a) follow a similar path as TiO_2-A-RT (Figure 10). TiO^2-ACAC water release occurs in the temperature range between 30 °C and 150 °C, followed

by a two-stage release of molecules due to ACAC oxidation above 150 °C. In the interval from 150 °C to ~ 265 °C, only acetyl ions (m/z = 43) and CO_2 (m/z = 44) were released. In addition, in the third temperature stage (300 °C –450 °C), CO_2 (m/z = 44 and 45) and water release were reported. The absence of acetone release in the TiO_2-ACAC xerogel probably occurred due to overnight drying at 100 °C, reducing the excess ACAC content in the sample.

On the other hand, the TGA-MS data of the TiO_2-A300 sample (Figure 11b) revealed only two distinct temperature stages of gases volatilization. The first stage between 30 °C and 150 °C was related to a release of water (m/z = 17, 18 e 19, and 20), while the second stage between 300 °C and 450 °C was due to CO_2 and water release. The volatilization step of the ACAC oxidation products above 300 °C, for all studied TiO_2-ACAC CTC samples, indirectly contributes to proving that the ACAC is responsible for the sensitization of TiO_2 in visible light in the samples calcined at 300 °C, as previously reported (Almeida *et al.*, 2020).

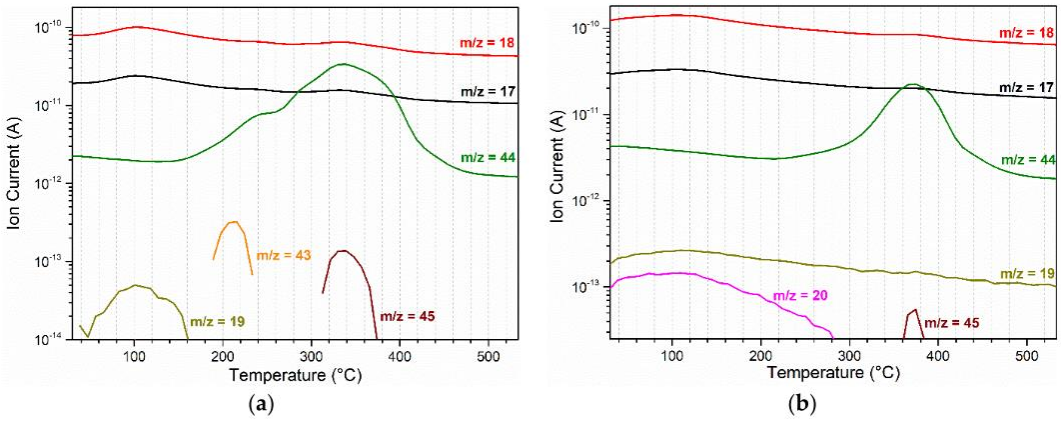

Figure 11: Evolution profiles of gaseous species as monitored by TGA-MS for (a) TiO_2-ACAC and (b) TiO_2-A300 samples.

4.3.2. Chlorophenol Photodegradation and ROS Efficiency under Reduced Power Visible Light

Figure 12 shows the photocatalytic degradation of chlorophenol using TiO_2-A300 CTC during the period of 6 h. Photolysis did not promote pollutant degradation (green curve).

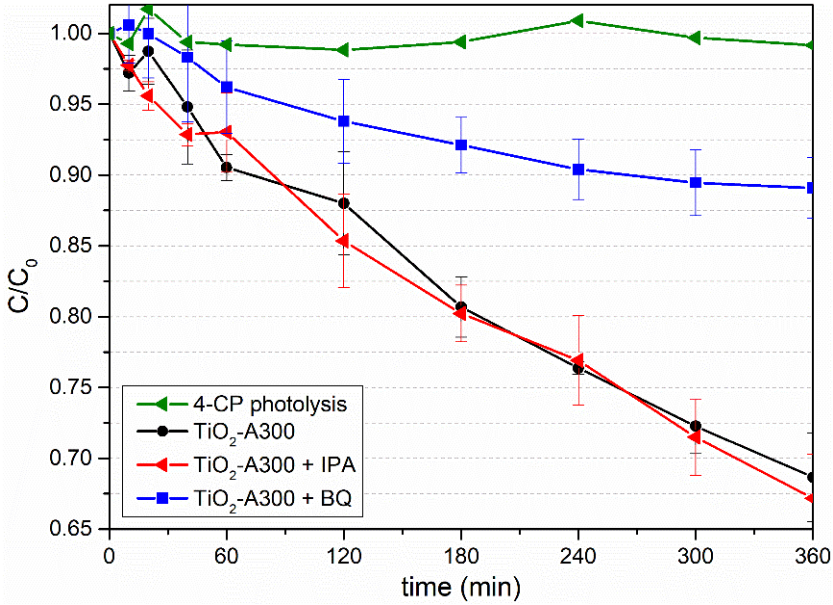

Figure 12: Chlorophenol photodegradation by TiO_2-A300 photocatalyst with and without the addition of scavengers. The green curve stands for photolysis.

The TiO_2-A300 CTC revealed photocatalytic abatement of 31.3% ± 3.1% for 4-CP after 6 h (Figure 12). Li et al. (Li, F. *et al.*, 2018) quantified visible light abatement of 4-CP as 29.9% after 2 h using graphene grafted titania/titanate nanosheets under UV-Vis light of 500 W for the same concentrations of pollutants and photocatalyst used in our study. Furthermore, 4-CP degradation using TiO_2-A300 was nearly half of the degradation reported by Li et al. (Li, F. *et al.*, 2018) after 2 h, however, with a light source with 20 times lower power.

The addition of the $^{\bullet}OH$ radical scavenger (IPA) did not significantly impact the degradation efficiency of TiO_2-A300 (Figure 12). The observed photodegradation of 4-CP was 32.8% ± 3.1% after 6 h and was within the error of the degradation measured for TiO_2-A300 without the addition of the IPA scavenger. On the other hand, Moraes et al. (Moraes, de, Torezin, *et al.*, 2020) revealed that with the addition of the IPA, the degradation of 4-CP (10 $mg.L^{-1}$) using nanometric anatase (0.2 $g.L^{-1}$) was about two times lower in comparison to the degradation without the addition of the IPA, however, under UV light and after 3 h. Therefore, these data indicate that hydroxyl radicals played an important role in the degradation of 4-CP for TiO_2 under UV light, since it promoted the formation of e^-/h^+ pairs and, consequently, $^{\bullet}OH$ radials. The results reported by Moraes et al. [4] are in accordance with studies that show that $^{\bullet}OH$ radicals have a dominant role in photodegradation of 4-CP [32,38]. However, for TiO_2-A300 CTC under visible

light, it was not possible to detect the role of •OH radicals in the photodegradation of 4-CP. Therefore, our results strongly indicate that TiO_2-A300 CTC does not efficiently generate •OH radicals under visible light.

On the other hand, the addition of the $•O_2^-$ scavenger (BQ) caused a strong reduction of the photodegradation potential of TiO_2-A300 (Figure 12). The 4-CP abatement after the addition of BQ was only 10.9% ± 2.1% after 6 h interval. Therefore, the $•O_2^-$ plays an important role in the photocatalytic activity of TiO_2-A300 during the degradation of 4-CP. According to Su et al. (Su *et al.*, 2012) and Fónagy et al. (Fónagy, Szabó-Bárdos e Horváth, 2021), benzoquinone is predominantly reduced by $•O_2^-$ radicals and e^- and, consequently, degraded. Therefore, $•O_2^-$ generated by TiO_2-A300 CTC preferentially degrades BQ molecules instead of degrading 4-CP, as illustrated in Figure 13. The expressive 76.7% ± 2.1% BQ degradation and low 4-CP degradation after 6 h demonstrate the efficient generation of $•O_2^-$ radicals under visible light from TiO_2-A300.

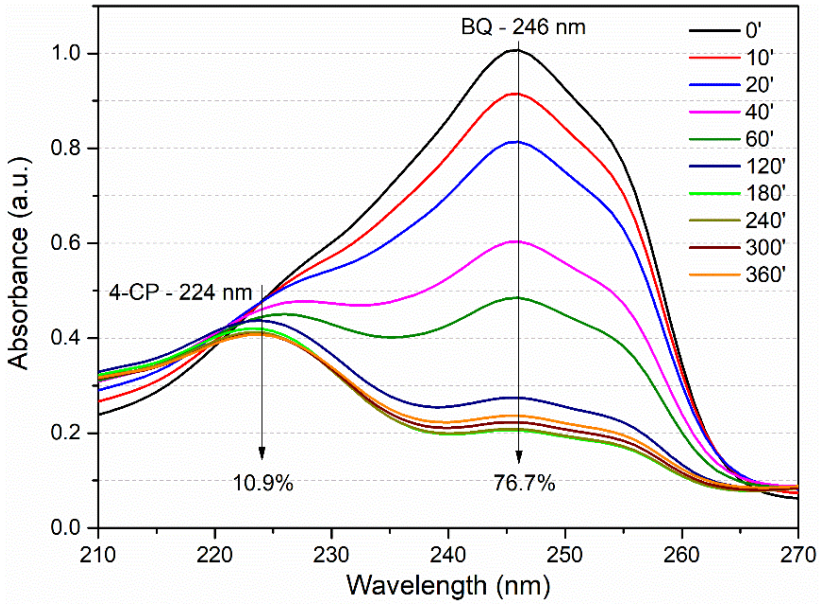

Figure 13: The absorbance of the BQ band situated at 246 nm and the 4-CP band at 224 nm, over time.

4.3.3. Tetracycline Photodegradation and ROS Efficiency under Reduced Power Visible Light

Figure 14 shows the photocatalytic degradation of tetracycline using TiO_2-A300. The photolysis (green curve) did not show pollutant degradation during the test time.

The TiO_2-A300 CTC showed a high photocatalytic degradation of 68.6% ± 3.4% of TC after 6 h (Figure 14). In addition, the maximum photodegradation of TC up to the abatement stabilization was 83% after 11 h (Figure 32, Appendix A). This maximum abatement of TC from TiO_2-A300 was similar to the 86.7% degradation reported by Wang et al. (Wang *et al.*, 2020) for the WO_3-TiO_2 core-shell heterostructure decorated by Pt nanoparticles (0.08 $g.L^{-1}$) under UV-Vis light at 300 W after 2 h. However, the performance of TiO_2-A300 was achieved with 11.5 times lower light power with the use of visible instead of UV light and without the use of precious metals.

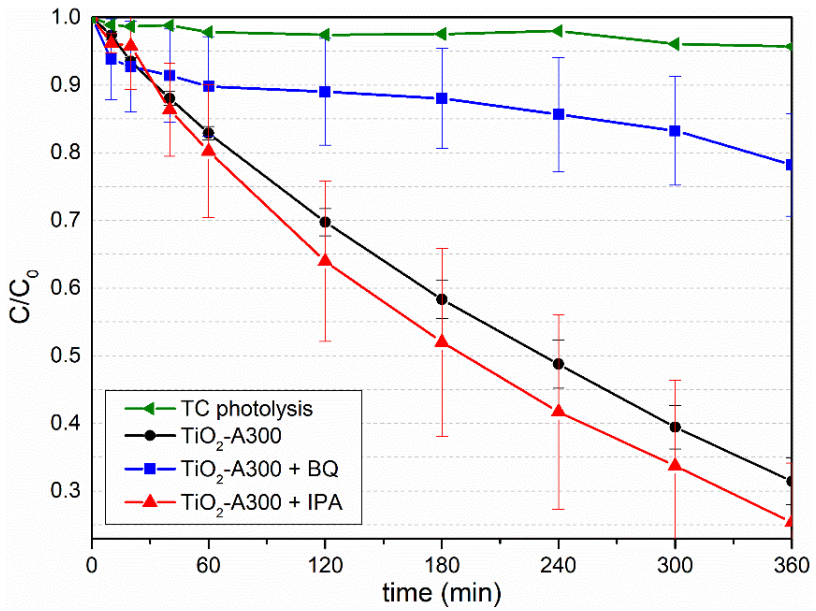

Figure 14: Tetracycline photodegradation by TiO_2-A300 with and without the addition of scavengers. The green curve stands for photolysis.

The use of isopropanol as the $^{\bullet}OH$ scavenger revealed an abatement of 74.6% ± 8.7% after 6 h, within the error bars of the degradation without the addition of the IPA scavenger. In contrast, TC degradation under UV-Vis light by heterostructures, such as ZnO/GO/Ag_3PO_4 (Zhu *et al.*, 2020), Ag_3PO_4/AgBr/g-C_3N_4 (Yu *et al.*, 2020), and $Bi_2W_2O_9$/g-C_3N_4 (Obregón *et al.*, 2020) revealed a decrease in TC

abatement due to the addition of IPA. These results reported for the heterostructures indicate that •OH radicals contribute to the degradation of TC when generated [5]. Therefore, the result obtained for TiO_2-A300 suggests that TiO_2-A300 is not capable of producing •OH under visible light.

The TC photodegradation with the addition of BQ was significantly reduced to 21.8% ± 7.6% using TiO_2-A300 after 6 h (Figure 14). The reduction observed in our study agrees with the literature, where different ceramic heterojunctions showed low TC degradation efficiency with the addition of BQ under high power UV or UV-Vis light sources (>300 W) (Lu *et al.*, 2021; Wang *et al.*, 2020; Yu *et al.*, 2020). He et al. (He, Kai e Ding, 2021) reported that $\bullet O_2^-$ and H2O2 radicals are capable of attacking the benzene ring of tetracycline, oxidizing the N-dimethyl group and the -C(O)NH_2 group, suggesting that $\bullet O_2^-$ plays an important role in the photodegradation pathway of TC. Therefore, the TC degradation behavior observed in Figure 5 is mainly due to the efficient generation of $\bullet O_2^-$ radicals by TiO_2-A300 CTC.

4.4. Discussion

The TGA-MS results of TiO_2-A-RT, TiO_2-ACAC, and TiO_2-A300 samples evidenced the fragments of ACAC oxidation release, such as acetyl ions, acetone, CO_2, and water between 150 °C and ~ 265 °C, while only CO_2 and water release were detected at higher temperatures between 300 °C and 450 °C (Figure 10b and Figure 11). Two distinct steps of ACAC fragments release for TiO_2-A-RT and TiO_2-ACAC, between 150 °C and 450 °C, are in accordance with the TGA-MS and FTIR-MS analysis reported by Acik et al. (Oja Açik *et al.*, 2007) for amorphous TiO_2-ACAC xerogel. The volatilization profile of ACAC from TiO_2-A300 (Figure 11b) converges well with the mass loss reported by Almeida et. al. (Almeida *et al.*, 2020) for the same material since CO_2 and water were released as ACAC oxidation products above 300 °C. Therefore, it is worth noting for the understanding of the CTC mechanism that nanocrystalline TiO_2-ACAC samples preserved a part of ACAC when calcined at temperatures higher than 150 °C, such as 300 °C, as applied for TiO_2-A300.

The results on the photocatalytic activity of TiO_2-A300 support the hypothesis that a TiO_2-ACAC CTC would be able to degrade aqueous pollutants under reduced power visible light. The TiO_2-A300 showed photocatalytic potential for degradation of both aqueous pollutants 4-CP and TC. In addition, TiO_2-A300 did not show adsorption of pollutants in the dark 1 h before turning on visible light (Figure 33, Appendix A). Therefore, the abatement of all the pollutants was the result of the photocatalytic activity of TiO_2-ACAC CTC.

In our previous study (Almeida *et al.*, 2020), TiO_2-A300 revealed a high efficiency (~100%) for photo-degradation of NO_x gas (100 ppm) during 2 h under reduced power visible light (24 W). Therefore, the results presented in the current research additionally increase the photocatalytic applicability of TiO_2-ACAC CTC.

Zhu et al. (Zhu *et al.*, 2020) reported 96.3% degradation of TC (30 $mg.L^{-1}$) after 75 min, with ~50% of the reported degradation values associated with the adsorption phenomenon in the dark. The authors used for this purpose $ZnO/GO/Ag_3PO_4$ photocatalyst (1 $g.L^{-1}$) under low power visible light (65 W). Therefore, photodegradation of TC reported in our study after 6 h (68.6%) was higher than documented by Zhu et al. (46.3%) (Zhu *et al.*, 2020) with 2.5 lower visible light power and using four times less photocatalyst. Additionally, the capacity of degradation of TC is ~two times higher than that observed for 4-CP using TiO_2-A300, after 6 h, indicating a distinct participation of ROS in the degradation of these two pollutants.

ROS Generation Efficiency in TiO_2-A300 CTC

One of the main goals of our study was understanding the roles of ROS ($^{\bullet}O_2^-$ and $^{\bullet}OH$) in photocatalysis performed by TiO_2-A300 CTC, using BQ and IPA scavengers. The photodegradation of 4-CP and TC under visible light with the addition of $^{\bullet}O_2^-$ scavenger confirms the efficient generation of $^{\bullet}O_2^-$ radicals by TiO_2-ACAC CTC (Figures 12 and 14), in accordance with the EPR characterization and DFT studies carried out on LMCT complexes (Almeida *et al.*, 2020; Milićević *et al.*, 2017; Ritacco *et al.*, 2021). On the other hand, the $^{\bullet}OH$ radicals were not efficiently generated by TiO_2-A300 CTC under visible light, resulting in the lower photodegradation of 4-CP than the photodegradation of TC, since $^{\bullet}OH$ radicals are the dominant ROS in the 4-CP photodegradation (Li, F. *et al.*, 2018; Moraes, de,

Torezin, *et al.*, 2020; Moraes, de, Valim, *et al.*, 2020), while $^{\bullet}O_2^-$ radicals play a key role in TC degradation [5].

Figure 15 represents an update of the photocatalytic reactions conducted by TiO_2-A300 CTC for the ROS generation and consequent degradation of 4-CP and TC. Additionally, the photocatalytic reactions for hydrogen production are also presented in Figure 15.

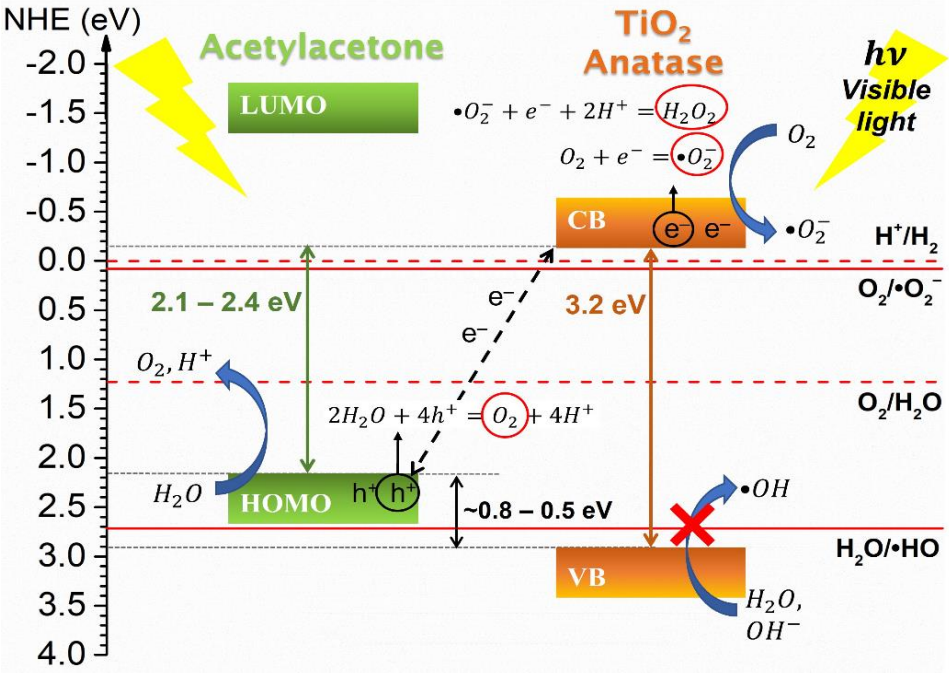

Figure 15: Scheme of electronic bands in TiO_2-A300 CTC and photocatalytic reactions for ROS generation. The position of BV and BC of anatase at redox potential scale, in accordance with normal hydrogen electrode (NHE), was adopted from literature (Christoforidis e Fornasiero, 2017; Ren *et al.*, 2017), as well as the positions of the ROS species. The position of HOMO of acetylacetone was previously established in (Almeida *et al.*, 2020). The position of LUMO of acetylacetone was arbitrarily added, since it does not have a role in photocatalytic and water splitting events and is higher than 3.2 eV.

Figure 15 shows the electron transfer from ACAC HOMO to TiO_2 (anatase) CB and, consequently, the formation of $^{\bullet}O_2^-$ radicals due to the reaction between O_2 adsorbed on the surface of anatase and free e^- from CB (Equation 1).

Equation 1: photogeneration of $^{\bullet}O_2^-$ radicals

$$O_2 + e^- \rightarrow {}^{\bullet}O_2^-$$

The efficient $^{\bullet}O_2^-$ generation is also a consequence of a high O_2 presence in the reaction medium (Ren *et al.*, 2017). A possible additional explanation for the O_2 presence in an aqueous solution is the water splitting mechanism (Equation 2)

(Christoforidis e Fornasiero, 2017; Ren *et al.*, 2017). The h^+ generated in the HOMO of the ACAC may promote water splitting, *i.e.*, decomposing H_2O into O_2 and H^+ through an oxidation half reaction as shown in Figure 15.

Equation 2: Water splitting mechanism

$$2\ H_2O + 4\ h^+ \rightarrow O_2 + 4\ H^+$$

Additionally, the efficient production of $^{\bullet}O_2^-$ radicals can also form H_2O_2 (Mamaghani, Haghighat e Lee, 2017; Ren *et al.*, 2017), which is another ROS capable of degradation of aqueous pollutants due to its ability to attack benzene rings and the N-dimethyl group (He, Kai e Ding, 2021). The energy barrier of the formation of H_2O_2 from $^{\bullet}O_2^-$ radicals (Equation 3) is 0.3 eV below the normal hydrogen electrode potential (NHE) (Nosaka e Nosaka, 2017). Therefore, a part of $^{\bullet}O_2^-$ generated by TiO_2-A300 can be transformed into H_2O_2 and can continue to degrade 4-CP and TC.

Equation 3: Photogeneration of hydrogen peroxide

$$^{\bullet}O_2^- + e^- + 2\ H^+ \rightarrow O_2 + H_2O_2$$

As seen in Figure 15, the arrangement of CB of TiO_2 and HOMO of ACAC in the TiO_2-ACAC CTC may provide photocatalytic production of H_2 from water splitting. The electron holes from HOMO of ACAC are capable of oxidizing water, forming H^+ (Equation 2), and the e^- in the CB of TiO_2 may reduce H^+ to H_2 (Equation 4).

Equation 4: Hydrogen production

$$2\ H^+ + 2\ e^- \rightarrow H_2$$

Finally, some previous studies demonstrated the photocatalytic potential of Z-scheme heterostructures based on WO_3 (Wang *et al.*, 2020; Zhi *et al.*, 2020), SnO_2 (Li, Y. *et al.*, 2018), and $BiVO_4$ (Zhou *et al.*, 2017) for TC and NOx degradation and hydrogen production under UV-Vis light. These low-bandgap semiconductors can absorb visible light and generate $^{\bullet}OH$ radicals via VB and CB with positive redox potential. The Z-scheme heterojunction consists of the recombination of the CB electrons of these low-bandgap semiconductors with the VB of another semiconductor with a lower positive redox potential, providing a

reduction in the recombination rate of e^{-}/h^{+} pairs in the low-bandgap semiconductors, such as WO_3, SnO_2, and $BiVO_4$ and, consequently, an increase in the formation of •OH radicals. Therefore, coupling TiO_2-ACAC CTC with semiconductors capable of generating •OH radicals under visible light may maximize the generation of ROS and increase of photocatalytic efficiency of these new heterojunctions.

4.5. Conclusions

The TGA-MS indirectly proved the presence of ACAC on TiO_2-A-RT, TiO_2-ACAC xerogel, and TiO_2-A300 at temperatures higher than 150 °C. The release of acetyl ions and acetone between 150 °C and ~265 °C was detected, while at temperatures above 300 °C, and not higher than 450 °C, the release of CO_2 and water was detected as the products of ACAC oxidation.

The TiO_2-A300 photodegrades 4-CP and TC under reduced power visible light. The photocatalytic abatement of tetracycline (68.6%) was ~two times higher than that observed for chlorophenol (31.3%) after 6 h, indicating a distinct potential of ROS in the degradation of these pollutants.

The addition of BQ scavenger on the photocatalytic degradation of 4-CP and TC proved TiO_2-A300 CTC to be a powerful source of superoxide ($•O_2^-$) radicals under visible light, promoting a high photodegradation of TC (68.6%) after 6 h. However, the •OH scavenger does not promote the reduction in photodegradation of 4-CP and TC, proving TiO_2-ACAC CTC is not an efficient generator of •OH radicals under visible light.

The photocatalytic potential reported for TiO_2-A300 may stimulate new studies on hydrogen production process from water splitting under visible light due to the redox potential arrangement of CB of TiO_2 and HOMO of ACAC. Furthermore, the development of heterostructures based on TiO_2-A300 CTC, and similar CTC, can increase the generation of ROS through coupling with semiconductors capable of generating •OH under visible light and, therefore, capable of formation of more powerful photocatalysts.

5.
Enhanced photocatalytic activity of TiO_2 anatase nanoparticles modified with malonic acid under reduced power visible light: synthesis, characterization and degradation of tetracycline and chlorophenol

5.1
Background

TiO_2-based nanomaterials are among the most promising alternatives for photocatalytic applications such as environmental remediation (Ren *et al.*, 2017; Saravanan *et al.*, 2022; Talaiekhozani *et al.*, 2021) or hydrogen production (Christoforidis e Fornasiero, 2017; Tahir, Tasleem e Tahir, 2020). Chemical stability, non-toxicity, relatively low cost, and mainly, the position of the valence band (VB) and conduction band (CB) relative to the normal hydrogen electrode potential (NHE) placed TiO_2 at this prominent position (Christoforidis e Fornasiero, 2017; Ren *et al.*, 2017; Wu, Lin e Hu, 2021). The electronic holes (h^+) at the VB are able to split the H_2O molecule and produce reactive oxidant species (ROS) such as $OH^{\bullet}$ (Nosaka e Nosaka, 2017). On the other hand, the free electrons at the CB are able to produce H_2 and ROS $^{\bullet}O_2^-$ species (Nosaka e Nosaka, 2017), maximizing photocatalytic activity under ultraviolet (UV) light (Christoforidis e Fornasiero, 2017; Ren *et al.*, 2017). However, UV light represents only 4-5% of the total solar spectrum (Wu, Lin e Hu, 2021) and, like most ceramics, TiO_2 has inefficient absorption of visible light. Therefore, the improvement of the sensitization in ceramic oxides over the visible light range is one of the driving forces for the development of novel TiO_2-based photocatalysts. (Christoforidis e Fornasiero, 2017; Ren *et al.*, 2017; Saravanan *et al.*, 2022; Tahir, Tasleem e Tahir, 2020; Talaiekhozani *et al.*, 2021; Wu, Lin e Hu, 2021)

Coupling with narrow bandgap ceramic semiconductors (*i.e.* bandgap < 3.2 eV), such as WO_3 (Lashuk *et al.*, 2022) and Cu_2O/CuO (Ansari, Sheibani e Fernandez-García, 2022), coating with metallic nanoparticles, such as Fe (Costa *et al.*, 2015), Cr (Mancuso *et al.*, 2022) and Au (Chen *et al.*, 2020), or, more recently,

coating with small organic molecules (chelating ligands), such as catechol (Higashimoto *et al.*, 2015), salicylic acid (Božanić *et al.*, 2019) and acetylacetone (Almeida *et al.*, 2020; Hong *et al.*, 2022; Sannino *et al.*, 2015), are alternatives to overcome this intrinsic disadvantage of TiO_2. However, an efficient photocatalyst must also present a low recombination rate between e^-/h^+ pairs and high surface area to improve interaction with environmental pollutants and as well as with molecules such as H_2O, O_2, and OH^-, and consequently, to permit an efficient generation of ROS or production of H_2 (Almeida *et al.*, 2022; Habran, Pontón, *et al.*, 2018).

Two features associated with chelating ligands make them a promising solution for maximizing photocatalytic properties of TiO_2-based nanomaterials. The first is the ligand-to-metal charge transfer (LMCT) mechanism, *i.e.*, the direct injection of e^- from the highest occupied molecular orbital (HOMO) of a chelating ligand (monodentate or bidentate) into the CB of TiO_2 under visible light (Zhang, Kim e Choi, 2014). The second feature is the possibility of synthesizing crystalline nanoparticles with a high surface area (>130.0 $m^2.g^{-1}$) by adding chelating ligands in excess during the synthesis process (Almeida *et al.*, 2020; Liu *et al.*, 2017).

Most of the charge transfer complexes (CTC) between TiO_2 and chelating ligands are formed through the coating of commercial materials or at a stage posterior to the synthesis of TiO_2 (Luciani, Imparato e Vitiello, 2020), promoting partial absorption of visible light and an optical bandgap of 2.4 eV (Higashimoto *et al.*, 2015; Li *et al.*, 2019; Schechtel *et al.*, 2019; Zhang, Kim e Choi, 2014). On the other hand, the incorporation of the bidentate ligands such as acetylacetone (ACAC) (Almeida *et al.*, 2020, 2022; Gil-Londoño, Krambrock, *et al.*, 2023; Habran, Pontón, *et al.*, 2018), glutaric acid (Gil-Londoño, Cremona, *et al.*, 2023) or acetic acid (Liu *et al.*, 2017) into sol-gel synthesis allowed the preparation of nanocrystalline anatase CTCs capable of absorbing along the visible spectrum when calcined at 300 °C. Furthermore, the calcination of nanocrystalline xerogel at mild temperatures (< 300 °C) permits control of the content of organic material adsorbed and bound to the TiO_2 surface, while preserving high surface area. (Almeida *et al.*, 2020; Liu *et al.*, 2017).

Our research group reported, recently, that calcination of TiO_2-Acetylacetone xerogel at 300 °C in air for 2 h preserved the surface area at 137.0 $m^2.g^{-1}$ while

reducing the apparent bandgap from 2.4 eV to 1.4 eV (Almeida *et al.*, 2020). As a consequence, TiO_2-ACAC CTC calcined at 300 °C (a brown powder) showed high photocatalytic activity under reduced visible light power (24-26 W) converting ~ 100% of NO_x (100 ppm) into NO_3^- during 1 h (Almeida *et al.*, 2020) and degrading partially chlorophenol and tetracycline (Almeida *et al.*, 2022). Furthermore, recently, Gil-Londoño et al. (Gil-Londoño, Cremona, *et al.*, 2023) reported a new CTC between TiO_2 and glutaric acid, calcined at 270 °C for 2 h under static air (TiO_2-GA-270), capable to photodegrade, after 6 h, 78.4% of tetracycline (5 $mg.L^{-1}$) using 100 $mg.L^{-1}$ of TiO_2-GA-270 under reduced visible light power (26 W). The TiO_2-GA-270 CTC presents a brown color (with an apparent bandgap of 1.30 eV) and the authors concluded that the visible absorption over the entire visible range was a result of a synergy between the LMCT mechanism and the electronic transitions promoted by the presence of oxygen vacancies sublevels into the bandgap of TiO_2. Another study, reported by Liu et al. (Liu *et al.*, 2017), showed a similar feature for nanocrystalline CTC formed between TiO_2 and acetic acid (TiO_2-AA) synthesized by the sol-gel route. The calcination of TiO_2-AA xerogel at 300 °C in a hypoxic atmosphere (5% O_2, 95% N_2, 100 $mL.min^{-1}$) for 2 h produced a brown powder with the surface area of 255.9 $m^2.g^{-1}$ and improved photocatalytic potential for degradation of phenol, close to ~ 90%, after 90 min under blue LED irradiance (410-500 nm, 20W).

However, the number of bidentate ligands used in sol-gel synthesis of TiO_2 with the simultaneous goals of combining maximum visible sensitization and high surface area is still scant.

For example, Bakre and Tilve (Bakre e Tilve, 2017) have reported sol-gel synthesis of anatase nanoparticles, by adding dicarboxylic acid, with surface areas higher than 250.0 $m^2.g^{-1}$ even after calcination of the xerogels at 500 °C in air for 3 h. The presence of carboxylate bridges (bidentate bonds) between the dicarboxylic acid and TiO_2 in the amorphous xerogels, reported by these authors (Bakre e Tilve, 2017), reveals the potential for the development of novel visible-sensitive TiO_2 CTCs.

Therefore, a study on the CTC made from malonic acid and TiO_2 nanoparticles, not yet carried out as authors are aware, may result in a novel photocatalyst with photocatalytic potential superior to those reported in the literature, by adjusting the parameters of sol-gel synthesis.

This study aims to (1) synthesize, characterize and (2) to evaluate the photocatalytic potential, under low-power visible light, of a novel nanocrystalline CTC composed from nano-TiO_2 bounded to malonic acid, using chlorophenol and tetracycline as the test molecules. In addition, the potential of ROS generation is evaluated using ROS scavengers for $^{\bullet}O_2^-$ and $OH^{\bullet}$, such as benzoquinone and isopropanol, respectively. Furthermore, this study intends to generalize the sol-gel synthesis and calcination conditions for the preparation of TiO_2-bidentate CTC, sensitive to the visible spectrum, and with specific surface areas larger than 250.0 $m^2.g^{-1}$.

5.2. Materials and methods

5.2.1. Materials

The synthesis of the TiO_2-bidentate CTC was carried out using the following reagents: titanium isopropoxide ($Ti(OiP)_4$, purity ~97%), malonic acid, $C_3H_4O_4$ (MoA, purity = 99%) and ethanol (purity ≥ 99.8%). Tetracycline (TC, purity ≥ 98%) and chlorophenol (4-CP, purity ≥ 99%) were used as aqueous pollutant molecules for the photocatalytic tests. Benzoquinone (BQ, purity ≥ 98%) and isopropanol (IPA, purity ≥ 99.5%) were used as ROS scavengers. All reagents were used without further purification and were purchased from Sigma-Aldrich.

5.2.2. Synthesis of TiO_2-Malonic acid charge transfer complex

The synthesis of CTC based on anatase nanocrystalline TiO_2 coupled with malonic acid was carried out by two different sol-gel synthesis methodologies, keeping fixed, in both methods, the molar ratio of complexing A=[MoA]/[Ti] at 2. This ratio was chosen based on the studies reported by Habran et al. (Habran, Pontón, *et al.*, 2018) and Almeida et al. (Almeida *et al.*, 2020), where the authors reported TiO_2-ACAC xerogels (in anatase form) with a mean crystallite size as small as 2.5 nm.

In the first sol-gel methodology, 5.146 g of MoA (0.05 M) were gradually added to 25 mL of ethanol under magnetic stirring. After the complete dissolution of the acid, 45 mL of distilled H_2O was added to the colorless solution, resulting in

a solution with pH= 1.2. Subsequently, 7.5 mL of $Ti(OiP)_4$ (0.025 M) were added to the previous solution, and immediately the colorless solution became a white solution, indicating the beginning of the hydrolysis and condensation process, as well as the formation of sol of TiO_2. The TiO_2 sol was kept for 8 h under vigorous stirring at 60°C. Afterwards, the sol was dried at room temperature overnight obtaining a white TiO_2 gel. Finally, the TiO_2 gel was kept at 100 °C in the oven for ~24 h to obtain the light yellow TiO_2-MoA xerogel, denoted CTC TiO_2-MoA1.

In the second sol-gel methodology, 7.5 mL of $Ti(OiP)_4$ (0.025 mol) were added into 25 mL of ethanol under magnetic stirring. Afterwards, 5.146 g of MoA (0.05 mol) were gradually added to the previous solution and heated to 60°C in order to increase the interaction of malonic acid with $Ti(OiP)_4$. During the dissolution of the MoA, the colorless solution became a strong yellow solution with pH= 1.2. After 10 min, 45 mL of distilled H_2O were added to increase the hydrolysis rate. The result solution, white and slightly viscous, was left at 60°C under stirring for 8 h. After this period, the white TiO_2 sol was deposited in Petri dishes and dried at room temperature overnight. Finally, the TiO_2 gel was dried at 100 °C for ~ 24 h, obtaining a light yellow TiO_2-MoA xerogel, named CTC TiO_2-MoA2.

Both TiO_2-MoA1 and TiO_2-MoA2 CTCs were grounded in an agate mortar and a fraction of the powders were calcined at 270 °C in air for 2 h. The powders obtained showed a brown color and were named as TiO_2-MoA1-270 and TiO_2-MoA2-270.

5.2.3. Characterization techniques

The previously prepared charge transfer complexes, TiO_2-MoA1, TiO_2-MoA1-270, TiO_2-MoA2 and TiO_2-MoA2-270 were thoroughly characterized.

X-ray powder diffraction (XRPD) was carried out in a Bruker D8 Advanced diffractometer (Bruker, Billerica, MA, USA), operating with Cu Kα radiation. The XRPD patterns were measured between 20° to 80° (2θ), with a step size of 0.02° and 2 s per step under 1.6 kW. All diffractograms were analyzed by Le Bail method, through Topas 4.2 software (Bruker, Billerica, MA, USA).

The thermogravimetric (TGA) analysis was performed using a Perkin-Elmer Simultaneous Thermal Analyzer, STA 6000 (Perkin-Elmer, Waltham, MA, USA), under synthetic air flow (20 $mL.min^{-1}$), at a heating rate of 10 $°C.min^{-1}$ in the temperature range of 30–800 °C.

A mass spectrometer (MS) OmniStar/ThermoStar-GSD 320 O3 (Pfeiffer Vacuum) was coupled to the STA-6000 to identify the volatilized species and confirm the presence of malonic acid in the TiO_2-MoA xerogels. The TGA-MS analysis was carried out using a synthetic air flow of 130 mL.min^{-1} and a heating rate of 10 °C.min^{-1}, within the temperature range of 30 °C to 450 °C with a mass of ~ 25 mg per sample. The m/z range until 105 was scanned with the measuring time of 0.5 s.amu^{-1}.

The Fourier transform infrared spectroscopy (FTIR) was performed on a Perkin-Elmer SpectrumTwo FT-IR-ATR spectrometer (Perkin-Elmer, Waltham, MA, USA). Each sample was analyzed without any pre-treatment and investigated in the range from 400 to 4000 cm^{-1}, with a resolution of 4 cm^{-1} and 20 scans.

The textural proprieties were determined by N_2 adsorption-desorption at -196 °C using a NOVAtouch LX2 (Quantachrome, Boyton Beach, FL, USA). Samples were pre-treated at 120 °C under vacuum, for 1 h. The N_2 adsorption isotherms were used to calculate the specific surface area by Brunauer-Emmett-Teller (BET) approach. The correlation coefficients were higher than 0.999 for all BET analyses. Mesoporous volume (V_{meso}) was determined by Barrett-Joyner-Halenda (BJH) method from the desorption branch of isotherm, assuming cylindrical pore model.

The diffuse reflectance spectroscopy (DRS) analyses were carried out using a Perkin-Elmer Lambda650 UV/Vis spectrophotometer (Perkin-Elmer, Waltham, MA, USA) in duplicate, applying *Spectralon* diffuse reflectance white plate standard (Perkin-Elmer, 1.25 in) as blank reference. The bandgap energies were determined through the Kubelka-Mulk function using the DRS data as input and considering the indirect allowed transition.

The photoluminescence emission spectroscopy (PL) at room temperature was performed by Spectroflurometer Photon Technology International, model Quanta Master 40 (American Laboratory Trading, East Lyme, CT, USA), under Xenon lamp excitation at 360 nm.

X-ray photoelectron spectroscopy (XPS) was recorded on a SPECS system equipped with a PHOIBOS 150 EP hemispherical energy analyser, a MCD-9 detector and an XR-50 X-ray source operating at 150 W. The C 1s signal at 284.8 eV was used to calibrate the binding energies (BE).

The electron paramagnetic resonance (EPR) spectra were carried on a Bruker Elexsys model (E500) spectrometer operating at X-band (9.85 GHz) with a high-

sensitivity resonant cavity. The operating parameters were a DC magnetic field ranging from 325 to 360 mT, an AC magnetic field with a frequency of 100 kHz, modulation amplitude of 0.2 mT, microwave power of 0.5 mW and 5 scans of 60 s. A MgO:Cr^{3+} standard sample with g = 1.9797 was used to calibrate the Landé g-factor. The experiments were performed at room temperature and 4 mm quartz tubes were used, suitable for insertion into the resonant cavity.

5.2.4. Measurement of the photodegradation of chlorophenol and tetracycline under reduced power visible light

The photocatalytic activity of the TiO_2-MoA CTCs was evaluated for 4-CP (5 $mg.L^{-1}$) and TC (5 $mg.L^{-1}$) abatement using the liquid photodegradation system previously reported elsewhere (Almeida *et al.*, 2022).

In this study, the measurement protocol was the same one applied by Almeida et al (Almeida *et al.*, 2022). The light source used was a DULUX D/E 26 W residential fluorescent lamp with an irradiance of 0.23 W cm^{-2} and an emission of light in the wavelength range from 400 nm to 700 nm. However, the photocatalyst concentration was reduced from 0.2 $g.L^{-1}$ to 0.1 $g.L^{-1}$ due to higher photocatalytic potential of the new CTCs (*vide infra* § 5.3.8). Furthermore, the absorption at the wavelengths at 224 nm and 358 nm was accompanied for photodegradation of 4-CP and TC during the test time, respectively. The observed reduction in these wavelengths for each pollutant was used as input to determine the percentage of photodegradation performed by TiO_2-MoA CTCs, as seen in Table 3 (Appendix B). The degradation data obtained were presented through the mean value together with the respective standard deviations (Table 3, Appendix B) since all photocatalytic tests were performed in duplicate.

The ROS generation potential of TiO_2-MoA CTCs was evaluated by adding scavenger molecules before starting the photocatalytic tests. The benzoquinone (BQ) scavenger (5.4 $mg \cdot L^{-1}$; 0.05 $mmol \cdot L^{-1}$) was used to inhibit the participation of the $^{\bullet}O_2^-$ radical in the degradation process. In addition, the isopropanol (IPA) scavenger (6.0 $mg \cdot L^{-1}$; 0.1 $mmol \cdot L^{-1}$) was added to inhibit the participation of the $^{\bullet}OH$ radical in the degradation of the tested molecules.

5.3
Results

5.3.1. Analysis of crystalline phases by XRPD

The XRPD patterns of the TiO_2-Malonic acid CTCs are shown in Figure 15. The XRPD patterns of TiO_2-MoA1 (Figure 15a) and TiO_2-MoA2 (Figure 15b) xerogels revealed monophasic material composed of pure anatase (PDF 89-4921). Scolan and Sanchez (Scolan e Sanchez, 1998) reported that a complexation ratio [Acetyacetone]/[Ti] higher than 2 leads to the formation of amorphous TiO_2 xerogels due to reduced reactivity of the hydrolysis-condensation reactions of titanium *n*-butoxide. Therefore, in this study, a complexation ratio equal to 2 for both syntheses can explain the formation of nanocrystalline anatase xerogels.

The samples calcined at 270 °C, TiO_2-MoA1-270 (Figure 15c) and TiO_2-MoA2-270 (Figure 15d), showed diffraction patterns attributed to the pure anatase phase (PDF 89-4921). The low-intensity and broad diffraction lines of TiO_2-MoA CTCs patterns can be associated with a very small size of the TiO_2 crystallites, as reported by Liu et al. (Liu *et al.*, 2017) and Habran et al. (Habran, Pontón, *et al.*, 2018) for the TiO_2-Acetic acid and TiO_2-Acetyacetone CTCs calcined up to 300 °C, respectively.

The samples TiO_2-MoA1, TiO_2-MoA2, TiO_2-MoA1-270 and TiO_2-MoA2-270 presented average crystallite sizes of 4.3 nm, 4.7 nm, 5.0 nm and 4.8 nm, respectively, as calculated through Le Bail method.

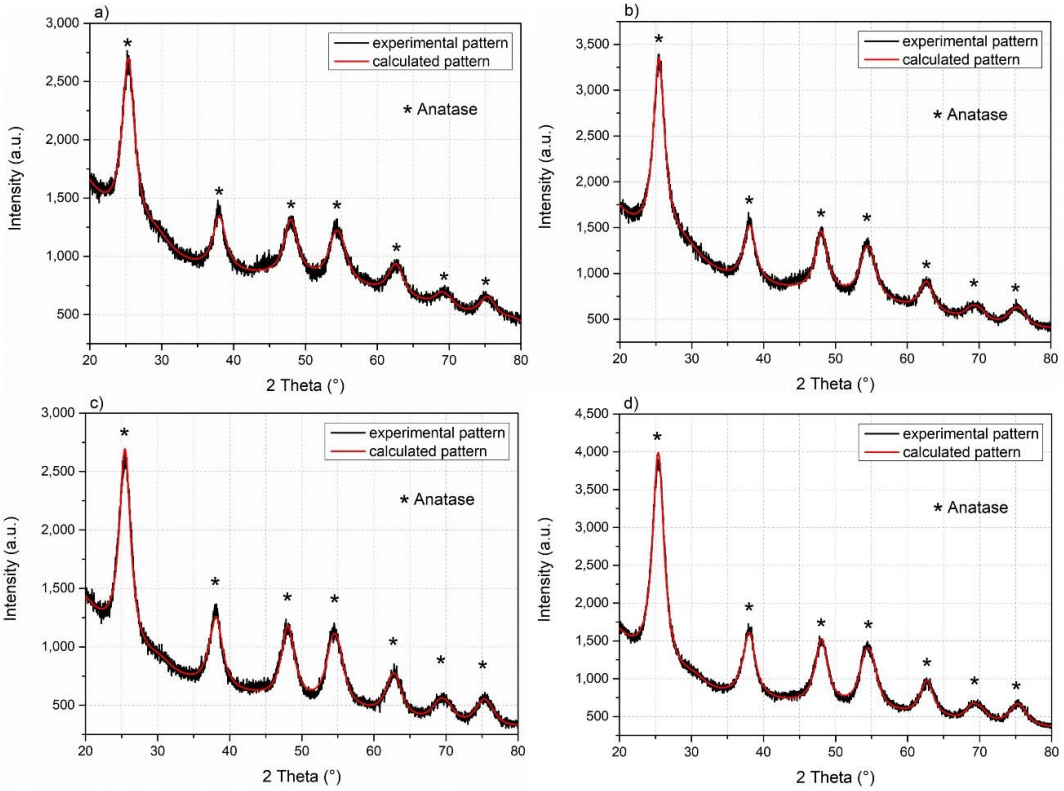

Figure 16: XRPD patterns of a) TiO_2-MoA1, b) TiO_2-MoA2, c) TiO_2-MoA1-270 and d) TiO_2-MoA2-270.

5.3.2. TG analysis of mass loss of TiO_2-Malonic acid CTCs

The thermogravimetric curves and their first derivatives (DTG) of the as-prepared TiO_2-MoA CTCs are shown in Figure 17.

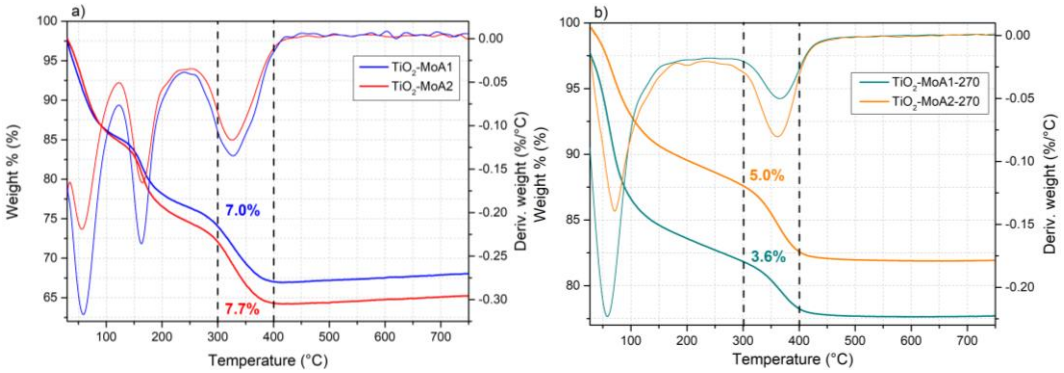

Figure 17: TGA and DTG curves of a) TiO_2-MoA xerogels and b) calcined TiO_2-MoA1-270 and TiO_2-MoA2-270. Vertical dashed lines and the percentages denoted the extension of mass loss due to MoA strongly bounded to TiO_2 and its temperature span.

The TiO_2-MoA1 and TiO_2-MoA2 xerogels (Figure 17a) presented three different mass loss events up to 400 °C. The first mechanism of mass loss, between

room temperature and 150 °C, occurs due to water loss, and is as high as 15.1% for TiO_2-MoA1 and 15.6% for TiO_2-MoA2. In the second step (Figure 17a), from 150 °C to 300 °C, TiO_2-MoA1 and TiO_2-MoA2 lost 11% and 9.6% of the mass, respectively, due to the loss of free or weakly bounded malonic acid to TiO_2, confirmed furthermore by TG-MS and FTIR analysis (*vide infra* § 5.3.3 *and* § 5.3.4). In addition, Caires et al. (Caires *et al.*, 2010) and Thongtem and Thongtem (Thongtem e Thongtem, 2005) reported that the mass loss of pure malonic acid is situated between 150 °C and 250°C, corroborating our interpretation of the mass loss between 150 and 300 °C. On the other hand, in the third event between 300 °C and 400 °C, is associated with the loss of the strongly bonded malonic acid to the TiO_2 surface (*vide infra* § 5.3.3 and § 5.3.4).

The TG and DTG curves of the samples TiO_2-MoA1-270 and TiO_2-MoA2-270 (Figure 17b) revealed that the calcination of the xerogels at 270 °C eliminated, at least partially, malonic acid weekly bounded to anatase surface, *i.e.* only 3% and 2.8% mass loss between 150 and 300 °C have been identified, respectively. Therefore, there are only two significant regions of mass loss in calcined samples. The first mass loss, between room temperature and 150 °C refers to water and the second, between 300 °C and 400 °C, is associated with the MoA strongly bonded to Ti^{4+}. Almeida et al. (Almeida *et al.*, 2020) and Gil-Londoño et al. (Gil-Londoño, Krambrock, *et al.*, 2023) reported for nanocrystalline TiO_2-Acetylacetone CTC that the mass loss above 300 °C was related to the breakage of strong interaction between ACAC (bidentate ligand) and TiO_2. Another recent study, reported by Gil-Londoño et al. (Gil-Londoño, Cremona, *et al.*, 2023) on a novel TiO_2-glutaric acid CTC also pointed out the mass loss of a dicarboxylic acid at temperatures higher than 270 °C, corroborating a strong interaction between TiO_2 and malonic acid.

5.3.3.TiO_2-malonic acid interactions evaluated by TGA-MS

The profiles of evolved gases as a function of temperature for TiO_2-MoA xerogels and calcined TiO_2-MoA CTCs are presented in Figure 18. The release of MoA fragments, water and CO_2 above 150 °C indicates the presence of malonic acid and its interactions with nano-TiO_2 within TiO_2-MoA CTCs.

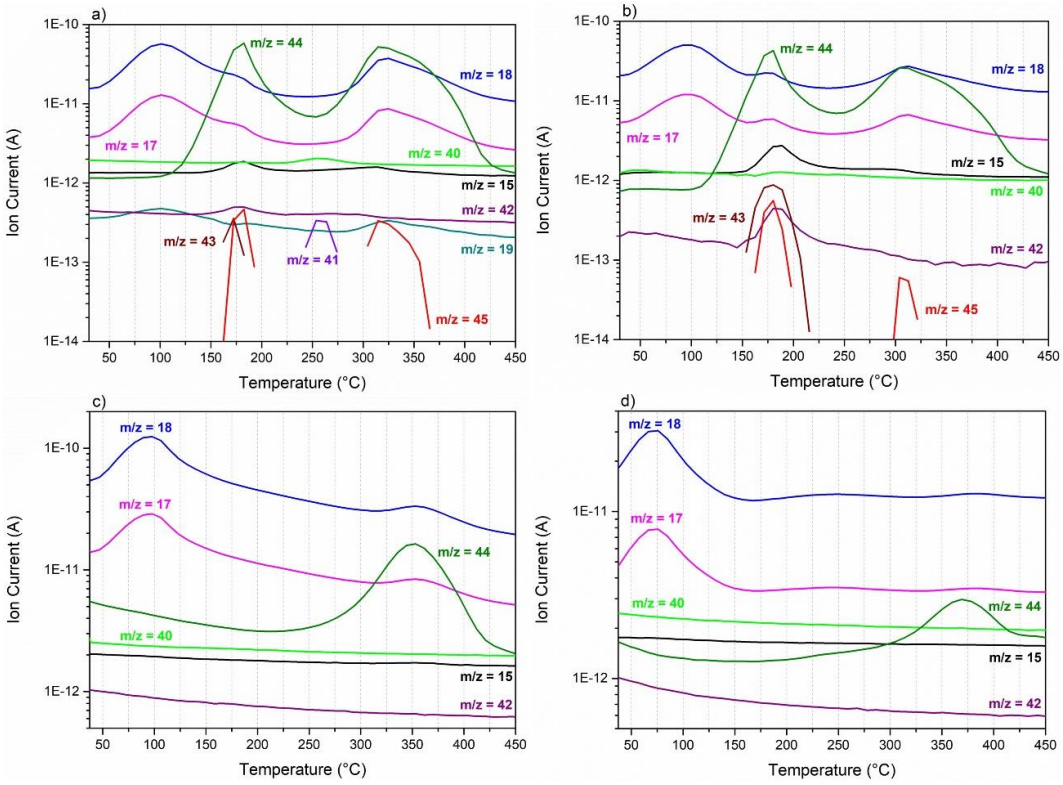

Figure 18: Evolution profiles of gaseous species as monitored by TGA-MS for (a) TiO_2-MoA1, (b) TiO_2-MoA2, (c) TiO_2-MoA1-270 and (d) TiO_2-MoA2-270.

The as-prepared TiO_2-MoA xerogels present three expressive temperature ranges of volatile species release. In the first interval, between 30 °C and 150 °C, the species with m/z= 17 and 18 predominated, corresponding to water release, as reported in other hybrid materials such as TiO_2-ACAC CTC (Almeida *et al.*, 2022), Ni and Cu complexes with imidazole-4,5-dicarboxylic acid (Materazzi, Foti e Crea, 2013), and sodium salt of the maleic acid-acrylic acid copolymer (Grabowska *et al.*, 2011).

In the second temperature region, between 150 °C and 270 °C, both samples (TiO_2-MoA1 and TiO_2-MoA2) show several m/z signals such as those at 15, 42, 43, 44, and 45, beyond the signals of water release (m/z= 17 and 18). The signals at 15, 42, 43, and 45 were associated with methyl (CH_3^+), alkyl ($C_3H_5^+$), acetyl ($CH_3C{\equiv}O^+$) and carboxylic ($COOH^+$) ions, respectively, proving the presence of malonic acid fragments (Dallinga, Nibbering e Boerboom, 1984; Kossanyi e Mogto, 1970; Pagacz *et al.*, 2015). Probably, the malonic acid fragmentation and oxidation (Dallinga, Nibbering e Boerboom, 1984) during the increase in temperature prevents the observation of m/z = 104 of the entire MoA molecule. Furthermore, m/z signals at 44 and 45 may also be associated with CO_2, related to

the oxidation of malonic acid (Almeida *et al.*, 2022; Dallinga, Nibbering e Boerboom, 1984; Materazzi, Foti e Crea, 2013). Therefore, in this temperature region, a release of fragments of the weakly bounded malonic acid molecules, and as well as the release of water and CO_2 due to malonic acid oxidation occurred simultaneously.

In the third region (from ~ 270 °C to 400 °C) only release of m/z = 15 and 45 was observed due to MoA fragments methyl (CH_3^+), and carboxylic ($COOH^+$), respectively, beyond the signals of water and CO_2, situated at m/z = 17, 18, 44 and 45. The increased release of water and CO_2 and lower release of malonic acid fragments are probably associated with the effective MoA oxidation process at temperatures higher than 270 °C.

Furthermore, TiO_2-MoA1 sample presents an additional range, although low intense, of evolved gases, between ~230 °C and 270 °C. The signals at m/z = 41 and m/z = 42, corresponding to alkyl ion ($C_3H_5^+$). This fourth release interval is also associated with a weaker interaction of malonic acid with anatase. The TiO_2-MoA2 did not present this additional release.

As expected, TGA-MS analysis of TiO_2-MoA-270 CTCs confirmed the release of organic content only above 270 °C. Figure 18c and 18d revealed an increase of CO_2 (m/z= 44) and water (m/z= 17 and 18) release, between 270 and 400 °C, for TiO_2-MoA1-270 and MoA2-270 CTCs, respectively. This species released are associated with the MoA oxidation process. In addition, in the temperature range of 30 °C to 150 °C it was possible to observe the release of water.

5.3.4. FTIR analysis of TiO_2-MoA CTCs bidentate bonds

Figure 19 shows the FTIR spectra of pure malonic acid, TiO_2-MoA xerogels, and calcined TiO_2-MoA CTCs. The FTIR analysis contributed to identifying the presence and the binding forms of carboxylic functional groups from MoA with metallic oxides, such as TiO_2 (Bakre e Tilve, 2017; Qu *et al.*, 2010; Zhao *et al.*, 2008).

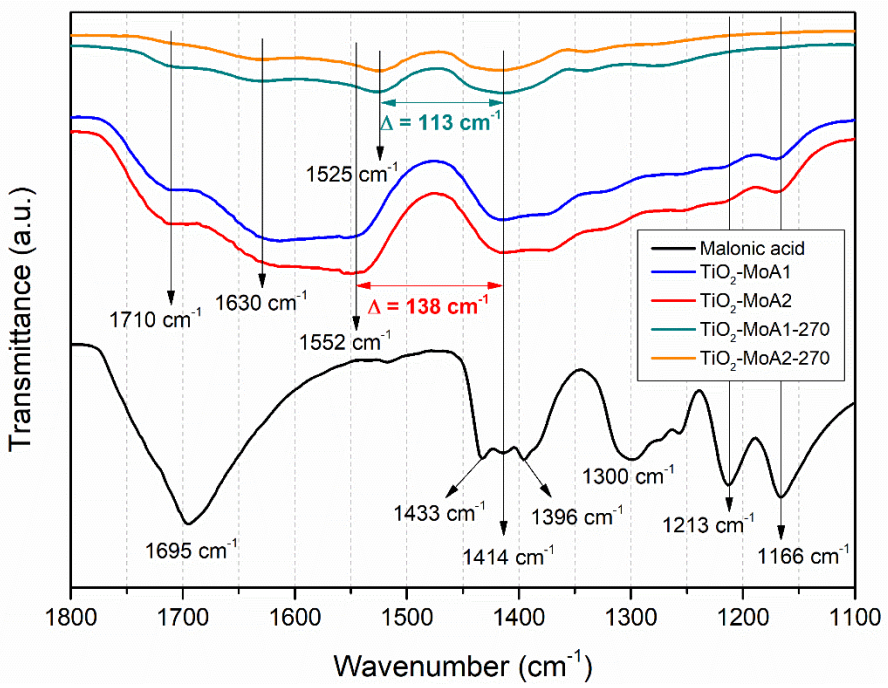

Figure 19: Fourier-transform infrared (FTIR) spectra of malonic acid, TiO_2-MoA1, TiO_2-MoA2, TiO_2-MoA1-270 and TiO_2-MoA2-270.

The FTIR spectra of TiO_2-MoA1 and TiO_2-MoA2 xerogels preserved some vibrations modes associated to the pure MoA molecule due to the content of weakly bound MoA. The bands situated at 1166 cm^{-1}, 1213 cm^{-1} and 1300 cm^{-1} are assigned to $\tau(CH_2)$, ν(C–C) and ν(C–O), respectively (Ganguly *et al.*, 1980; Shao *et al.*, 2017). These three vibrations modes of MoA were preserved in the xerogels samples. On the other hand, the C=O stretching band observed for the pure MoA at 1695 cm^{-1} was shifted to 1710 cm^{-1} and reduced in intensity in xerogel samples since malonic acid is linked to TiO_2 and, possibly, with water (> 10% mass loss in all as prepared TiO_2-MoA CTC samples) *vide infra* § 5.3.2. The humidity can alter the keto-enol equilibrium in the MoA, shifting the ν(C=O) toward the enol form as humidity increases (Ghorai, Laskin e Tivanski, 2011; Shao *et al.*, 2017). Furthermore, the covalent bonds between TiO_2 and MoA formed during the sol-gel synthesis also contributed to the decrease of free COOH groups and the increase of enol form of MoA in the CTCs. The presence of enol form was confirmed by the appearance of C=C stretching band at 1630 cm^{-1}. The ν(C=C) is assigned in the range of 1620 cm^{-1} to 1680 cm^{-1}, characteristic of the keto-enol tautomerism reaction (Ghorai, Laskin e Tivanski, 2011).

However, the formation of complexes (chemical adsorption) between organic molecules and metal oxides is confirmed by the presence of asymmetric and

symmetric stretching of the carboxylate group, ν(COO) bounded to metal ions (Gil-Londoño, Cremona, *et al.*, 2023; Qu *et al.*, 2010; Thongtem e Thongtem, 2005; Zhao *et al.*, 2008). Both TiO_2-MoA xerogels have asymmetric ν(COO) at 1552 cm^{-1} and the symmetric ν(COO) at 1414 cm^{-1}, confirming covalent bond formation between MoA molecule and Ti^{4+}. In addition, Almeida et al. (Almeida *et al.*, 2020) and Liu et al. (Liu *et al.*, 2017) reported asymmetric and symmetric ν(COO) for the xerogels formed between TiO_2-Acetylacetone and TiO_2-Acetic acid, respectively.

Furthermore, the wavenumber separation between the asymmetric (ν_{as}) and symmetric stretching (ν_s) COO vibration bands ($\Delta = \nu_{as-} \nu_s$) can reveal the binding mode. Bidentate bridging presents Δ = 150-180 cm^{-1} while bidentate chelating presents Δ = 60-100 cm^{-1} (Qu *et al.*, 2010; Zhao *et al.*, 2008). TiO_2-MoA xerogels present Δ = 138 cm^{-1}, a wavenumber separation between bidentate bridging and bidentate chelating, suggesting a combination of both bidentate binding modes. Qu et al. (Qu *et al.*, 2010) observed for the complex formed between TiO_2 and *p*-bromobenzoic acid (dicarboxylic acid) Δ = 130 cm^{-1} and the authors also suggested a bidentate bridging/chelating form.

On the other hand, TiO_2-MoA-270 CTCs spectra (Figure 19) revealed only a bidentate chelating mode. The calcined samples have ν_{as}(COO) at 1525 cm^{-1} and ν_s(COO) at 1414 cm^{-1}, resulting in Δ = 114 cm^{-1}. Gil-Londoño et al. (Gil-Londoño, Cremona, *et al.*, 2023) and Almeida et al. (Almeida *et al.*, 2020) also reported Δ = 114 cm^{-1} for the calcined TiO_2-GA-270 and TiO_2-ACAC-300 CTCs, respectively, corroborating the formation of bidentate chelating. The calcination eliminated the MoA weekly bonded to TiO_2. Qu et al. (Qu *et al.*, 2010) concluded that thermal treatment at 250 °C of TiO_2 modified by *p*-bromobenzoic acid, *via* solvothermal reaction, eliminates the simply absorbed (weakly bounded) *p*-bromobenzoic acid molecules on TiO_2 surface and preserves the bidentate chelating form (Δ = 96 cm^{-1}). Furthermore, the FTIR spectra of TiO_2-MoA-270 CTCs show a reduced organic vibrations mode. However, a low vibration intensity of C=O (1710 cm^{-1}) and C=C (1630 cm^{-1}) stretching modes were observed.

Therefore, TiO_2 and MoA are bonded through two oxygen atoms of malonic acid with one Ti ion, in all TiO_2-MoA CTCs. The bidentate bonds can be formed by two different combinations of functional group (hydroxyl and/or carbonyl) in our nanocrystalline TiO_2-MoA CTCs. Bakre and Tilve (Bakre e Tilve, 2017), and Thomas et al. (Thomas e Syres, 2012) reported different ways of bidentate chelating

mode, supporting the binding modes proposed for the MoA carboxylic groups with TiO_2 in our study (Figure 20).

The first bidentate binding mode occurs through one oxygen of hydroxyl group and one oxygen of carbonyl group with one Ti^{4+}, forming a bidentate chelating (Figure 20a). The presence of ν(C=O) band at 1710 cm^{-1} (Figure 19a) associated with the side of the carboxyl group not connected with TiO_2 surface corroborates this bidentate bond configuration. Besides our results, Gil-Londoño et al. (Gil-Londoño, Cremona, *et al.*, 2023) also reported bidentate chelating form (Δ = 114 cm^{-1}) and ν(C=O) at 1697 cm^{-1} for the TiO_2-Glutaric acid xerogel and calcined sample.

The second bidentate binding mode is formed by the bonds between the oxygen atoms of the two carbonyl groups with Ti^{4+} (Figure 20b). This second bidentate bond configuration is characterized by the formation of a bidentate ring between the Ti^{4+} and the enol form of MoA, named as 6-member ring bidentate chelating (Figure 20b). Furthermore, the asymmetric and symmetric vibrations of carboxylate group is accompanied by the appearance of C=C vibration band (located at 1630 cm^{-1}) in our TiO_2-MoA CTCs (Figure 19), corroborating the 6-member ring bidentate chelating mode. In some previous studies reported by our research group, TiO_2-ACAC CTCs revealed the same 6-member ring bidentate chelating mode (Almeida *et al.*, 2020; Gil-Londoño, Krambrock, *et al.*, 2023). However, acetylacetone is a β-diketone, not present hydroxyl group, and can only form bidentate bonds with TiO_2 through both carbonyl functional groups in the ketonic and enolic forms (Almeida *et al.*, 2020). Furthermore, Fahmi et al. (Fahmi *et al.*, 1995) reported that the carbonyl group gives the highest adsorption energy between TiO_2 and oxalic acid (dicarboxylic acid). Therefore, the second bidentate bond configuration (Figure 20b) is possibly the most significant one in the novel TiO_2-MoA CTC, being one of the explanations for the high photocatalytic performance of this CTC (*vide infra* § 5.3.8).

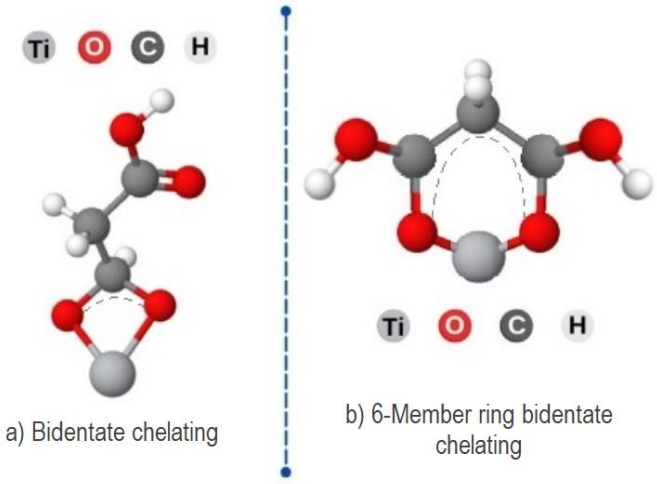

Figure 20: Two possible bidentate binding modes between carboxylic groups from malonic acid and TiO_2.

5.3.5. Textural properties of TiO_2-MoA CTCs

The N_2 adsorption-desorption curves of the two TiO_2-MoA CTCs presented similar features (Figure 34, Appendix B). Both isotherms of TiO_2-MoA xerogels can be classified as Type IVa with hysteresis loop H2b, in accordance with IUPAC classification, typical for materials with irregular pore sizes and shapes, such as inorganic gels and oxides (Sangwichien e Aranovich, 2002; Thommes *et al.*, 2015). TiO_2-MoA1 and TiO_2-MoA2 have high surface area of 180.9 $m^2.g^{-1}$ and 243.5 $m^2.g^{-1}$, respectively (Table 1).

After the calcination of xerogels samples at 270 °C in air, the surface areas and mesoporous volumes were significantly increased (Table 1). The calcination process, eliminates the excess of organic content (*vide infra* § 5.3.3) in TiO_2-MoA pores, increasing approximately twice the mesoporous volume (Table 1). The same behavior was observed by Almeida et al. (Almeida *et al.*, 2020) and Liu et al. (Liu *et al.*, 2017) after the calcination at 300 °C of TiO_2-ACAC and TiO_2-AA xerogels, respectively. Both TiO_2-MoA-270 CTCs present Type IVa isotherms with hysteresis loop H2b, characteristic of mesoporous materials that used to have a high surface area (Sangwichien e Aranovich, 2002; Thommes *et al.*, 2015). Consequently, surface area of TiO_2-MoA1-270 and TiO_2-MoA2-270 increased 69% and 33% to 306.1 $m^2.g^{-1}$ and 323.9 $m^2.g^{-1}$, respectively, in comparison to their respective xerogels. The increase in surface area provides more reactive sites for absorption and photodegradation of pollutants (Wu, Lin e Hu, 2021).

To the best of our knowledge, these novel TiO_2-MoA-270 CTCs have the highest surface area among the nanoparticles functionalized by small organic molecules.

Table 1: Specific surface areas (S_{BET}), volumes of mesopores (V_{meso}), optical bandgaps and intrinsic bandgaps

Sample	S_{BET}	V_{meso} (BJH)	Optical bandgap	Intrinsic bandgap
	$m^2\ g^{-1}$	$mL\ g^{-1}$	eV	eV
TiO_2-MoA1	180.9	0.130	2.27	3.15
TiO_2-MoA2	243.5	0.202	2.33	3.14
TiO_2-MoA1-270	306.1	0.339	1.75	2.92
TiO_2-MoA2-270	323.9	0.356	1.78	2.96

5.3.6. Optical properties of TiO_2-MoA CTCs

Figure 21 shows the DRS spectra and Kubelka-Munk plots of TiO_2-MoA1, TiO_2-MoA2, TiO_2-MoA1-270, and TiO_2-MoA2-270. The optical and intrinsic bandgaps of the as-prepared TiO_2-MoA CTCs are present in Table 1. TiO_2-MoA xerogels present a pale-yellow color. The shift of absorption into the visible light region (Figure 6a, extended from 387 nm to ~ 600 nm) is a consequence of the LMCT mechanism, in which the electrons from the HOMO of malonic acid are transferred to the CB of anatase. The Kubelka-Munk plots of TiO_2-MoA1 and TiO_2-MoA2 (Figure 6b) reveal an optical bandgap of 2.27 eV and 2.33 eV, respectively. The optical bandgap of ~ 2.3 eV is a feature of the LMCT mechanism in charge transfer complexes between TiO_2 and chelating ligands (Zhang, Kim e Choi, 2014), as observed in other studies such as for TiO_2-squaric acid (Barbieriková *et al.*, 2022), TiO_2-Acetylacetone (Almeida *et al.*, 2020; Gil-Londoño, Krambrock, *et al.*, 2023; Sannino *et al.*, 2015), TiO_2-salicylic acid (Božanić *et al.*, 2019). Furthermore, the TiO_2-MoA xerogels reveal a bandgap of 3.15 eV and 3.14 eV, respectively, associated with the anatase phase (bandgap equal to 3.2 eV (Gil-Londoño, Cremona, *et al.*, 2023; Pessanha *et al.*, 2023; Ren *et al.*, 2017)), *vide infra* § 5.3.1.

On the other hand, the calcined samples, TiO_2-MoA1-270 and TiO_2-MoA2-270, absorb the entire visible spectrum (Figure 21), showing a brown color. The

increase of visible sensitization can be associated with the combination of the LMCT mechanism and the formation of extrinsic oxygen vacancies produced through the partial oxidation of malonic acid molecules bonded to the TiO_2 surface, during the calcination process (*vide infra* § 5.3.3). Furthermore, the Kubelka-Munk plots of TiO_2-MoA1-270 and TiO_2-MoA2-270 show a reduction of the bandgaps associated to the anatase phase and LMCT mechanism, corroborating the creation of intermediated energy levels within the TiO_2 bandgap, probably, due to extrinsic oxygen vacancies (*vide infra* § 5.3.7). The intrinsic anatase bandgaps were reduced to 2.92 eV for TiO_2-MoA1-270 and 2.96 eV for TiO_2-MoA2-270. In addition, the optical bandgaps were reduced to 1.75 eV for TiO_2-MoA1-270 and 1.78 eV for TiO_2-MoA2-270.

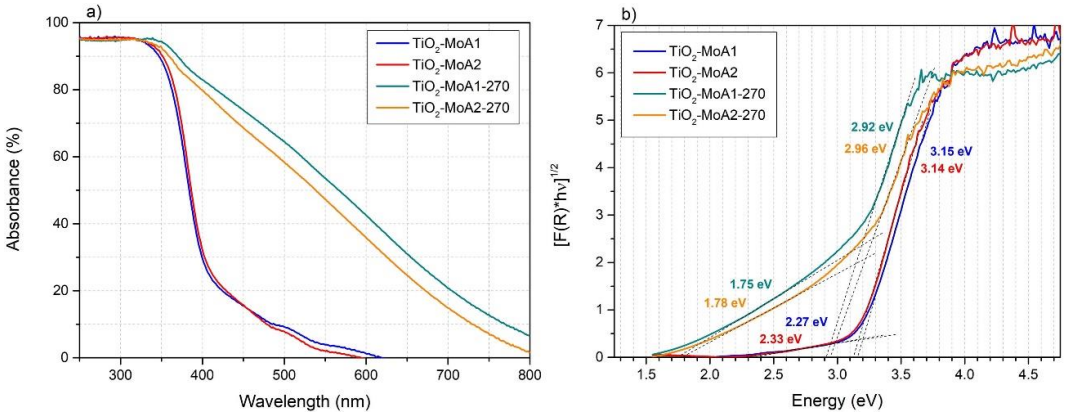

Figure 21: (a) DRS curves and (b) Kubelka-Munk plots of TiO_2-MoA1, TiO_2-MoA2, TiO_2-MoA1-270 and TiO_2-MoA2-270.

The PL spectra of the as-prepared TiO_2-MoA CTCs are shown in Figure 22. These PL spectra can confirm the formation of LMCT mechanisms and energy sublevels within TiO_2 bandgap due to extrinsic oxygen vacancies (Aronne *et al.*, 2017; Gil-Londoño, Cremona, *et al.*, 2023; Gil-Londoño, Krambrock, *et al.*, 2023). The deconvolution of the PL spectra of all samples was performed in the energy range of visible light (1.82 - 3.1 eV). The emission bands associated with excitons located at TiO_6 octahedra (exciton PL), LMCT mechanism, and F^+ center electronic transitions were identified, in accordance to the literature (Aronne *et al.*, 2017; Gil-Londoño, Cremona, *et al.*, 2023; Gil-Londoño, Krambrock, *et al.*, 2023; Lei *et al.*, 2001; Santara *et al.*, 2013; Serpone, 2006).

The PL spectra of TiO_2-MoA xerogels and their deconvolution curves (Figure 22a-b) present two significant emission bands. One emission band centered at 2.85 eV and another one centered at ~2.4 eV were associated with exciton emission and electron decay from CB of anatase to HOMO of malonic acid, respectively. Both TiO_2-MoA xerogels did not present signal of color center F^+, *i.e.*, no evidence on deep trap state due to single electron trapped in oxygen vacancy (SETOV) (equation 5, *vide infra* § 5.3.7). Gil-Londoño et al. (Gil-Londoño, Krambrock, *et al.*, 2023) reported the presence of an emission band associated with the LMCT mechanism and the absence of an emission band associated with the F^+ center in the PL spectra of TiO_2-Acetylacetone xerogel. Therefore, the PL spectra of as-prepared TiO_2-MoA xerogels corroborate the LMCT mechanism as also suggested in the DRS spectra and Kubelka-Munk plots (Figure 21).

However, for the calcined samples, a combined contribution of oxygen vacancies and the LMCT mechanism in the visible sensitization was identified, shifting the maximum emission band to lower energies of the visible spectrum. The calcined TiO_2-MoA CTCs (Figure 22c-d) presented a third emission band, centered at 1.96 eV, related to electron decay from the excited state (F^{+*} centers) to the ground state of F^+ centers. Another recent study on TiO_2-GA xerogels calcined, in air, at 270 °C also identified emission bands associated with F^+ centers (1.96 eV) and LMCT mechanism (2.4 eV) (Gil-Londoño, Cremona, *et al.*, 2023), corroborating the creation of oxygen vacancies during the calcination of TiO_2-MoA xerogels. In addition, the intensity of the emission band assigned to the LMCT mechanism in the calcined TiO_2-MoA CTCs was reduced in respect to the xerogels samples, as also reported by Gil-Londoño et al. (Gil-Londoño, Krambrock, *et al.*, 2023) for the TiO_2-ACAC xerogel calcined at 270 °C in air. Therefore, the TiO_2-MoA-270 CTCs may present a decay of the excited electron from the CB of TiO_2 to the energy sublevel of SETOV, decreasing the emission band related to the LMCT mechanism.

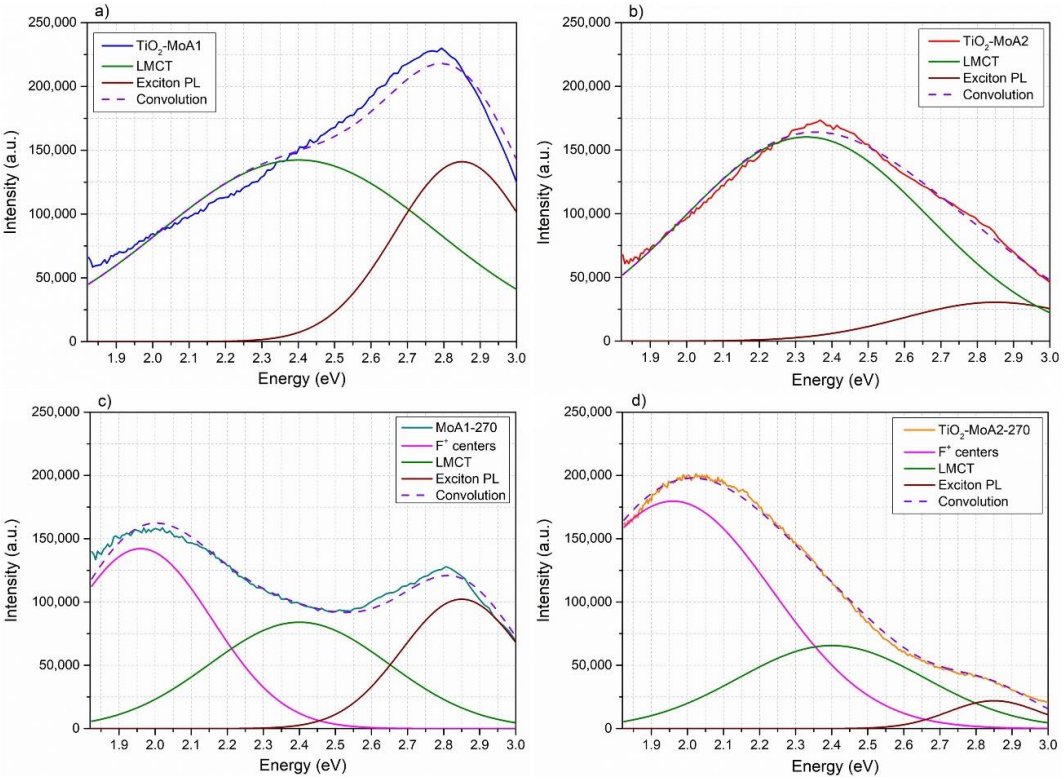

Figure 22: PL emission spectra of a) TiO_2-MoA1, b) TiO_2-MoA2, c) TiO_2-MoA1-270 and d) TiO_2-MoA2-270.

5.3.7. Electron paramagnetic resonance and X-ray photoelectron spectroscopies of TiO_2-MoA CTCs

The EPR measurements at room temperature were performed to analyze the presence of SETOV (color center F^+) and Ti^{3+} in the calcined TiO_2-MoA CTCs samples (Figure 23). None of the as-prepared TiO_2-MoA CTCs present a signal of Ti^{3+} with Landé g factor equal to 1.96 – 1.99 (Gil-Londoño, Krambrock, *et al.*, 2023; Mao *et al.*, 2017). In addition, the TiO_2-MoA xerogels do not present SETOV signal, with g = 2.0043 (Figure 23), while both calcined samples present SETOV signal. The absolute concentration of SETOV in TiO_2-MoA1-270 and TiO_2-MoA2-270 is 1.8×10^{16} cm^{-3} and 1.4×10^{16} cm^{-3}, respectively, obtained from double integration of the EPR spectrum and comparison with $CuSO_4$ standard. Therefore, based on the EPR data an electronic charge compensation mechanism in TiO_2-MoA CTCs after the calcination process can be proposed, *i.e.*, the formation of oxygen vacancies with one electron at the vacancy site (SETOV) is accompanied by the absence of trivalent titanium, leading to the creation of color centers F^+ (equation 6, using the standard Kröger–Vink notation) (Gil-Londoño, Cremona, *et al.*, 2023;

Gil-Londoño, Krambrock, *et al.*, 2023). This electronic charge compensation mechanism was proposed for two calcined TiO_2-bidantate ligand CTCs, such as TiO_2-ACAC-270 (Gil-Londoño, Krambrock, *et al.*, 2023) and TiO_2-GA-270 (Gil-Londoño, Cremona, *et al.*, 2023), considered fundamental for their high photocatalytic activity. In addition, the EPR spectra corroborate the DRS and PL results on extrinsic oxygen vacancies (*vide infra* § 5.3.6).

Equation 5: Definition of SETOV / centers F^+

$$\text{SETOV} = V_O^{\bullet\bullet} + 1e^- = V_O^{\bullet} \equiv F^+$$

Equation 6: Formation of SETOV / centers F^+

$$2O_O^x + Ti_{Ti}^x \xrightarrow{\text{Calcination}} 2V_O^{\bullet} + Ti_{Ti}^x + 2e' + O_2$$

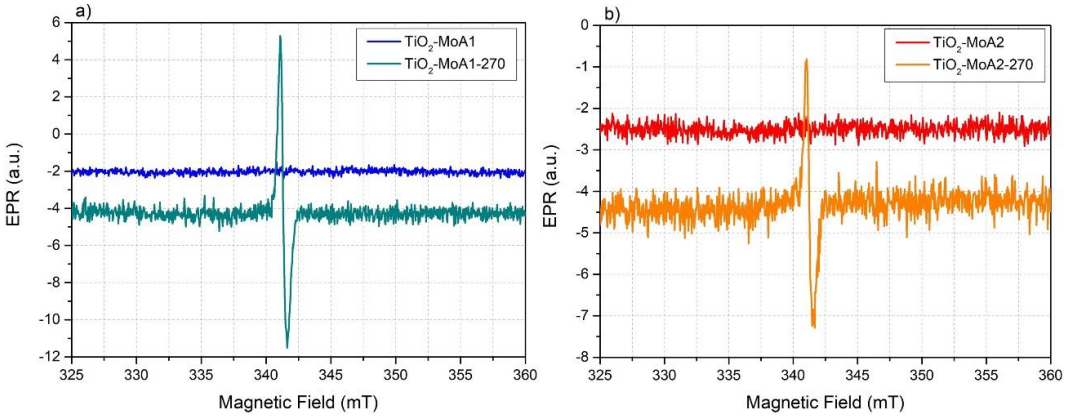

Figure 23: EPR spectra of a) TiO_2-MoA1 and TiO_2-MoA1-270; b) TiO_2-MoA2 and TiO_2-MoA2-270.

The TiO_2-MoA1-270 and TiO_2-MoA2-270 were analyzed by XPS to elucidate the type of Ti species present at the surface in calcined specimens. Figure 24 shows the XPS spectra of TiO_2-MoA1-270 and TiO_2-MoA2-270 CTCs. Both samples exhibit peaks at 458.5 eV and 464.3 eV, which is characteristic of Ti^{4+} $2p_{3/2}$ and Ti^{4+} $2p_{1/2}$, respectively (Ullattil *et al.*, 2018). In addition, the Ti 2p XPS spectra of calcined samples did not present peak asymmetry (Figure 24), which is a characteristic feature when Ti^{3+} is present (Guan *et al.*, 2017). It is relevant to notice that, in a similar manner, Almeida et al. (Almeida *et al.*, 2020), Gil-Londoño et al. (Gil-Londoño, Cremona, *et al.*, 2023) and Liu et al. (Liu *et al.*, 2017) reported three others calcined nanocrystalline CTCs (TiO_2-ACAC-300, TiO_2-ACAC-270, and

TiO_2-AA-300, respectively) free of Ti^{3+}. Therefore, the XPS data support the proposed electronic charge compensation mechanism for the TiO_2-MoA-270 CTCs.

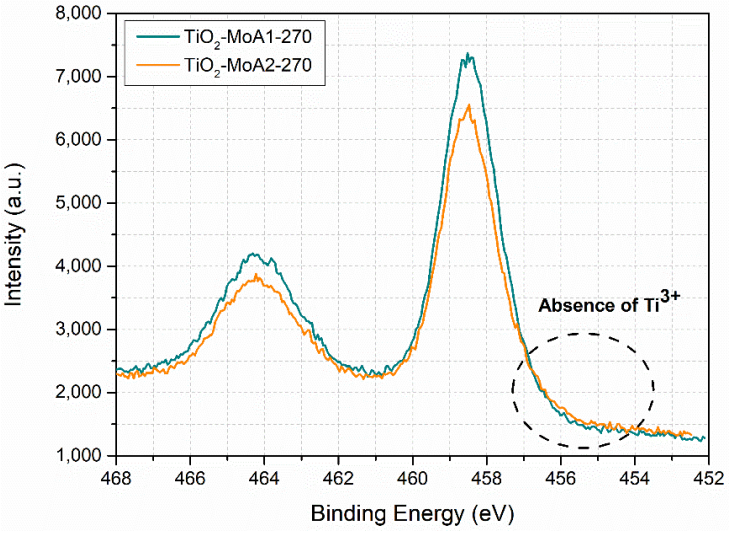

Figure 24: Ti 2p XPS spectra for TiO_2-MoA1-270 and TiO_2-MoA2-270.

5.3.8. Photocatalytic Performance of the TiO_2-MoA CTCs under reduced power visible light

The photocatalytic degradation of tetracycline and chlorophenol are shown in Figure 25a and Figure 25b, respectively, for all TiO_2-MoA CTCs. The photodegradation of TC (antibiotic) and 4-CP (industrial wastewater) are examples of practical applications of TiO_2-MoA CTCs for aqueous decontamination since both molecules are sources of severe pollution of aqueous effluents (Galeas *et al.*, 2023; He, Kai e Ding, 2021; Mohammad *et al.*, 2021; Moraes, de, Torezin, *et al.*, 2020; Zhou *et al.*, 2020).

Figure 25a reveals a photocatalytic degradation of TC higher than 90% after 6 h, using both xerogel or calcined TiO_2-MoA CTCs as photocatalysts. The TiO_2-MoA1 and TiO_2-MoA2 xerogels show a TC photodegradation of 94.8% ± 7.3% and 93.7% ± 8.9%, respectively. The high photocatalytic performance of the TiO_2-MoA xerogels was not expected owing to lower visible light absorption and specific area, as well as owing to excess of MoA weakly bound to TiO_2, in comparison to the calcined CTCs (Figure 21, Table 1 and Figure 17, respectively) and also considering some previous studies (Almeida *et al.*, 2020; Habran, Pontón, *et al.*, 2018). For example, our research group reported a low conversion of NO_x (initial

concentration of 100 ppm) into NO_3^- (~ 20%, during 1 h) for the TiO_2-ACAC xerogel CTC while the calcinated sample (300 °C in air) convert almost 100% of NO_x, within 1 h (Almeida *et al.*, 2020). However, the TiO_2-MoA1 and TiO_2-MoA2 xerogels have a surface area 37% and 85%higher, respectively, than TiO_2-ACAC xerogel (Almeida *et al.*, 2020). In addition, mesopore volume in TiO_2-MoA1 and TiO_2-MoA2 was 86% and 188% higher, respectively, than for TiO_2-ACAC xerogel (Almeida *et al.*, 2020). High surface areas and mesopore volumes of the as-prepared TiO_2-MoA xerogels may explain their efficient photocatalytic degradation of TC.

Furthermore, the TiO_2-MoA1-270 and TiO_2-MoA2-270 calcined samples show the highest TC photodegradation of 97.7% ± 3.3% and 96.7% ± 2.0%, respectively, under reduced power of visible light (26 W). This photocatalytic performance of calcined TiO_2-MoA-270 CTCs was comparable to the best outcome of the heterojunctions between different semiconductors, as reported in the review by He et al. (He, Kai e Ding, 2021). Those authors rejoin more than 70 studies of photocatalytic heterojunctions displaying high photocatalytic activity under high power visible light (> 200 W) and with the concentration at least twice of that used in the present study. Only two heterojunctions, $NiFe_2O_4$ deposited S-doped g-C_3N_4 nanorod (SCNNR) and $Bi_2W_2O_9$/g-C_3N_4 degraded TC, under reduced power visible light (40 W) and sunlight (35 W), respectively, to the level as high as 90% (He, Kai e Ding, 2021). However, the concentration of the photocatalyst $NiFe_2O_4$/SCNNR and $Bi_2W_2O_9$/g-C_3N_4 were 5 times and 10 times, respectively, higher than the used in this study. Recently, two different studies on calcined CTCs, TiO_2-ACAC-270 (Gil-Londoño, Krambrock, *et al.*, 2023) and TiO_2-GA-270 (Gil-Londoño, Cremona, *et al.*, 2023), demonstrated TC photocatalytic abatement of 88.5% and 74.8%, respectively, under the same conditions as the photocatalytic tests carried out in this study. Additionally, TiO_2-ACAC-270 (Gil-Londoño, Krambrock, *et al.*, 2023) and TiO_2-GA-270 (Gil-Londoño, Cremona, *et al.*, 2023) also show the presence oxygen vacancies after the calcination process, as observed in our study. However, the novel calcined TiO_2-MoA CTCs have more than twice the surface area and mesopore volume of calcined TiO_2-ACAC CTC (S_{BET} =137.0 $m^2.g^{-1}$ and V_{meso} = 0.16 $mL.g^{-1}$) (Almeida *et al.*, 2020). [25,26] As such, the highest photocatalytic performance of TiO_2-MoA-270 CTCs for TC degradation is probably associated with the high surface area (≥ 306.1 $m^2.g^{-1}$) and more effective generation of $^{\bullet}O_2^-$ radicals (*vide infra* § 5.3.9). In addition, the synergetic effect of

the LMCT mechanism (being the source of excited electrons) and energy levels of oxygen vacancies within the TiO_2 bandgap (causing reduction of recombination rate of e^-/h^+ pairs) would additionally contribute to such a high level of TC degradation under low power visible light.

A higher photocatalytic performance of TiO_2-MoA CTCs to degrade tetracycline (Figure 25a) than chlorophenol (Figure 25b) can be attributed to the predominant role of $^{\bullet}O_2^-$ radicals in the TC degradation (He, Kai e Ding, 2021) while $OH^{\bullet}$ radical is reported as the main ROS acting in 4-CP degradation (Li, F. *et al.*, 2018; Schneider *et al.*, 2014). Equations 7 and 8 represent the reaction between the e^-/h^+ pairs to form $^{\bullet}O_2^-$ and $OH^{\bullet}$ radicals.

Equation 7: Photogeneration of $^{\bullet}O_2^-$ radicals

$$O_2 + e^- \rightarrow {}^{\bullet}O_2^-$$

Equation 8: Photogeneration of $OH^{\bullet}$ radicals

$$OH^- + h^+ \rightarrow OH^{\bullet}$$

Figure 25b shows photocatalytic performance of the as-prepared TiO_2-MoA CTCs during 6h of 4-CP photodegradation test. TiO_2-MoA xerogels did not show photocatalytic activity against 4-CP (Figure 25b). This performance was comparable to the 4-CP photolysis test (less than 5% degradation during the test time) previously reported by Almeida et al. (Almeida *et al.*, 2022).

On the other hand, the TiO_2-MoA1-270 and TiO_2-MoA2-270 present 25.7% ± 3.6% and 30.8% ± 3.9%, respectively, of photodegradation for 4-CP. Almeida et al. (Almeida *et al.*, 2022) reported 4-CP photodegradation of 31.3% using 0.2 $g.L^{-1}$ TiO_2-ACAC-300, twice the concentration of photocatalyst tested in this study. Moreover, TiO_2-ACAC-300 did not generate $OH^{\bullet}$ efficiently, so its photocatalytic performance in 4-CP degradation was a result of the efficient generation of $^{\bullet}O_2^-$ radicals, as revealed through the addition of ROS scavengers in the photocatalytic tests [15]. Moraes et al. reported photodegradation of 4-CP of nearly 90% under UV-Vis light after 5h using three different photocatalyst (0.2 $g.L^{-1}$), TiO_2/Nb_2O_5/carbon xerogel (Moraes, de, Torezin, *et al.*, 2020), lignin-based carbon xerogel/ZnO (Moraes, de *et al.*, 2023) and ZnO/ZnS/carbon xerogel (Moraes, de *et al.*, 2021). However, the UV-Vis light power was as high as 300 W, ~11 times

higher than applied in our study. In addition, ZnO/ZnS/carbon xerogel shows 4-CP degradation of ~ 45% after 5 h, under visible light (400 W, with UV filter) and revealed a dependence of both hydroxyl and superoxide radicals ($^{\bullet}O_2^-$ and $OH^{\bullet}$) in its 4-CP photodegradation (Moraes, de *et al.*, 2021). Therefore, the photocatalytic performance of the TiO_2-MoA-270 CTCs is relevant for 4-CP partial abatement due to efficient generation of $^{\bullet}O_2^-$ radicals, high surface area and mesopore volume. Furthermore, the photocatalytic activity of TiO_2-MoA1-270 CTC in relation to TiO_2-MoA2-270 CTC was practically the same, probably because the content of strong bonds between TiO_2 and MoA is very close between these CTCs (*vide infra* § 5.3.2 and § 5.3.4), as well as the concentration of SETOVs (*vide infra* § 5.3.7).

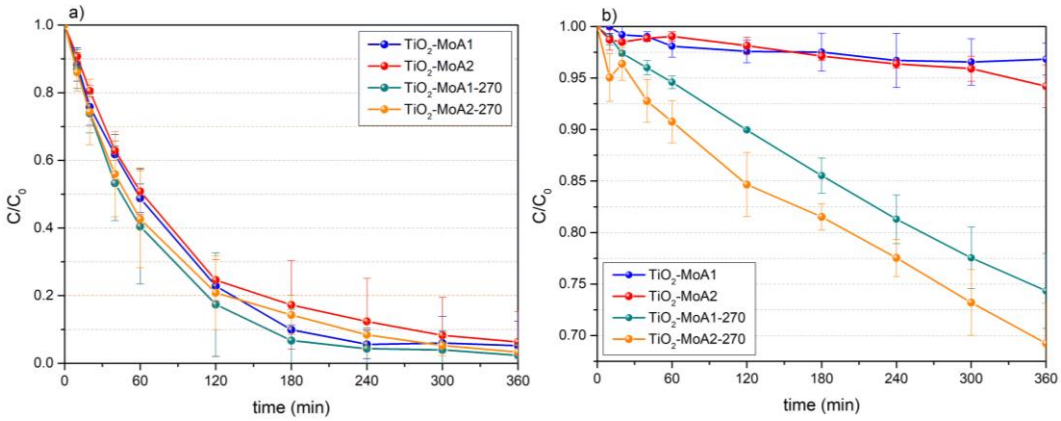

Figure 25: a) Tetracycline and b) chlorophenol photodegradation by TiO_2-MoA1, TiO_2-MoA1-270, TiO_2-MoA2 and TiO_2-MoA2-270.

5.3.9. ROS generation potential in the TiO_2-MoA CTCs

Figure 26 shows the photocatalytic activity of the TiO_2-MoA-270 calcined samples using ROS scavengers to degrade TC. Benzoquinone and isopropanol were used as the scavengers for $^{\bullet}O_2^-$ and $OH^{\bullet}$.

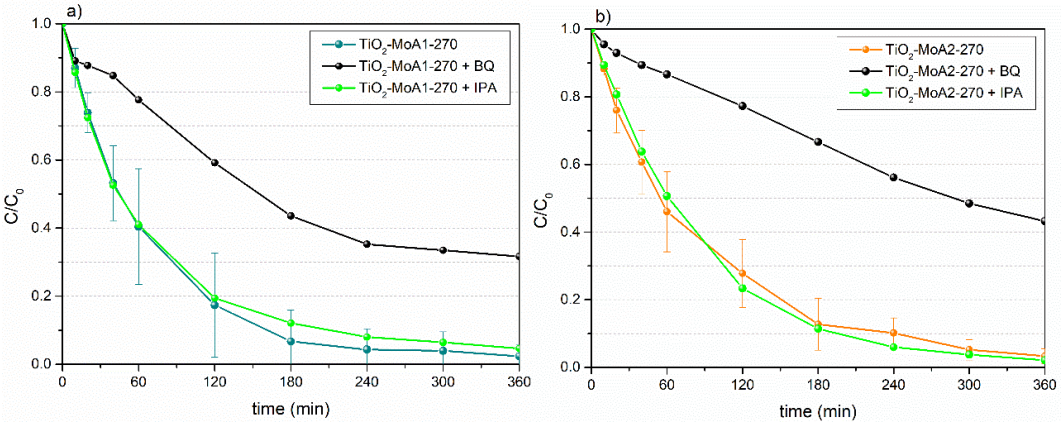

Figure 26: Photodegradation of TC by a) TiO_2-MoA1-270 and b) TiO_2-MoA2-270 with and without the addition of BQ or IPA scavengers.

Figures 26a and 26b revealed almost the same effect of ROS generation on the photocatalytic performance of TiO_2-MoA1-270 and TiO_2-MoA2-270. As expected, the addition of IPA as $OH^{\bullet}$ scavenger did not impact on the photodegradation activity of TiO_2-MoA-270 CTCs. The TC abatement after the addition of IPA was 95,4% and 98.0% for TiO_2-MoA1-270 and TiO_2-MoA2-270, respectively, within the error bars of the degradation without adding any scavengers, after 6h. Therefore, the $OH^{\bullet}$ radicals do not play a role in the photocatalytic performance of TiO_2-MoA-270 CTCs. In addition, some previous study on TiO_2-bidentate ligands CTCs reported that the formation of h^+ into the HOMO of MoA, due to the injection of e^- to CB of TiO_2 and into energy sublevels of SETOV, was not capable to produce $OH^{\bullet}$ radicals (Almeida *et al.*, 2022; Gil-Londoño, Cremona, *et al.*, 2023; Gil-Londoño, Krambrock, *et al.*, 2023), corroborating our results and discussion, *vide infra* § 5.4.4.

Conversely, the addition of BQ as $^{\bullet}O_2^-$ scavenger significantly impact on the photodegradation activity of TiO_2-MoA-270 CTCs. The TC abatement after the addition of BQ was reduced from 97.7% ± 3.3% and 96.7% ± 2.1% to 61.4% and 56.8%, after 6 h, for TiO_2-MoA1-270 and TiO_2-MoA2-270. respectively. Therefore, the $^{\bullet}O_2^-$ radicals are efficiently generated and play the main role in TiO_2-MoA-270 CTCs, corroborating the effect of $^{\bullet}O_2^-$ radicals previously reported for TiO_2-ACAC (Gil-Londoño, Krambrock, *et al.*, 2023) and TiO_2-GA (Gil-Londoño, Cremona, *et al.*, 2023) CTCs calcined at 270 °C. Furthermore, EPR experimental data acquired in a narrow magnetic field interval of 10 mT revealed the presence of $^{\bullet}O_2^-$ signal (axial g tensor with values $g_{||} = 2.0093$ and $g_{\perp}=2.0275$) for both calcined TiO_2-MoA CTCs. Figure 35 (Appendix B) shows the EPR experimental spectra of

calcined TiO_2-MoA CTCs in a narrow magnetic field interval and EPR calculated spectra of $^{\bullet}O_2^-$ and SETOV, using Easyspin software. However, the TC abatement even with the addition of BQ is higher than 50% for both calcined TiO_2-MoA CTCs. The absorption spectra of TC photodegradation with addition of BQ over time (Figure 36, Appendix B) revealed an BQ abatement (as judged through the band situated at 246 nm) of ~80% during the first 2 h of the test for both calcined TiO_2MoA CTCs. The effective generation of $^{\bullet}O_2^-$ radicals is capable of degrading almost all BQ in the first 2 h of the photocatalytic test and, consequently, the TC molecules continue to be degraded over time by newly formed $^{\bullet}O_2^-$ radicals.

5.4. Discussion

One of the main goals of our study was the synthesis of a novel charge transfer complex between TiO_2 anatase nanoparticles modified and malonic acid sensible to visible light and with high surface area (> 250.0 $m^2.g^{-1}$). The calcined TiO_2-MoA1-270 and TiO_2-MoA2-270 CTC achieved these features and revealed expressive photocatalytic activity to degrade especially tetracycline under visible light with reduced power (Figure 25).

The photocatalytic performance of calcined TiO_2-MoA-270 CTCs is directly associated to the formation of bidentate chelating bonds (covalent bonds) between MoA and TiO_2 surface (Figures 19 and 20) and to the formation of extrinsic oxygen vacancies, promoting electronic levels within the TiO_2 bandgap (Figures 21 to 24).

5.4.1. Enhanced physical properties of TiO_2-MoA CTCs for photocatalytic applications

The sol-gel synthesis of TiO_2 adding twice the molar concentration of malonic acid in respect to Ti (complexing ratio, A = [MoA]/[Ti] = 2) is capable to produce anatase TiO_2 nanoparticles due to strong interaction formed between MoA and Ti^{4+}, during the synthesis.

The XRPD pattern of the as-prepared TiO_2-MoA CTCs reveals mean crystalline sizes lower than 5 nm (Figure 16). Our XRPD results corroborated several other studies pointing out that the addition of bidentate ligands in the sol-gel synthesis is capable to produce nanocrystalline xerogels of anatase (Gil-

Londoño, Cremona, *et al.*, 2023; Habran, Pontón, *et al.*, 2018; Liu *et al.*, 2017; Mančić *et al.*, 2023; Scolan e Sanchez, 1998). In addition, the bonds formed between TiO_2 and bidentate ligands are responsible for enhancement of two physical properties of the TiO_2-MoA CTCs fundamental for photocatalytic application. The one is a shorter diffusion distance for the photogenerated charge (e^-/h^+ pairs) to reach the TiO_2 surface due to very small nanoparticles formed within the sol-gel process (Habran, Krambrock, *et al.*, 2018; Kim e Kwak, 2007; Ren *et al.*, 2017). Consequently, the second is very high surface area of the formed CTCs, leading to a higher density of active sites and, therefore, to higher probability of ROS formation (Ren *et al.*, 2017). The TiO_2-MoA2 xerogel has a higher surface area than TiO_2-MoA1, probably due to the greater interaction between MoA and titanium isopropoxide during sol-gel synthesis (second synthesis methodology), leading to lower reactivity of the hydrolysis-condensation reactions of the metal alkoxide precursor.

As observed in our study, the calcined TiO_2-MoA-270 present very high surface area ($\geq$ 306.1 $m^2.g^{-1}$, Table 1). Bakre and Tilve (Bakre e Tilve, 2017) reported surface area of 253.8 $m^2.g^{-1}$ and 297.0 $m^2.g^{-1}$ for two calcined anatase nanopowders (at 500 °C, during 3 h) produced *via* sol-gel synthesis with addition of malonic and glutaric acid (complexing ratio A = 6), respectively. Liu et al. (Liu *et al.*, 2017) also used the same complexing ratio of 6 and reported a TiO_2-Acetic acid CTCs, calcined at 300 °C, during 2 h, with the surface area of 255.9 $m^2.g^{-1}$. Therefore, possibly, the complexation ratio fixed at 2, as well as lower calcination temperatures and times can promote higher surface area of TiO_2-bidenate ligand CTCs, as obtained in our study.

Furthermore, the TiO_2-MoA-270 CTCs calcined samples significantly increased the surface area when compared to TiO_2-MoA xerogels (Table 1). The TG, MS-TG and FTIR analysis confirm that the calcination of TiO_2-MoA xerogels promotes the release of weakly bonded MoA, while preserving MoA covalently bonded to the TiO_2 surface (Figure 18 and 19), causing an increase of mesopore volumes and specific surface areas in the TiO_2-MoA-270 CTCs (Table 1). In addition, TiO_2-MoA2-270 presents practically the same crystallite size (4.8 nm) as presented inTiO_2-MoA xerogel (4.7 nm). A similar feature was also observed by Liu et al. (Liu *et al.*, 2017) for the TiO_2-AA CTCs calcined at 100 °C and 300 °C. Therefore, the highest surface area obtained by TiO_2-MoA2-270 CTC is associated

to the release of MoA content weakly bound to TiO_2, *i.e.*, elimination of excess of organic content in TiO_2-MoA pores and to preservation of original crystallite/nanoparticle size of TiO_2-MoA xerogels (Figure 17).

5.4.2. Enhanced visible light absorption of TiO_2-MoA CTCs: LMCT mechanism and oxygen vacancy sublevels

The DRS and PL data (Figures 21 and 22) of TiO_2-MoA xerogels reveals that the visible light absorption is an exclusive consequence of LMCT mechanism. Therefore, only a partial sensitization in the visible light is observed for the as-prepared TiO_2-MoA xerogels (Figure 6). Barbieriková et al. (Barbieriková *et al.*, 2022) also reported a low visible light absorption of the CTCs formed between a commercial TiO_2 nanomaterial (P-25) and squaric acid. In addition, the TiO_2-Squaric acid CTC showed an optical bandgap of ~ 2.5 eV (Barbieriková *et al.*, 2022), characteristic values of LMCT mechanism (Luciani, Imparato e Vitiello, 2020; Zhang, Kim e Choi, 2014).

However, the calcination process of the TiO_2-MoA xerogels promotes the absorption of light along visible spectrum (Figure 21). The DRS and PL curves of TiO_2-MoA-270 materials demonstrated the existence of LMCT mechanism (strong bonds between MoA molecules and TiO_2) together with formation of energy sublevels due SETOVs content, *i.e.*, creation of color center F^+. Serporne (Serpone, 2006) reported optical bandgaps values of 1.78 eV and 1.63 eV for two different TiO_2 rutile materials with the presence of F^+ color center, close to the values observed for the TiO_2-MoA1-270 (1.78 eV) and TiO_2-MoA2-270 (1.75 eV) CTCs (Table 1), corroborating the presence of SETOVs in our calcined samples. Furthermore, EPR of TiO_2-MoA-270 CTCs confirmed the presence of SETOV in the calcinated samples.

Therefore, the possible charge transfer paths, due to the LMCT mechanism and the energy sublevels of SETOV within the TiO_2 bandgap (F^+ center), allow for improvement of visible light absorption in calcined TiO_2-MoA-270 CTCs

5.4.3. Mechanisms of photocatalytic degradation of aqueous pollutants by TiO_2-MoA xerogels

The TiO_2-MoA1 and TiO_2-MoA2 xerogels revealed high photocatalytic efficiency for TC degradation (94.8% ± 7.3% and 93.7% ± 8.9%, respectively) and negligible 4-CP degradation (3.2% ± 1.6% and 5.8% ± 2.0%, respectively). As elucidated by DRS, PL and EPR, the TiO_2-MoA xerogels did not present any evidence of the creation of oxygen vacancies. Therefore, the LMCT mechanism is the predominant charge transfer path in TiO_2-MoA xerogels, leading to generation of superoxide, $^{\bullet}O_2^-$ (Figure 27), and consequence high TC degradation (Figure 25). TiO_2-MoA xerogels show higher photocatalytic activity to degrade TC, as well as larger surface area and mesopore volume than the other calcined CTCs, such as TiO_2-ACAC-300 (Almeida *et al.*, 2022), TiO_2-ACAC-270 (Gil-Londoño, Krambrock, *et al.*, 2023) and TiO_2-GA-270 (Gil-Londoño, Cremona, *et al.*, 2023). Probably, the high surface area and mesopore volume of the as-prepared TiO_2-MoA xerogels (Table 1) are determinant to promote efficient TC photodegradation under reduced power visible light, since the xerogels of TiO_2-bidantante ligand provides a limited visible light absorption (Figure 21) (Zhang, Kim e Choi, 2014). Moreover, the h^+ generated in the HOMO of MoA cannot react with the H_2O/OH^- to produce $OH^{\bullet}$, causing an inefficient 4-CP degradation. Finally, the enhanced photocatalytic activity of the TiO_2-MoA xerogels in aqueous medium is attributed to (1) high surface area and (2) efficient $^{\bullet}O_2^-$ radical generation due to LMCT mechanism.

5.4.4. Mechanisms of photocatalytic degradation of aqueous pollutants by calcined TiO_2-MoA xerogels

Both calcined TiO_2-MoA-270 CTCs revealed close to 100% of TC photocatalytic degradation under reduced power of visible light, after 6h. In addition, TiO_2-MoA1-270 and TiO_2-MoA2-270 revealed 4-CP photocatalytic degradation of 25.7% ± 3.6% and 30.8% ± 3.9%, respectively, under the same photocatalytic conditions as applied for TC.

This expressive photocatalytic activity to degrade tetracycline is the result of the synergy of two visible sensitization mechanisms, beyond the increase in surface area and mesopore volume, promoted after the calcination process. One is the LMCT mechanism while the second one is the generation of intermediated energy

sublevels into TiO_2 bandgap due to oxygen vacancies such as SETOVs / F^+ centers, as confirmed by DRS, PL and EPR data. Furthermore, the photocatalytic tests of TC degradation with and without the ROS scavengers performed by TiO_2-MoA-270 CTCs revealed an efficient generation of $^{\bullet}O_2^-$ radical, while $OH^{\bullet}$ radial was inefficiently generated (Figure 26).

Therefore, the charge transfer path in calcined TiO_2-MoA CTCs for the efficient generation of superoxide ($^{\bullet}O_2^-$) radicals, and consequently, abatement of aqueous pollutants can be summarized through the electronic band scheme depicted in Figure 27: (1) direct injection of e^- from HOMO of MoA to CB of TiO_2, (2) from HOMO of MoA to energy sublevels of oxygen vacancies such as SETOV and (3) from oxygen vacancies such as SETOV to CB of TiO_2 anatase. The charge transfer path (1) and (3) promoted the generation of $^{\bullet}O_2^-$ due to reaction between the O_2 molecules and e^- from CB of TiO_2 anatase reaching the surface. The charge transfer path (2) probably increases e^- into oxygen vacancies sublevels, stimulated e^- injection to CB of TiO_2.

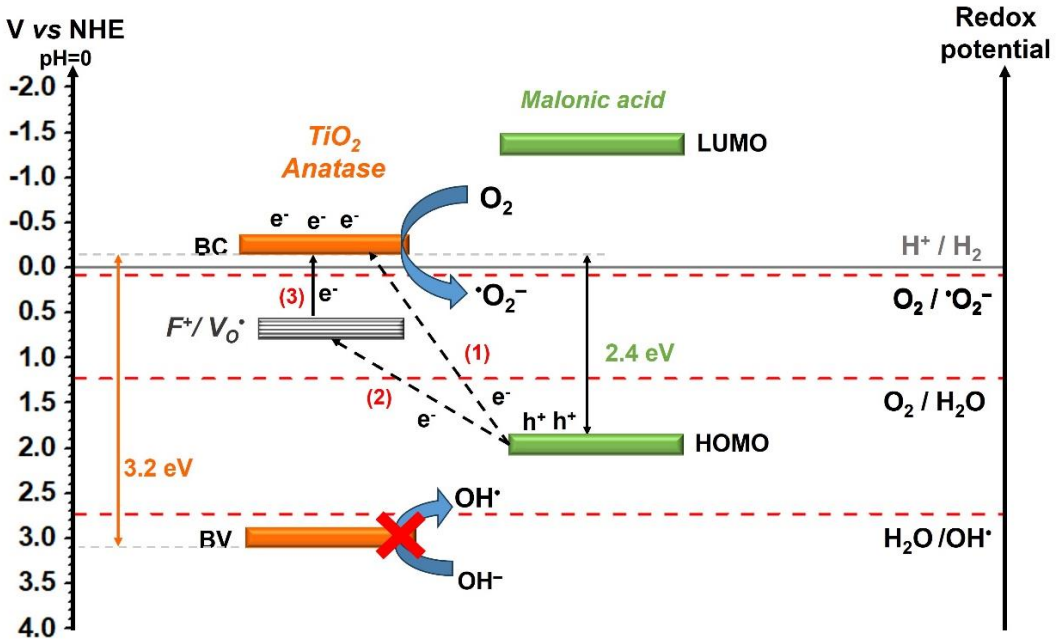

Figure 27: Scheme of electronic bands in TiO_2-MoA-270 CTCs and photocatalytic reactions for ROS generation. The position of BV and BC of anatase at redox potential scale, in accordance with normal hydrogen electrode (NHE), was adopted from literature (Christoforidis e Fornasiero, 2017; Ren *et al.*, 2017), as well as the positions of the ROS species. The energy levels of color center F^+ is in accordance with (Gil-Londoño, Krambrock, *et al.*, 2023; Lei *et al.*, 2001; Santara *et al.*, 2013)

Furthermore, the oxygen vacancies sublevels such as SETOV may reduce the recombination rates of photogenerated carries when the extrinsic oxygen vacancies are dispersed. The trapped electrons undergo repeated hopping and tunneling to the surface of nanoparticles, as reported by Kato et al. (Kato *et al.*, 2022). This phenomenon was observed by Gil-Londoño (Gil-Londoño, Krambrock, *et al.*, 2023) for TiO_2-ACAC-270 CTC (calcined in air) that showed the best TC photodegradation (78.4%) before the evaluation of the photocatalytic potential of the TiO_2-MoA-270 CTCs as presented in this study.

5.5 Conclusions

A novel nanocrystalline CTC formed from TiO_2 anatase coupled to malonic acid, sensible to visible light and with surface area higher than 300.0 $m^2.g^{-1}$ was successful synthetized *via* sol-gel for the first time. The molar complexing ratio of 2 during the hydrolysis-condensation reactions and the calcination temperature of 270 °C were fundamental parameters to produce the TiO_2-MoA CTCs with ~5 nm of mean crystallite size, high surface area and enhanced visible light absorption.

The TGA, MS-TG and FTIR confirmed the formation of weak and strong bonds between MoA and TiO_2 surface. Additionally, the calcination process in air at 270 °C, for 2 h, caused the release of the weakly bonded MoA through partial oxidation of malonic acid, while simultaneously preserved bidentate chelating bounds between MoA and TiO_2.

The bonds between MoA and TiO_2 surface promoted the formation of LMCT mechanism, and consequently, creation of a charge transfer complex TiO_2-MoA, as revealed by DRS and PL data. Furthermore, the calcination at 270°C of the TiO_2-MoA xerogels promoted the creation of extrinsic oxygen vacancies, such as SETOV, without the presence of trivalent titanium species.

The highest photocatalytic TC abatement (close to 100% after 6 h) and significantly photocatalytic abatement of 4-CP using the calcined TiO_2-MoA CTCs under low power visible light (26 W) demonstrated the powerful synergy between LMCT mechanism and energy sublevels due to SETOV / F^+ center. The $^{\bullet}O_2^-$ radicals are efficiently generated and play a principal role at the photocatalytic activity of TiO_2-MoA-270 CTCs. Furthermore, calcined TiO_2-MoA CTCs have

very high surface areas (306.1 $m^2.g^{-1}$ and 323.9 $m^2.g^{-1}$) and mesopore volumes (0.339 $mL.g^{-1}$ and 0.356 $mL.g^{-1}$).

The findings of this research can be applied to the synthesis, *via* sol-gel, of other CTCs between TiO_2 and bidentate ligands, such as dicarboxylic acids. Furthermore, the high photocatalytic performance of TiO_2-MoA CTCs to degrade aqueous pollutants can be explored in further studies on air purification and hydrogen production.

6.
Conclusions and future works

The sol-gel synthesis and the calcination process adopted successfully produced nano-TiO_2 strongly bound to the chelating ligands, acetylacetone and malonic acid, capable of absorbing along the visible spectrum when calcined at 300 °C (TiO_2-ACAC CTC) and 270 °C (TiO_2-MoA CTC).

Both nanocrystalline CTC based on TiO_2 modified with Acetylacetone and malonic acid showed high photocatalytic activity to TC degradation and significant performance to degrade 4-CP under reduced power of visible light. The TiO_2-MoA-270 CTCs showed the highest photocatalytic activity, degrading approximately 100% of the TC after 6 h.

The TiO_2-A300 CTC, as well as, TiO_2-MoA-270 CTCs, were an efficient source of superoxide radicals. However, the CTCs based on TiO_2 modified with chelating ligands did not efficiently generate $OH^{\bullet}$ radicals.

The novel TiO_2-MoA CTCs showed significantly enhance in the photocatalytic performance in relation to the TiO_2-ACAC CTCs due to the high surface area and mesopore volume, since both calcined CTCs presented synergy between LMCT mechanism and energy sublevels due to SETOV / F^+ center.

The calcined TiO_2-MoA CTCs have very high surface areas (306.1 $m^2.g^{-1}$ and 323.9 $m^2.g^{-1}$) and mesopore volumes (0.339 $mL.g^{-1}$ and 0.356 $mL.g^{-1}$).

Based on the findings of this research, the following proposals were suggested for future works:

- Synthesis, *via* sol-gel, of other CTCs between TiO_2 and bidentate ligands, such as maleic acid and acetic acid.
- Exploit the high photocatalytic activity of TiO_2-MoA CTCs in air purification and hydrogen production studies.
- Development of heterostructures based on TiO_2-MoA CTC, and similar CTCs, with semiconductors capable of generating $OH^{\bullet}$ radicals under visible light, and probably forming more powerful photocatalysts.

7.

References

ABD ELKODOUS, M.; S. EL-SAYYAD, G.; ABDEL MAKSOUD, M. I. A.; KUMAR, R.; MAEGAWA, K.; KAWAMURA, G.; TAN, W. K.; MATSUDA, A. Nanocomposite matrix conjugated with carbon nanomaterials for photocatalytic wastewater treatment. **Journal of Hazardous Materials**, v. 410, n. September 2020, p. 124657, 2021.

ABREU, M.; MORGADO, E.; JARDIM, P.; MARINKOVIC, B. The effect of anatase crystal morphology on the photocatalytic conversion of NO by TiO_2-based nanomaterials. **Open Chemistry**, v. 10, n. 4, p. 1183–1198, 1 ago. 2012.

ACIK, I. O.; MADARÁSZ, J.; KRUNKS, M.; TÕNSUAADU, K.; POKOL, G.; NIINISTÖ, L. Titanium(IV) acetylacetonate xerogels for processing titania films : A thermoanalytical study. **Journal of Thermal Analysis and Calorimetry**, v. 97, n. 1, p. 39–45, 2009.

ADDONIZIO, M. L.; ARONNE, A.; IMPARATO, C. Amorphous hybrid TiO_2 thin films: The role of organic ligands and UV irradiation. **Applied Surface Science**, v. 502, n. May 2019, 2020.

ALAM, U.; SHAH, T. A.; KHAN, A.; MUNEER, M. One-pot ultrasonic assisted sol-gel synthesis of spindle-like Nd and V codoped ZnO for efficient photocatalytic degradation of organic pollutants. **Separation and Purification Technology**, v. 212, n. August 2018, p. 427–437, 2019.

ALMEIDA, L. A.; DOSEN, A.; VIOL, J.; MARINKOVIC, B. A. TiO_2-Acetylacetone as an Efficient Source of Superoxide Radicals under Reduced Power Visible Light: Photocatalytic Degradation of Chlorophenol and Tetracycline. **Catalysts**, v. 12, n. 2, p. 116, 19 jan. 2022.

ALMEIDA, L. A.; HABRAN, M.; SANTOS CARVALHO, R. DOS; MAIA DA COSTA, M. E. H.; CREMONA, M.; SILVA, B. C.; KRAMBROCK, K.; GINOBLE PANDOLI, O.; MORGADO JR., E.; MARINKOVIC, B. A. The Influence of Calcination Temperature on Photocatalytic Activity of TiO_2-Acetylacetone Charge Transfer Complex towards Degradation of NO_x under Visible Light. **Catalysts**, v. 10, n. 12, p. 1463, 14 dez. 2020.

ALMEIDA, L. A. L. **Nanohíbridos sensíveis à luz visível à base de nanofolhas de ferrititanato esfoliadas e um complexo de transferência de cargas: Efeito de diferentes razões molares de [Ti] anatásio / [Ti]**

ferrititanato e distintas rotas de síntese. Pontifícia Universidade Católica do Rio de Janeiro, 2019.

ANSARI, F.; SHEIBANI, S.; FERNANDEZ-GARCÍA, M. Surface modification of Cu_2O-CuO photocatalyst on Cu wire through decorating with TiO_2 nanoparticles for enhanced visible light photocatalytic activity. **Journal of Alloys and Compounds**, v. 919, p. 165864, 25 out. 2022.

ARONNE, A. *et al.* Electronic properties of TiO_2-based materials characterized by high Ti^{3+} self-doping and low recombination rate of electron–hole pairs. **RSC Advances**, v. 7, n. 4, p. 2373–2381, 2017.

BAI, X.; JIA, J.; DU, Y.; HU, X.; LI, J.; LIU, E.; FAN, J. Multi-level trapped electrons system in enhancing photocatalytic activity of TiO_2 nanosheets for simultaneous reduction of Cr (VI) and RhB degradation. **Applied Surface Science**, v. 503, n. September 2019, p. 144298, 2020.

BAKRE, P. V.; TILVE, S. G. Dicarboxylic Acids as Soft Templates for the Sol-Gel Synthesis of Mesoporous Nano TiO_2 with Enhanced Photocatalytic Activity. **ChemistrySelect**, v. 2, n. 24, p. 7063–7072, 22 ago. 2017.

BANERJEE, R.; PAL, A.; GHOSH, D.; GHOSH, A. B.; NANDI, M.; BISWAS, P. Improved photocurrent response, photostability and photocatalytic hydrogen generation ability of CdS nanoparticles in presence of mesoporous carbon. **Materials Research Bulletin**, v. 134, n. September 2020, p. 111085, 2021.

BARBIERIKOVÁ, Z.; ŠIMUNKOVÁ, M.; BREZOVÁ, V.; SREDOJEVIĆ, D.; LAZIĆ, V.; LONČAREVIĆ, D.; NEDELJKOVIĆ, J. M. Interfacial charge transfer complex between TiO_2 and non-aromatic ligand squaric acid. **Optical Materials**, v. 123, p. 111918, 1 jan. 2022.

BOWIE, J. H.; WILLIAMS, D. H.; LAWESSON, S.-O.; SCHROLL, G. Studies in Mass Spectrometry. IX. [1] Mass Spectra of β-Diketones. **The Journal of Organic Chemistry**, v. 31, n. 5, p. 1384–1390, 1 maio 1966.

BOŽANIĆ, D. K.; GARCIA, G. A.; NAHON, L.; SREDOJEVIĆ, D.; LAZIĆ, V.; VUKOJE, I.; AHRENKIEL, S. P.; DJOKOVIĆ, V.; ŠLJIVANČANIN, Ž.; NEDELJKOVIĆ, J. M. Interfacial Charge Transfer Transitions in Colloidal TiO_2 Nanoparticles Functionalized with Salicylic acid and 5-Aminosalicylic acid: A Comparative Photoelectron Spectroscopy and DFT Study. **Journal of Physical Chemistry C**, v. 123, n. 47, p. 29057–29066, 27 nov. 2019.

CAIRES, F. J.; LIMA, L. S.; CARVALHO, C. T.; GIAGIO, R. J.; IONASHIRO, M. Thermal behaviour of malonic acid, sodium malonate and its compounds with some bivalent transition metal ions. **Thermochimica Acta**, v. 497, n. 1–2, p. 35–40, 10 jan. 2010.

CHEN, J.; WANG, H.; HUANG, G.; ZHANG, Z.; HAN, L.; SONG, W.; LI, M.; ZHANG, Y. Facile synthesis of urchin-like hierarchical Nb_2O_5 nanospheres with enhanced visible light photocatalytic activity. **Journal of Alloys and Compounds**, v. 728, p. 19–28, 2017.

CHEN, Y.; SOLER, L.; XIE, C.; VENDRELL, X.; SERAFIN, J.; CRESPO, D.; LLORCA, J. A straightforward method to prepare supported Au clusters by mechanochemistry and its application in photocatalysis. **Applied Materials Today**, v. 21, p. 100873, dez. 2020.

CHESHME KHAVAR, A. H.; MOUSSAVI, G.; MAHJOUB, A. R.; LUQUE, R.; RODRÍGUEZ-PADRÓN, D.; SATTARI, M. Enhanced visible light photocatalytic degradation of acetaminophen with Ag_2S-ZnO@rGO core-shell microsphere as a novel catalyst: Catalyst preparation and characterization and mechanistic catalytic experiments. **Separation and Purification Technology**, v. 229, n. July, p. 115803, dez. 2019.

CHRISTOFORIDIS, K. C.; FORNASIERO, P. Photocatalytic Hydrogen Production: A Rift into the Future Energy Supply. **ChemCatChem**, v. 9, n. 9, p. 1523–1544, 10 maio 2017.

COSTA, A. M. L. M.; MARINKOVIC, B. A.; SUGUIHIRO, N. M.; SMITH, D. J.; COSTA, M. E. H. M. DA; PACIORNIK, S. Fe-doped nanostructured titanates synthesized in a single step route. **Materials Characterization**, v. 99, p. 150–159, 2015.

DALLINGA, J. W.; NIBBERING, N. M. M.; BOERBOOM, A. J. H. Curie–point pyrolysis of saturated and unsaturated dicarboxylic acids studied by tandem mass spectrometry. **J. Chem. Soc., Perkin Trans. 2**, n. 6, p. 1065–1076, 1984.

DESSAL, C. *et al.* Influence of Pt particle size and reaction phase on the photocatalytic performances of ultradispersed Pt/TiO_2 catalysts for hydrogen evolution. **Journal of Catalysis**, v. 375, p. 155–163, jul. 2019.

DIVINS, N. J.; TRIFONOV, T.; RODRÍGUEZ, Á.; LLORCA, J. A million-microchannel multifuel steam reformer for hydrogen production. **Catalysis Today**, v. 362, n. April, p. 55–61, fev. 2021.

ESTEBAN, N. M. H. **Nanohíbrido mesoporoso sensível à luz visível preparado a partir de ferrititanato do tipo lepidocrocita acoplado a um complexo de transferência de carga e empregado na conversão fotocatalítica de um gás poluente**. Pontifícia Universidade Católica do Rio de Janeiro, Departamento, 2017.

FAHMI, A.; MINOT, C.; FOURRÉ, P.; NORTIER, P. A theoretical study of the adsorption of oxalic acid on TiO_2. **Surface Science**, v. 343, n. 3, p. 261–272, dez. 1995.

FÓNAGY, O.; SZABÓ-BÁRDOS, E.; HORVÁTH, O. 1,4-Benzoquinone and 1,4-hydroquinone based determination of electron and superoxide radical formed in heterogeneous photocatalytic systems.

Journal of Photochemistry and Photobiology A: Chemistry, v. 407, p. 113057, 15 fev. 2021.

FUJISHIMA, A.; HONDA, K. Electrochemical Photolysis of Water at a Semiconductor Electrode. **Nature**, v. 238, n. 5358, p. 38–40, 1972.

FUJISHIMA, A.; ZHANG, X.; TRYK, D. A. TiO2 photocatalysis and related surface phenomena. **Surface Science Reports**, v. 63, n. 12, p. 515–582, 2008.

GALEAS, S.; VALDIVIESO-RAMÍREZ, C. S.; PONTÓN, P. I.; GUERRERO, V. H.; GOETZ, V. Photocatalytic degradation of phenol under visible light irradiation by using ferrous oxalate synthesized from iron-rich mineral sands via a green hydrothermal route. **Environmental Technology & Innovation**, v. 32, p. 103325, 1 nov. 2023.

GANGULY, S.; FERNANDES, J. R.; DESIRAJU, G. R.; RAO, C. N. R. Phase transition in malonic acid: An infrared study. **Chemical Physics Letters**, v. 69, n. 2, p. 227–229, jan. 1980.

GHORAI, S.; LASKIN, A.; TIVANSKI, A. V. Spectroscopic Evidence of Keto−Enol Tautomerism in Deliquesced Malonic Acid Particles. **The Journal of Physical Chemistry A**, v. 115, n. 17, p. 4373–4380, 5 maio 2011.

GIL-LONDOÑO, J.; CREMONA, M.; KRAMBROCK, K.; COSTA, M. E. H. M. DA; ALMEIDA, L. A.; MARINKOVIC, B. A. Functionalization of anatase nanoparticles with Glutaric acid and their photochemical and photocatalytic properties under visible light. **Ceramics International**, v. 49, n. 11, p. 17123–17134, jun. 2023.

GIL-LONDOÑO, J.; KRAMBROCK, K.; OLIVEIRA, R. DE; CREMONA, M.; MAIA DA COSTA, M. E. H.; MARINKOVIC, B. A. Extrinsic Point Defects in TiO_2–Acetylacetone Charge-Transfer Complex and Their Effects on Optical and Photochemical Properties. **Inorganic Chemistry**, v. 62, n. 5, p. 2273–2288, 6 fev. 2023.

GRABOWSKA, B.; HOLTZER, M.; EICHHOLZ, S.; HODOR, K.; BOBROWSKI, A. Thermal analysis of a sodium salt of the maleic acid-acrylic acid copolymer used as a polymeric binder. **Polimery**, v. 56, n. 03, p. 151, mar. 2011.

GUAN, D.; YU, Q.; XU, C.; TANG, C.; ZHOU, L.; ZHAO, D.; MAI, L. Aerosol synthesis of trivalent titanium doped titania/carbon composite microspheres with superior sodium storage performance. **Nano Research**, v. 10, n. 12, p. 4351–4359, 17 dez. 2017.

HABRAN, M.; KRAMBROCK, K.; MAIA DA COSTA, M. E. H.; MORGADO, E.; MARINKOVIC, B. A. TiO_2 anatase nanorods with non-equilibrium crystallographic {001} facets and their coatings exhibiting high photo-oxidation of NO gas. **Environmental Technology**, v. 39, n. 2, p. 231–239, 17 jan. 2018.

HABRAN, M.; PONTÓN, P. I.; MANCIC, L.; PANDOLI, O.; KRAMBROCK, K.; COSTA, M. E. H. M. DA; LETICHEVSKY, S.; COSTA, A. M. L. M.; MORGADO, E.; MARINKOVIC, B. A. Visible light sensitive mesoporous nanohybrids of lepidocrocite-like ferrititanate coupled to a charge transfer complex: Synthesis, characterization and photocatalytic degradation of NO. **Journal of Photochemistry and Photobiology A: Chemistry**, v. 365, n. June, p. 133–144, out. 2018.

HE, X.; KAI, T.; DING, P. Heterojunction photocatalysts for degradation of the tetracycline antibiotic: a review. **Environmental Chemistry Letters**, v. 19, n. 6, p. 4563–4601, 30 dez. 2021.

HERNÁNDEZ RODRÍGUEZ, M. J.; MELIÁN, E. P.; ARAÑA, J.; NAVÍO, J. A.; GONZÁLEZ DÍAZ, O. M.; SANTIAGO, D. E.; DOÑA RODRÍGUEZ, J. M. Influence of water on the oxidation of no on pd/TiO_2 photocatalysts. **Nanomaterials**, v. 10, n. 12, p. 1–16, 2020.

HIGASHIMOTO, S.; NISHI, T.; YASUKAWA, M.; AZUMA, M.; SAKATA, Y.; KOBAYASHI, H. Photocatalysis of titanium dioxide modified by catechol-type interfacial surface complexes (ISC) with different substituted groups. **Journal of Catalysis**, v. 329, p. 286–290, set. 2015.

HONG, S. Y.; LEE, H. J.; PARK, J. K.; HEO, J. H.; IM, S. H. Acetylacetone modulated TiO_2 nanoparticles for low-temperature solution processable perovskite solar cell. **International Journal of Energy Research**, v. 46, n. 15, p. 22819–22831, 4 dez. 2022.

HUNGE, Y. M.; YADAV, A. A.; MAHADIK, M. A.; BULAKHE, R. N.; SHIM, J. J.; MATHE, V. L.; BHOSALE, C. H. Degradation of organic dyes using spray deposited nanocrystalline stratified WO_3/TiO_2 photoelectrodes under sunlight illumination. **Optical Materials**, v. 76, p. 260–270, 2018.

IMPARATO, C.; D'ERRICO, G.; MACYK, W.; KOBIELUSZ, M.; VITIELLO, G.; ARONNE, A. Interfacial Charge Transfer Complexes in TiO_2-Enediol Hybrids Synthesized by Sol-Gel. **Langmuir**, v. 38, n. 5, p. 1821–1832, 8 fev. 2022.

KAPILASHRAMI, M.; ZHANG, Y.; LIU, Y.-S.; HAGFELDT, A.; GUO, J. Probing the Optical Property and Electronic Structure of TiO_2 Nanomaterials for Renewable Energy Applications . **Chemical Reviews**, v. 114, n. 19, p. 9662–9707, 2014.

KATO, K.; UEMURA, Y.; ASAKURA, K.; YAMAKATA, A. Role of Oxygen Vacancy in the Photocarrier Dynamics of WO_3 Photocatalysts: The Case of Recombination Centers. **The Journal of Physical Chemistry C**, v. 126, n. 22, p. 9257–9263, 9 jun. 2022.

KIM, D. S.; KWAK, S. Y. The hydrothermal synthesis of mesoporous TiO_2 with high crystallinity, thermal stability, large surface area, and enhanced photocatalytic activity. **Applied Catalysis A: General**, v. 323, p. 110–118, 2007.

KIM, G.; LEE, S. H.; CHOI, W. Glucose-TiO_2 charge transfer complex-mediated photocatalysis under visible light. **Applied Catalysis B: Environmental**, v. 162, p. 463–469, 2015.

KOSSANYI, J.; MOGTO, J. K. Spectrométrie de Masse—IV: Fragmentation des Dicétones—ε. **Organic Mass Spectrometry**, v. 3, n. 6, p. 721–734, jun. 1970.

LAM, S.-M.; SIN, J.-C.; SATOSHI, I.; ABDULLAH, A. Z.; MOHAMED, A. R. Enhanced sunlight photocatalytic performance over Nb_2O_5/ZnO nanorod composites and the mechanism study. **Applied Catalysis A: General**, v. 471, p. 126–135, fev. 2014.

LASHUK, B.; PINEDA, M.; ABUBAKR, S.; BOFFITO, D.; YARGEAU, V. Application of photocatalytic ozonation with a WO_3/TiO_2 catalyst for PFAS removal under UVA/visible light. **Science of The Total Environment**, v. 843, p. 157006, out. 2022.

LEI, Y.; ZHANG, L. D.; MENG, G. W.; LI, G. H.; ZHANG, X. Y.; LIANG, C. H.; CHEN, W.; WANG, S. X. Preparation and photoluminescence of highly ordered TiO_2 nanowire arrays. **Applied Physics Letters**, v. 78, n. 8, p. 1125–1127, 19 fev. 2001.

LI, F.; DU, P.; LIU, W.; LI, X.; JI, H.; DUAN, J.; ZHAO, D. Hydrothermal synthesis of graphene grafted titania/titanate nanosheets for photocatalytic degradation of 4-chlorophenol: Solar-light-driven photocatalytic activity and computational chemistry analysis. **Chemical Engineering Journal**, v. 331, n. August 2017, p. 685–694, jan. 2018.

LI, MEICHEN; LI, Y.; ZHAO, J.; LI, MINGCHENG; WU, Y.; NA, P. Alizarin-TiO_2 LMCT Complex with Oxygen Vacancies: An Efficient Visible Light Photocatalyst for Cr(VI) Reduction. **Chinese Journal of Chemistry**, v. 38, n. 11, p. 1332–1338, 2020.

LI, X.; XU, H.; SHI, J.-L.; HAO, H.; YUAN, H.; LANG, X. Salicylic acid complexed with TiO_2 for visible light-driven selective oxidation of amines into imines with air. **Applied Catalysis B: Environmental**, v. 244, n. September 2018, p. 758–766, maio 2019.

LI, Y.; WU, X.; HO, W.; LV, K.; LI, Q.; LI, M.; CHENG, S. Graphene-induced formation of visible-light-responsive SnO_2-Zn_2SnO_4 Zscheme photocatalyst with surface vacancy for the enhanced photoreactivity towards NO and acetone oxidation. **Chemical Engineering Journal**, v. 336, n. November 2017, p. 200–210, 2018.

LIU, J.; HAN, L.; AN, N.; XING, L.; MA, H.; CHENG, L.; YANG, J.; ZHANG, Q. Enhanced visible-light photocatalytic activity of carbonate-doped anatase TiO_2 based on the electron-withdrawing bidentate carboxylate linkage. **Applied Catalysis B: Environmental**, v. 202, p. 642–652, mar. 2017.

LIU, N.; WANG, J.; WU, J.; LI, Z.; HUANG, W.; ZHENG, Y.; LEI, J.; ZHANG, X.; TANG, L. Magnetic Fe_3O_4@MIL-53(Fe) nanocomposites derived from MIL-53(Fe) for the photocatalytic degradation of ibuprofen under visible light irradiation. **Materials Research Bulletin**, v. 132, n. July, p. 111000, dez. 2020.

LIU, Q.; WANG, S.; REN, Q.; LI, T.; TU, G.; ZHONG, S.; ZHAO, Y.; BAI, S. Stacking design in photocatalysis: Synergizing cocatalyst roles and anti-corrosion functions of metallic MoS_2 and graphene for remarkable hydrogen evolution over CdS. **Journal of Materials Chemistry A**, v. 9, n. 3, p. 1552–1562, 2021.

LIU, X.; LIU, Y.; LU, S.; GUO, W.; XI, B. Performance and mechanism into TiO_2/Zeolite composites for sulfadiazine adsorption and photodegradation. **Chemical Engineering Journal**, v. 350, n. May, p. 131–147, 2018.

LU, F.; CHEN, K.; FENG, Q.; CAI, H.; MA, D.; WANG, D.; LI, X.; ZUO, C.; WANG, S. Insight into the enhanced magnetic separation and photocatalytic activity of Sn-doped TiO_2 core-shell photocatalyst. **Journal of Environmental Chemical Engineering**, v. 9, n. 5, p. 105840, 1 out. 2021.

LUCIANI, G.; IMPARATO, C.; VITIELLO, G. Photosensitive Hybrid Nanostructured Materials: The Big Challenges for Sunlight Capture. **Catalysts**, v. 10, n. 1, p. 103, 10 jan. 2020.

MADARÁSZ, J.; KANEKO, S.; OKUYA, M.; POKOL, G. Comparative evolved gas analyses of crystalline and amorphous titanium(IV)oxo-hydroxo-acetylacetonates by TG-FTIR and TG/DTA-MS. **Thermochimica Acta**, v. 489, n. 1–2, p. 37–44, 2009.

MAMAGHANI, A. H.; HAGHIGHAT, F.; LEE, C.-S. Photocatalytic oxidation technology for indoor environment air purification: The state-of-the-art. **Applied Catalysis B: Environmental**, v. 203, p. 247–269, abr. 2017.

MANČIĆ, L.; ALMEIDA, L. A.; MACHADO, T. M.; GIL-LONDOÑO, J.; DINIĆ, I.; TOMIĆ, M.; MARKOVIĆ, S.; JARDIM, P.; MARINKOVIC, B. A. Tetracycline Removal through the Synergy of Catalysis and Photocatalysis by Novel NaYF4:Yb,Tm@TiO_2-Acetylacetone Hybrid Core-Shell Structures. **International Journal of Molecular Sciences**, v. 24, n. 11, p. 9441, 29 maio 2023.

MANCUSO, A.; MORANTE, N.; CARLUCCIO, M. DE; SACCO, O.; RIZZO, L.; FONTANA, M.; ESPOSITO, S.; VAIANO, V.; SANNINO, D. Solar driven photocatalysis using iron and chromium doped TiO_2 coupled to moving bed biofilm process for olive mill wastewater treatment. **Chemical Engineering Journal**, v. 450, p. 138107, dez. 2022.

MAO, L.; CAI, X.; GAO, H.; DIAO, X.; ZHANG, J. A newly designed porous oxynitride photoanode with enhanced charge carrier mobility. **Nano Energy**, v. 39, p. 172–182, 1 set. 2017.

MARTÍNEZ, L.; SOLER, L.; ANGURELL, I.; LLORCA, J. Effect of TiO_2 nanoshape on the photoproduction of hydrogen from water-ethanol mixtures over Au_3Cu/TiO_2 prepared with preformed Au-Cu alloy nanoparticles. **Applied Catalysis B: Environmental**, v. 248, n. February, p. 504–514, jul. 2019.

MATERAZZI, S.; FOTI, C.; CREA, F. Nickel and copper biomimetic complexes with N-heterocyclic dicarboxylic ligands. **Thermochimica Acta**, v. 573, p. 101–105, dez. 2013.

MEDIĆ, M. M.; VASIĆ, M.; ZARUBICA, A. R.; TRANDAFILOVIĆ, L. V.; DRAŽIĆ, G.; DRAMIĆANIN, M. D.; NEDELJKOVIĆ, J. M. Enhanced photoredox chemistry in surface-modified Mg_2TiO_4 nano-powders with bidentate benzene derivatives. **RSC Advances**, v. 6, n. 97, p. 94780–94786, 2016.

MILIĆEVIĆ, B.; ĐORĐEVIĆ, V.; LONČAREVIĆ, D.; DOSTANIĆ, J. M.; AHRENKIEL, S. P.; DRAMIĆANIN, M. D.; SREDOJEVIĆ, D.; ŠVRAKIĆ, N. M.; NEDELJKOVIĆ, J. M. Charge-transfer complex formation between TiO_2 nanoparticles and thiosalicylic acid: A comprehensive experimental and DFT study. **Optical Materials**, v. 73, p. 163–171, 2017.

MOHAMMAD, A.; KHAN, M. E.; CHO, M. H.; YOON, T. Adsorption promoted visible-light-induced photocatalytic degradation of antibiotic tetracycline by tin oxide/cerium oxide nanocomposite. **Applied Surface Science**, v. 565, n. June, p. 150337, nov. 2021.

MORAES, N. P. DE; MARINS, L. G. P.; MOURA YAMANAKA, M. Y. DE; BACANI, R.; SILVA ROCHA, R. DA; RODRIGUES, L. A. Efficient photodegradation of 4-chlorophenol under solar radiation using a new ZnO/ZnS/carbon xerogel composite as a photocatalyst. **Journal of Photochemistry and Photobiology A: Chemistry**, v. 418, p. 113377, 1 set. 2021.

MORAES, N. P. DE; SIERVO, A. DE; SILVA, T. O.; SILVA ROCHA, R. DA; REDDY, D. A.; LIANQING, Y.; VASCONCELOS LANZA, M. R. DE; RODRIGUES, L. A. Kraft lignin-based carbon xerogel/zinc oxide composite for 4-chlorophenol solar-light photocatalytic degradation: effect of pH, salinity, and simultaneous Cr(VI) reduction. **Environmental Science and Pollution Research**, v. 30, n. 3, p. 8280–8296, 2 jan. 2023.

MORAES, N. P. DE; TOREZIN, F. A.; JUCÁ DANTAS, G. V.; SOUSA, J. G. M. DE; VALIM, R. B.; SILVA ROCHA, R. DA; LANDERS, R.; SILVA, M. L. C. P. DA; RODRIGUES, L. A. TiO_2/Nb_2O_5/carbon xerogel ternary photocatalyst for efficient degradation of 4-chlorophenol under solar light irradiation. **Ceramics International**, v. 46, n. 10, p. 14505–14515, jul. 2020.

MORAES, N. P. DE; VALIM, R. B.; SILVA ROCHA, R. DA; SILVA, M. L. C. P. DA; CAMPOS, T. M. B.; THIM, G. P.; RODRIGUES, L. A. Effect of synthesis medium on structural and photocatalytic properties of ZnO/carbon xerogel composites for solar and visible light degradation of 4-chlorophenol and bisphenol A. **Colloids and Surfaces A: Physicochemical and Engineering Aspects**, v. 584, n. September 2019, p. 124034, jan. 2020.

MYILSAMY, M.; MAHALAKSHMI, M.; SUBHA, N.; RAJABHUVANESWARI, A.; MURUGESAN, V. Visible light responsive mesoporous graphene-Eu_2O_3/TiO_2 nanocomposites for the efficient photocatalytic degradation of 4-chlorophenol. **RSC Advances**, v. 6, n. 41, p. 35024–35035, 2016.

NORTON, M. G.; CATER, C. B. **Ceramic materials: science and engineering**. Springer. New York: 2007.

NOSAKA, Y.; NOSAKA, A. Y. Generation and Detection of Reactive Oxygen Species in Photocatalysis. **Chemical Reviews**, v. 117, n. 17, p. 11302–11336, 13 set. 2017.

OBREGÓN, S.; RUÍZ-GÓMEZ, M. A.; RODRÍGUEZ-GONZÁLEZ, V.; VÁZQUEZ, A.; HERNÁNDEZ-URESTI, D. B. A novel type-II $Bi_2W_2O_9$/g-C_3N_4 heterojunction with enhanced photocatalytic performance under simulated solar irradiation. **Materials Science in Semiconductor Processing**, v. 113, p. 105056, 1 jul. 2020.

OHNO, T.; SARUKAWA, K.; MATSUMURA, M. Photocatalytic activities of pure rutile particles isolated from TiO_2 owder by dissolving the anatase component in HF solution. **Journal of Physical Chemistry B**, v. 105, n. 12, p. 2417–2420, 2001.

OJA AÇIK, I.; MADARÁSZ, J.; KRUNKS, M.; TÕNSUAADU, K.; JANKE, D.; POKOL, G.; NIINISTÖ, L. Thermoanalytical studies of titanium(IV) acetylacetonate xerogels with emphasis on evolved gas analysis. **Journal of Thermal Analysis and Calorimetry**, v. 88, n. 2, p. 557–563, 15 maio 2007.

OMRANI, N.; NEZAMZADEH-EJHIEH, A. A comprehensive study on the enhanced photocatalytic activity of Cu_2O/$BiVO_4$/WO_3 nanoparticles. **Journal of Photochemistry and Photobiology A: Chemistry**, v. 389, n. October 2019, 2020.

PAGACZ, J.; LESZCZYŃSKA, A.; MODESTI, M.; BOARETTI, C.; ROSO, M.; MALKA, I.; PIELICHOWSKI, K. Thermal decomposition studies of bio-resourced polyamides by thermogravimetry and evolved gas analysis. **Thermochimica Acta**, v. 612, p. 40–48, 22 jul. 2015.

PESSANHA, E. C.; MENEZES, F. A. F.; GUIMARÃES, A. O.; JARDIM, P. M.; MARINKOVIC, B. A. Cu_2O nanocubes/TiO_2 heterostructure and its adsorption and photocatalytic properties for tetracycline removal. **Journal**

of Photochemistry and Photobiology A: Chemistry, v. 440, p. 114652, 1 jun. 2023.

PISKUNOV, S.; LISOVSKI, O.; BEGENS, J.; BOCHAROV, D.; ZHUKOVSKII, Y. F.; WESSEL, M.; SPOHR, E. C-, N-, S-, and Fe-Doped TiO_2 and $SrTiO_3$ Nanotubes for Visible-Light-Driven Photocatalytic Water Splitting: Prediction from First Principles. **Journal of Physical Chemistry C**, v. 119, n. 32, p. 18686–18696, 15 jul. 2015.

QU, Q.; GENG, H.; PENG, R.; CUI, Q.; GU, X.; LI, F.; WANG, M. Chemically Binding Carboxylic Acids onto TiO_2 Nanoparticles with Adjustable Coverage by Solvothermal Strategy. **Langmuir**, v. 26, n. 12, p. 9539–9546, 15 jun. 2010.

REN, H.; KOSHY, P.; CHEN, W.-F.; QI, S.; SORRELL, C. C. Photocatalytic materials and technologies for air purification. **Journal of Hazardous Materials**, v. 325, p. 340–366, mar. 2017.

RITACCO, I.; IMPARATO, C.; FALIVENE, L.; CAVALLO, L.; MAGISTRATO, A.; CAPORASO, L.; FARNESI CAMELLONE, M.; ARONNE, A. Spontaneous Production of Ultrastable Reactive Oxygen Species on Titanium Oxide Surfaces Modified with Organic Ligands. **Advanced Materials Interfaces**, v. 8, n. 17, p. 2100629, 8 set. 2021.

ROCHKIND, M.; PASTERNAK, S.; PAZ, Y. Using dyes for evaluating photocatalytic properties: A critical review. **Molecules**, v. 20, n. 1, p. 88–110, 2015.

SABZEHEI, K.; HADAVI, S. H.; BAJESTANI, M. G.; SHEIBANI, S. Comparative evaluation of copper oxide nano-photocatalyst characteristics by formation of composite with TiO_2 and ZnO. **Solid State Sciences**, v. 107, n. May, 2020.

SANCHEZ, C.; LIVAGE, J; BABONNEAU, F. Chemical modification of alkoxide Precursor. v. 100, p. 65–76, 1988.

SANGWICHIEN, C.; ARANOVICH, G. Density functional theory predictions of adsorption isotherms with hysteresis loops. **Colloids and Surfaces A: Physicochemical and Engineering Aspects**. v. 206, n. 1-3, p. 313– 320, 2002.

SANNINO, F.; PERNICE, P.; IMPARATO, C.; ARONNE, A.; D'ERRICO, G.; MINIERI, L.; PERFETTI, M.; PIROZZI, D. Hybrid TiO_2–acetylacetonate amorphous gel-derived material with stably adsorbed superoxide radical active in oxidative degradation of organic pollutants. **RSC Advances**, v. 5, n. 114, p. 93831–93839, 2015.

SANTARA, B.; GIRI, P. K.; IMAKITA, K.; FUJII, M. Evidence of oxygen vacancy induced room temperature ferromagnetism in solvothermally synthesized undoped TiO_2 nanoribbons. **Nanoscale**, v. 5, n. 12, p. 5476, 2013.

SARAVANAN, A.; KUMAR, P. S.; JEEVANANTHAM, S.; ANUBHA, M.; JAYASHREE, S. Degradation of toxic agrochemicals and pharmaceutical pollutants: Effective and alternative approaches toward photocatalysis. **Environmental Pollution**, v. 298, p. 118844, 1 abr. 2022.

SCHECHTEL, E.; DÖREN, R.; FRERICHS, H.; PANTHÖFER, M.; MONDESHKI, M.; TREMEL, W. Mixed Ligand Shell Formation upon Catechol Ligand Adsorption on Hydrophobic TiO_2 Nanoparticles. **Langmuir**, v. 35, n. 38, p. 12518–12531, 24 set. 2019.

SCHNEIDER, J.; MATSUOKA, M.; TAKEUCHI, M.; ZHANG, J.; HORIUCHI, Y.; ANPO, M.; BAHNEMANN, D. W. Understanding TiO_2 Photocatalysis: Mechanisms and Materials. **Chemical Reviews**, v. 114, n. 19, p. 9919–9986, 8 out. 2014.

SCOLAN, E.; SANCHEZ, C. Synthesis and Characterization of Surface-Protected Nanocrystalline Titania Particles. **Chemistry of Materials**, v. 10, n. 10, p. 3217–3223, 1 out. 1998.

SERGA, V.; BURVE, R.; KRUMINA, A.; PANKRATOVA, V.; POPOV, A. I.; PANKRATOV, V. Study of phase composition, photocatalytic activity, and photoluminescence of TiO_2 with Eu additive produced by the extraction-pyrolytic method. **Journal of Materials Research and Technology**, v. 13, p. 2350–2360, 1 jul. 2021.

SERPONE, N. Is the Band Gap of Pristine TiO_2 Narrowed by Anion- and Cation-Doping of Titanium Dioxide in Second-Generation Photocatalysts? **The Journal of Physical Chemistry B**, v. 110, n. 48, p. 24287–24293, 1 dez. 2006.

SHAO, X.; ZHANG, Y.; PANG, S.-F.; ZHANG, Y.-H. Vacuum FTIR observation on hygroscopic properties and phase transition of malonic acid aerosols. **Chemical Physics**, v. 483–484, p. 7–11, 1 fev. 2017.

SOUSA, J. G. M. DE; SILVA, T. V. C. DA; MORAES, N. P. DE; CAETANO PINTO DA SILVA, M. L.; SILVA ROCHA, R. DA; LANDERS, R.; RODRIGUES, L. A. Visible light-driven ZnO/g-C_3N_4/carbon xerogel ternary photocatalyst with enhanced activity for 4-chlorophenol degradation. **Materials Chemistry and Physics**, v. 256, n. April, p. 123651, dez. 2020.

SU, R.; TIRUVALAM, R.; HE, Q.; DIMITRATOS, N.; KESAVAN, L.; HAMMOND, C.; LOPEZ-SANCHEZ, J. A.; BECHSTEIN, R.; KIELY, C. J.; HUTCHINGS, G. J.; BESENBACHER, F. Promotion of Phenol Photodecomposition over TiO_2 Using Au, Pd, and Au-Pd Nanoparticles. **ACS Nano**, v. 6, n. 7, p. 6284–6292, 24 jul. 2012.

TAHIR, M.; TASLEEM, S.; TAHIR, B. Recent development in band engineering of binary semiconductor materials for solar driven photocatalytic hydrogen production. **International Journal of Hydrogen Energy**, v. 45, n. 32, p. 15985–16038, 11 jun. 2020.

TALAIEKHOZANI, A.; REZANIA, S.; KIM, K.-H.; SANAYE, R.; AMANI, A. M. Recent advances in photocatalytic removal of organic and inorganic pollutants in air. **Journal of Cleaner Production**, v. 278, p. 123895, jan. 2021.

THOMAS, A. G.; SYRES, K. L. Adsorption of organic molecules on rutile TiO_2 and anatase TiO2 single crystal surfaces. **Chemical Society Reviews**, v. 41, n. 11, p. 4207, 15 maio 2012.

THOMMES, M.; KANEKO, K.; NEIMARK, A. V.; OLIVIER, J. P.; RODRIGUEZ-REINOSO, F.; ROUQUEROL, J.; SING, K. S. W. Physisorption of gases, with special reference to the evaluation of surface area and pore size distribution (IUPAC Technical Report). **Pure and Applied Chemistry**, v. 87, n. 9–10, p. 1051–1069, 1 out. 2015.

THONGTEM, T.; THONGTEM, S. Synthesis of $Li_{1-x}Ni_{1+x}O_2$ using malonic acid as a chelating agent. **Ceramics International**, v. 31, n. 2, p. 241–247, jan. 2005.

TSANG, C. H. A.; LI, K.; ZENG, Y.; ZHAO, W.; ZHANG, T.; ZHAN, Y.; XIE, R.; LEUNG, D. Y. C.; HUANG, H. Titanium oxide based photocatalytic materials development and their role of in the air pollutants degradation: Overview and forecast. **Environment International**, v. 125, n. January, p. 200–228, abr. 2019.

ULLATTIL, S. G.; NARENDRANATH, S. B.; PILLAI, S. C.; PERIYAT, P. Black TiO_2 Nanomaterials: A Review of Recent Advances. **Chemical Engineering Journal**, v. 343, n. November 2017, p. 708–736, jul. 2018.

WANG, Y.; FU, H.; YANG, X.; AN, X.; ZOU, Q.; XIONG, S.; HAN, D. Pt nanoparticles-modified WO_3@TiO_2 core–shell ternary nanocomposites as stable and efficient photocatalysts in tetracycline degradation. **Journal of Materials Science**, v. 55, n. 29, p. 14415–14430, 2020.

WU, S.; LIN, Y.; HU, Y. H. Strategies of tuning catalysts for efficient photodegradation of antibiotics in water environments: a review. **Journal of Materials Chemistry A**, v. 9, n. 5, p. 2592–2611, 7 fev. 2021.

YU, H.; WANG, D.; ZHAO, B.; LU, Y.; WANG, X.; ZHU, S.; QIN, W.; HUO, M. Enhanced photocatalytic degradation of tetracycline under visible light by using a ternary photocatalyst of Ag_3PO_4/AgBr/g-C_3N_4 with dual Z-scheme heterojunction. **Separation and Purification Technology**, v. 237, n. September 2019, p. 116365, 2020.

ZHANG, G.; KIM, G.; CHOI, W. Visible light driven photocatalysis mediated via ligand-to-metal charge transfer (LMCT): an alternative approach to solar activation of titania. **Energy & Environmental Science**, v. 7, n. 3, p. 954, 2014.

ZHANG, Y.; LI, J.; LIU, H. Synergistic Removal of Bromate and Ibuprofen by Graphene Oxide and TiO_2 Heterostructure Doped with F:

Performance and Mechanism. **Journal of Nanomaterials**, v. 2020, p. 1–9, 5 mar. 2020.

ZHAO, D.; CHEN, C.; WANG, Y.; MA, W.; ZHAO, J.; RAJH, T.; ZANG, L. Enhanced photocatalytic degradation of dye pollutants under visible irradiation on Al(III)-modified TiO_2: Structure, interaction, and interfacial electron transfer. **Environmental Science and Technology**, v. 42, n. 1, p. 308–314, 1 jan. 2008.

ZHI, L.; ZHANG, S.; XU, Y.; TU, J.; LI, M.; HU, D.; LIU, J. Controlled growth of AgI nanoparticles on hollow WO_3 hierarchical structures to act as Z-scheme photocatalyst for visible-light photocatalysis. **Journal of Colloid and Interface Science**, v. 579, p. 754–765, 1 nov. 2020.

ZHOU, F. Q.; FAN, J. C.; XU, Q. J.; MIN, Y. L. BiVO4 nanowires decorated with CdS nanoparticles as Z-scheme photocatalyst with enhanced H_2 generation. **Applied Catalysis B: Environmental**, v. 201, p. 77–83, 1 fev. 2017.

ZHOU, H.; QU, Y.; ZEID, T.; DUAN, X. Towards highly efficient photocatalysts using semiconductor nanoarchitectures. **Energy and Environmental Science**, v. 5, n. 5, p. 6732–6743, 2012.

ZHOU, Z.; LI, YANAN; LI, M.; LI, YI; ZHAN, S. Efficient removal for multiple pollutants via Ag_2O/BiOBr heterojunction: A promoted photocatalytic process by valid electron transfer pathway. **Chinese Chemical Letters**, v. 31, n. 10, p. 2698–2704, out. 2020.

ZHU, P.; DUAN, M.; WANG, R.; XU, J.; ZOU, P.; JIA, H. Facile synthesis of ZnO/GO/Ag_3PO_4 heterojunction photocatalyst with excellent photodegradation activity for tetracycline hydrochloride under visible light. **Colloids and Surfaces A: Physicochemical and Engineering Aspects**, v. 602, p. 125118, 5 out. 2020.

8.

Appendix A: Supplementary material to support Chapter 4

A.1.

Photocatalytic system for aqueous pollutants degradation

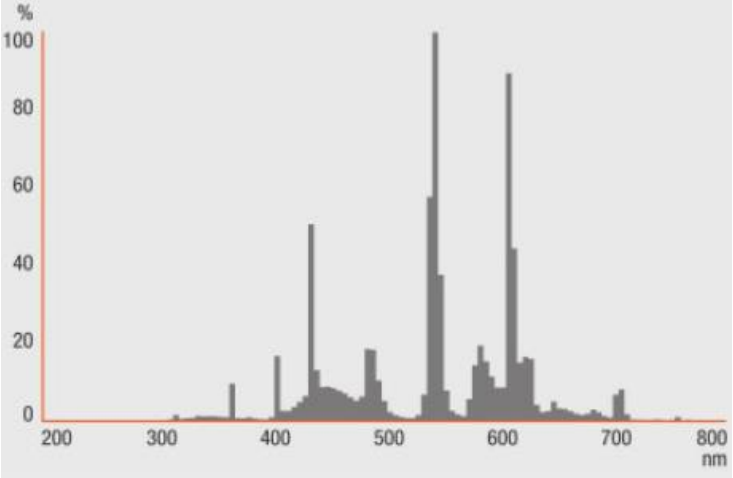

Figure 28: Light emission spectrum of the DULUX D/E 26W lamp

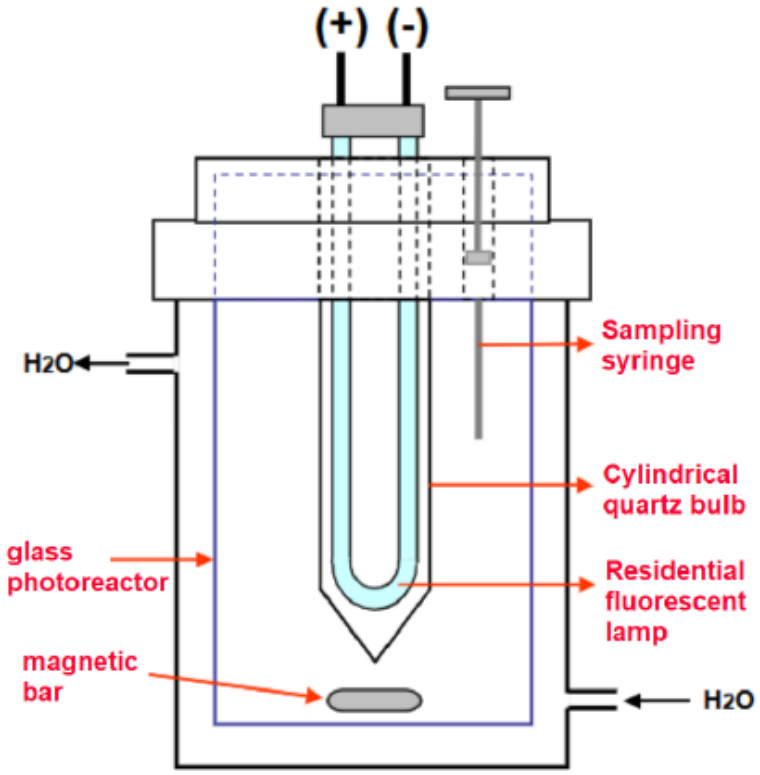

Figure 29: Photocatalytic system for aqueous pollutants degradation.

A.2.

Relationship between UV absorbance of 4-CP and TC and their respective photodegradation during the test time

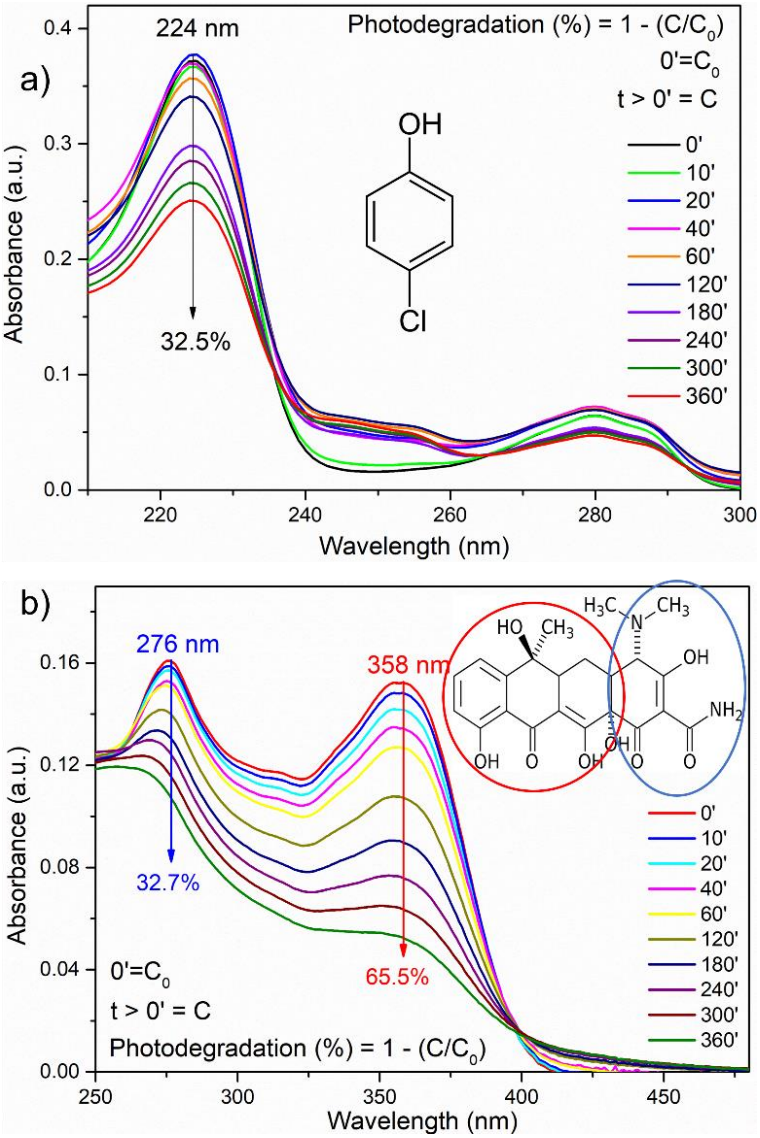

Figure 30: Absorbance of a) 4-CP band, situated at 224 nm, and b) TC band at 358 nm, over the time.

Table 2: 4-CP and TC degradation data obtained in the first repetition of the photocatalytic test using TiO_2-A300.

time (min)	Absorbance (a.u.)		C/C0		Degradation (%)		Average degradation (%)		Standard deviation (%)	
	4-CP	TC	4-CP	TC	4-CP	TC	4-CP	TC	4-CP	TC
-70 (pure pollutants)	0.3836	0.1474	-	-	-	-	-	-	-	-
-60	0.3843	0.1507	-	-	-	-	-	-	-	-
-30	0.3786	0.1625	-	-	-	-	-	-	-	-
0	0.3717	0.1523	1.000	1.000	0.0	0.0	0.0	0.0	0.0	0.0
10	0.3665	0.1482	0.986	0.973	1.4	2.7	2.8	2.6	1.3	0.6
20	0.3769	0.1417	1.014	0.930	-1.4	7.0	1.3	6.5	2.3	0.6
40	0.3696	0.1345	0.995	0.883	0.5	11.7	5.2	12.0	4.0	1.0
60	0.3366	0.1268	0.906	0.833	9.4	16.7	9.5	17.1	0.9	1.0
120	0.3410	0.1074	0.918	0.705	8.2	29.5	12.0	30.3	3.6	2.0
180	0.2983	0.0899	0.803	0.590	19.7	41.0	19.3	41.7	2.1	2.8
240	0.2853	0.0760	0.768	0.499	23.2	50.1	23.6	51.2	0.4	3.6
300	0.2662	0.0638	0.716	0.419	28.4	58.1	27.7	60.6	1.9	3.2
360	0.2507	0.0526	0.675	0.345	32.5	65.5	31.3	68.6	3.1	3.5

A.3.

TGA and DTG curves of TiO_2-ACAC xerogel and TiO_2-A300 sample

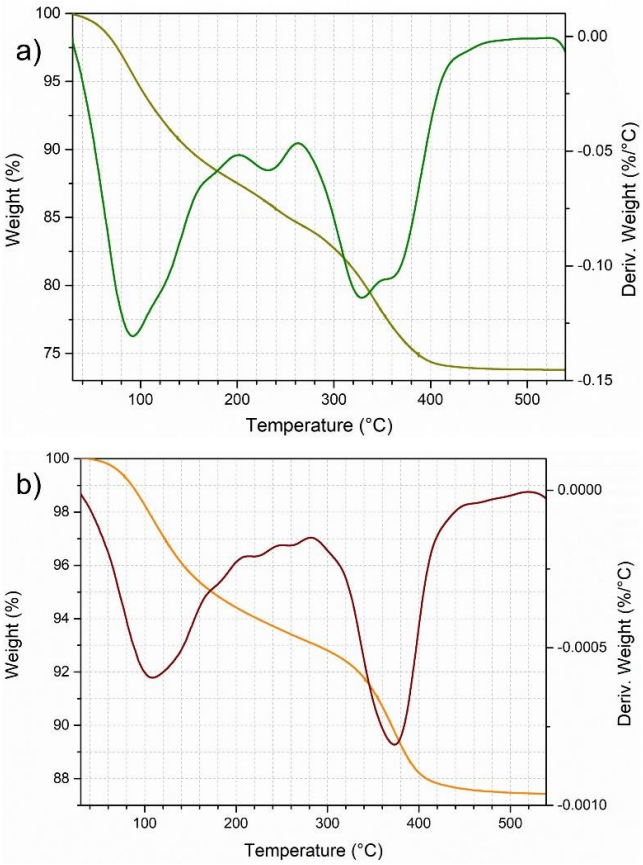

Figure 31: TGA and DTG curves of a) TiO_2-ACAC xerogel and b) TiO_2-A300 sample.

A.4.

Photodegradation of TC until the abatement stabilization using TiO_2-A300.

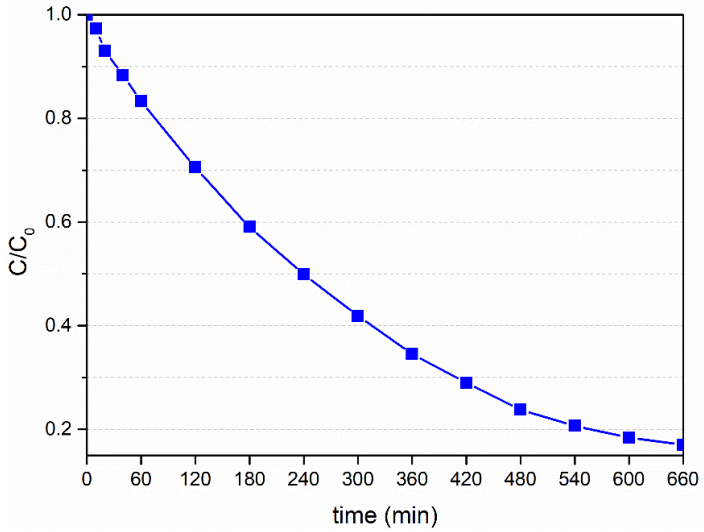

Figure 32: Tetracycline photodegradation by TiO_2-A300.

A.5.

Curve of adsorption and photocatalytic activity of 4-CP and TC using TiO_2-A300.

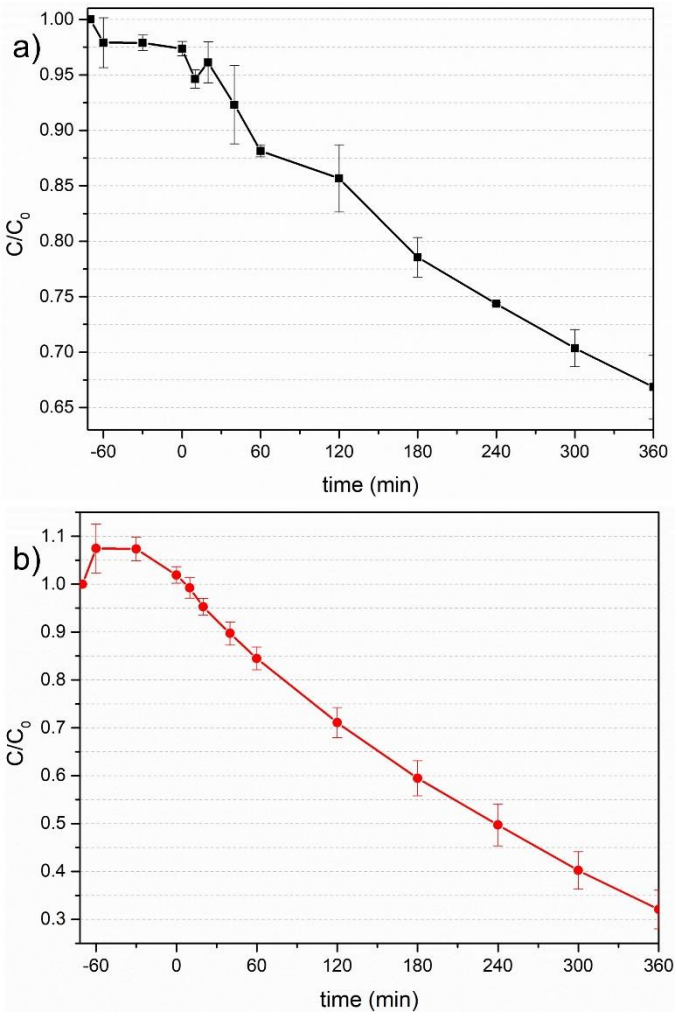

Figure 33: Curves of adsorption (1 h in dark) and photocatalytic activity of 4-CP and TC using TiO_2-A300 of a) 4-CP and b) TC by TiO_2-A300 without scavengers addition during 6 h.

9.

Appendix B: Supplementary material to support Chapter 5

B.1.

Relationship between UV absorbance of TC and 4-CP and their respective photodegradation during the test time

Table 3: TC and 4-CP degradation data obtained in the first repetition of the photocatalytic test using TiO_2-MoA2-270.

time (min)	Absorbance (a.u.)		C/C0		Degradation (%)		Average degradation (%)		Standard deviation (%)	
	TC	4-CP	TC	4-CP	TC	4-CP	TC	4-CP	TC	4-CP
-70 (pure pollutants)	0.11089	0.35861	-	-	-	-	-	-	-	
-60	0.11646	0.35410	-	-	-	-	-	-	-	
-30	0.10814	0.35158	-	-	-	-	-	-	-	
0	0.09683	0.35035	1.000	1.000	0.0	0.0	0.0	0.0	0.0	0.0
10	0.08522	0.32491	0.880	0.927	0.120	0.073	14.0	4.9	5.5	2.3
20	0.07605	0.33210	0.785	0.948	0.215	0.052	25.7	3.6	9.6	1.6
40	0.05819	0.31775	0.600	0.907	0.400	0.093	44.0	7.2	12.6	2.1
60	0.04511	0.31081	0.465	0.887	0.535	0.113	57.4	9.2	14.3	2.0
120	0.01906	0.28567	0.197	0.815	0.803	0.185	79.1	15.3	10.8	3.1
180	0.01140	0.28111	0.118	0.802	0.882	0.198	85.7	18.5	5.84	1.3
240	0.00663	0.26530	0.068	0.757	0.932	0.243	91.5	22.5	4.1	1.8
300	0.00495	0.24530	0.051	0.700	0.949	0.300	94.7	26.8	3.0	3.2
360	0.00417	0.22883	0.043	0.653	0.957	0.347	96.7	30.8	2.0	3.9

B.2.

N_2 adsorption-desorption isotherms of TiO_2-MoA1, TiO_2-MoA2, TiO_2-MoA1-270 and TiO_2-MoA2-270

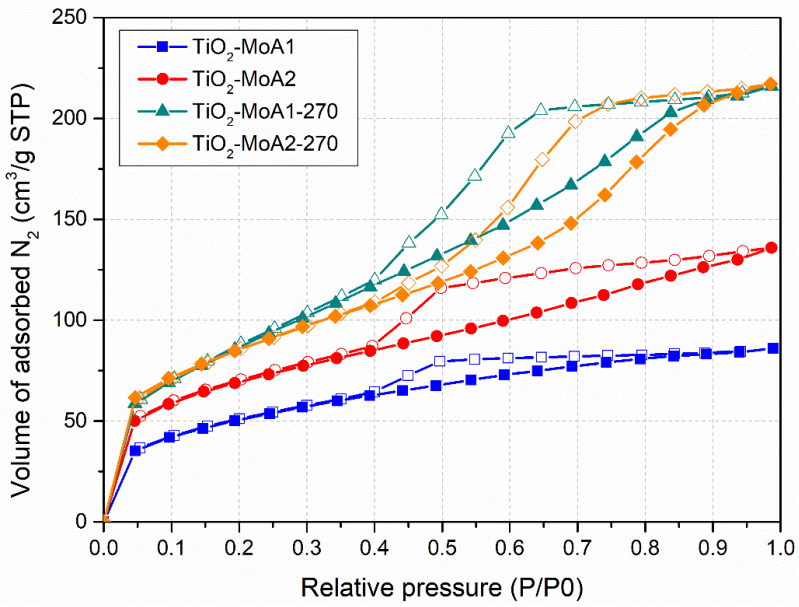

Figure 34: N_2 adsorption-desorption isotherms of TiO_2-MoA1, TiO_2-MoA2, TiO_2-MoA1-270 and TiO_2-MoA2-270.

B.3.

EPR experimental spectra of calcined TiO_2-MoA CTCs and EPR calculated spectra of single-electron-trapped oxygen vacancies (SETOV) and superoxide anion radical

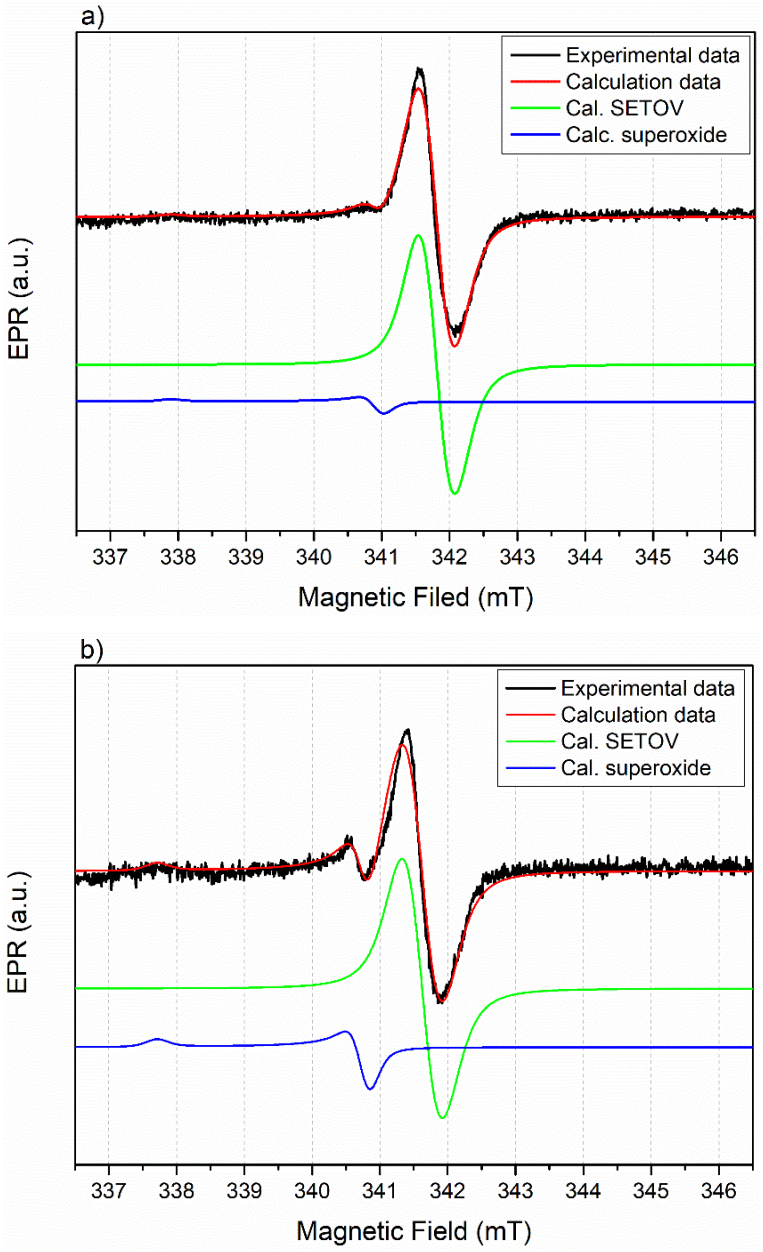

Figure 35: EPR experimental spectra of a) TiO_2-MoA1-270 and b) TiO_2-MoA2-270 and respective EPR calculated spectra of single-electron-trapped oxygen vacancies (SETOV) and superoxide anion radical, using Easyspin software.

B.3.

The absorbance of the BQ band situated at 246 nm and the TC band at 358 nm, over time

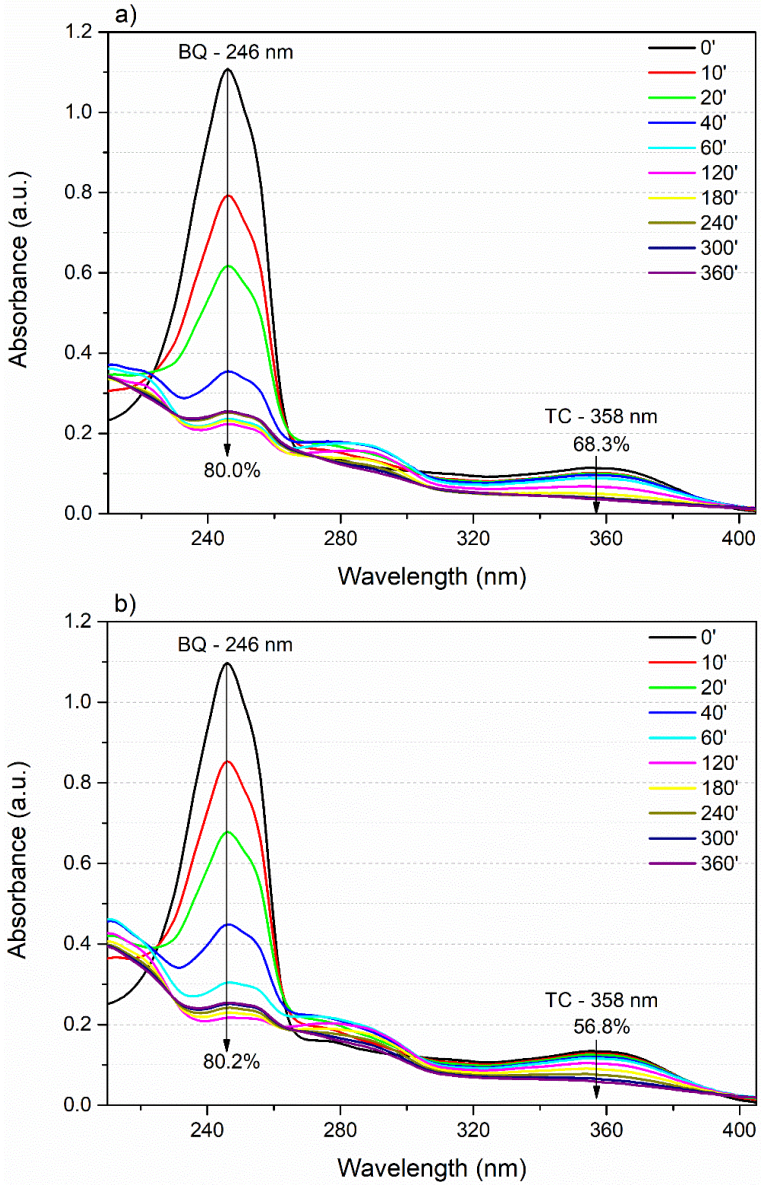

Figure 36: UV absorption spectra of photocatalytic degradation of BQ and TC using a) TiO_2-MoA1-270 and b) TiO_2-MoA2-270, during the test time.

10.
Appendix C: Scientific production

The results of this study are part of two articles:

⋆ Article published in the Catalysts journal (MDPI), open access journal, classified as A1 in Qualis Capes 2013-2016, Article DOI 10.3390/catal12020116:
TiO_2-Acetylacetone as an Efficient Source of Superoxide Radicals under Reduced Power Visible Light: Photocatalytic Degradation of Chlorophenol and Tetracycline
Lucas A. Almeida, Anja Dosen, Juliana Viol and Bojan A. Marinkovic*

Department of Chemical and Materials Engineering, Pontifical Catholic University of Rio de Janeiro (PUC-Rio), Rio de Janeiro 22453-900, Brazil

⋆ Article to be submitted to the Environmental Technology & Innovation journal (Elsevier), classified as A2 in Qualis Capes 2017-2020:
Enhanced photocatalytic activity of TiO_2 anatase nanoparticles modified with malonic acid under reduced power visible light: synthesis, characterization and degradation of tetracycline and chlorophenol
Lucas A. Almeida[a], Juliana Viol[a], Marco Cremona[b], Francine A.F. Menezes[c], André O. Guimarães[c], Jordi Llorca[d,e], Bojan A. Marinkovic[a,*]

[a] Departament of Chemical and Materials Engineering, Pontifical Catholic University of Rio de Janeiro (PUC-Rio), 22453-900, Rio de Janeiro, RJ, Brazil
[b] Departament of Physics, Pontifical Catholic University of Rio de Janeiro (PUC-Rio), 22453-900, Rio de Janeiro, RJ, Brazil
[c] Physical Science Laboratory, Northern Fluminense State University (UENF), 28013-602 Campos dos Goytacazes, Rio de Janeiro, Brazil
[d] Institute of Energy Technologies and Barcelona Research Center in Multiscale Science and Engineering, Universitat Politècnica de Catalunya, Eduard Maristany 16, EEBE, Barcelona 08019, Spain
[e] Department of Chemical Engineering, Universitat Politècnica de Catalunya, Eduard Maristany 16, EEBE, Barcelona 08019, Spain